Gamma-Ray Bursts,

Their High Energy Emission as Observed by EGRET

by

María Magdalena González Sánchez

A dissertation submitted in partial fulfillment

of the requirements for the degree of

Doctor of Philosophy

(Physics)

at the

UNIVERSITY OF WISCONSIN - MADISON

2005

To **José Rubén Alfaro Molina** who is my entire life,

because you are the strength behind me

and;

to **José Rubén Alfaro González** who is our sprout,

because you have been inside of me even after been born.

Abstract

Gamma-ray bursts are among the most powerful events in the universe. These events release most of their energy as photons with energies in the range from 30keV to a few MeV, with a smaller fraction of the energy radiated in radio, optical and soft X-ray afterglows. Several experiments had advocated observing their prompt hard X-ray emission as well as their afterglows in all wavelengths. Thus, huge steps toward a complete understanding of gamma-ray burst afterglows have been done. Nevertheless, radiation above MeV energies has not been fully explored and understood. In particular, the Energetic Gamma Ray Experiment Telescope (EGRET, 1991-2000) observed emission at GeV energies at the same time and delayed from the keV emission for one burst. The GRB emission in the MeV-GeV range will not be further explored by another experiment until 2006. This thesis studies GRB emission in the MeV-GeV energies by a deeper analysis of EGRET data. First, upper limits for prompt and delayed GRB emission in the energy range of 0.02-30 GeV are calculated for bursts that were in the field of view of the EGRET Spark Chambers but were not detected. Secondly, EGRET data from its calorimeter TASC, in the energy range of 1-200 MeV is combined with BATSE data in the energy range of 0.025-2 MeV to better describe the GRB spectra in the MeV regime and its time evolution. Two special bursts that show an extra contribution to their spectra mainly above 10 MeV and up to 200 MeV are discussed. Characterization of the extra contribution to the spectra found in GRB941017 and GRB980923 is done. Also, limits to the existence of this extra contribution are calculated by analyzing TASC and Spark Chamber data finding evidence of this extra contribution in another burst, GRB910503. This emission is not explained by the known non-thermal electron radiation. Therefore this result implies that another radiation mechanism must exist in this gamma-ray burst and is responsible for more than 3 times as much energy release as previously observed. Other possible theoretical implications are also discussed.

Table of Contents

List of Figures

List of Tables

Preface

Human beings chained in a cavern, facing the back wall and trying to understand the outside truth from its shadows, is how I would describe our efforts to explain the nature of the Gamma-Ray Bursts [1]. Our impossibility to travel through the universe to the gamma-ray burst's sites forces us to look at their shadows by detecting light at all frequencies and particles of all kinds that reach our cavern, the Earth.

After their discovery in 1967, as brief flashes of gamma-rays, most of the experiments were dedicated to obtaining basic information such as how far away they are, what kind of emission they have, how long they last, etc. It was a hard task that took around 33 years because of two main reasons. First, because GRBs come from unpredictable directions and their gamma-ray emission lasts less than one hundred seconds making their detection a whole sky search. The second cause was a lack of technology. It was not until the 90's that new and better technology made possible to increase the number of observed bursts, to improve the accuracy of their fast localization and to develop an international network to allow follow-ups from ground telescopes in all frequencies.

The first big observational contributions came with the launch of the Compton Gamma Ray Observatory in 1991, twenty four years after the discovery of GRBs. Many (maybe too many) theories were developed based on a few observational facts. Today,

[1] The allegory of the cave was inspired by Plato's dialogue "The Cavern" in his book "The Republic". In this case, it describes the human search for the truth instead of its sudden discovery and acceptance.

thanks to the observational progress, most of our beliefs are converging to the Standard Fireball Model for the emission process and, binary systems and core collapse of single massive stars as progenitors of short and long bursts respectively.

Recent observations such as the supernova signature associated with a gamma-ray burst, agree with theory indicating that we may be going in the correct direction. However the GRB emission of particles, gravitational waves and radiation above MeV energies has not been fully explored and understood. In particular, the Energetic Gamma Ray Experiment Telescope (EGRET, 1991-2000) observed emission at GeV energies at the same time and delayed from the keV emission for one burst. The GRB emission in the MeV-GeV range will not be further explored by another experiment until 2006. This is why; the goal of my doctorate research is to extend our knowledge of the GRB emission in the MeV-GeV energies by a deeper analysis of EGRET data. This thesis has been divided in five chapters.

The first chapter introduces Gamma-Ray Bursts by giving all the experimental facts that enlighten the basic GRB characteristics. Then the bases of the GRB theory are explained and how they arise from the experimental facts. And finally, the latest relevant experimental results are given.

My doctorate research is explained in the second, third and fourth chapters. In the second chapter, upper limits for the GRB emission in the energy range of 0.02-30 GeV are calculated for bursts that were in the field of view of the EGRET Spark Chambers but were not detected.

In the third chapter, EGRET data from its calorimeter TASC, in the energy range of 1-200 MeV is combined with BATSE data in the energy range of 0.025-2 MeV to better describe the GRB spectra in the MeV regime and its time evolution. Two special bursts that show an extra contribution to their spectra mainly above 10 MeV and up to 200 MeV are discussed.

In the fourth chapter, limits to the existence of an extra contribution to the spectra similar to the observed in GRB941017, are calculated by analyzing TASC and Spark Chamber data. The possible theoretical implications are also discussed.

Finally, in the fifth chapter, general conclusions to the implications of the results of the complete analysis of GRB emission in MeV-GeV are discussed.

Chapter 1

What are Gamma-Ray Bursts?

Gamma-Ray Bursts (GRBs) have been studied since 1963. They were not predicted by any theory prior their discovery and their existence is completely an experimental fact. After 40 years of study and observations, we have started to converge on a model that has successfully explained and predicted their emission at different wavelengths, at least for the bursts lasting longer than 1s. However, there are and there will be observations that puzzle and challenge our conception of Gamma-Ray Bursts.

The first section of this chapter does not pretend to define a Gamma-Ray Burst; it rather gives the most relevant observations that gave rise to the most accepted Gamma-Ray Burst theory, the Standard Fireball shock model. In the second section, the framework of the Standard Fireball shock model is introduced focusing on the concepts relevant to this thesis. In the third section, the latest observations are presented and their impact to the theory are briefly discussed. Finally, the goals of this thesis are presented within the GRB-field context.

1.1 Experimental Evidence. 1967 - 2002

In 1950 a nuclear test ban treaty was negotiated by US, USSR and Great Britain (France joined in 1960 and China in 1964). To assure that the treaty was not being violated in space, US started a project called VELA that in Spanish means "watchman". The VELA project was a series of satellites carrying X-ray detectors to observe the X-ray blast of a nuclear explosion, plus γ-ray and neutron detectors in case the X-rays were being shielded. The satellites were operated in pairs with one satellite flying with a half of one orbit delay to the other one, so that every part of the Earth was under direct observation. The first VELA satellite was launched in 1963. VELA 4 (launched in 1965) discovered the first Gamma-Ray Burst in 1967 but only VELA 5 and 6 (launched in 1969) had the timing accuracy necessary to deduce the directions of the gamma-ray events. In 1972, Ian Strong analyzed these gamma-ray events to conclude that they were of cosmic origin. The discovery was finally published in 1973 ([KL73]) with a total of 16 observed Gamma-Ray Bursts observed between 1969 and 1972.

It was clear from the first GRB observations that they were not due to nuclear explosions since some of them were detected by more than one satellite on opposite sides of the Earth. Furthermore, the detailed time structure of each burst was reproduced by every satellite observing the event. The 16 GRBs reported by [KL73] were observed within the energy ranges of 0.2-1 MeV and 0.3-1.5MeV. Their time durations ranged from less than a second to about 30s. Some GRBs had lightcurves with no structure while others had clearly resolved peaks as observed in the first GRB, see figure 1.1. The VELA satellites were not able to give a GRB spectrum, however the differences in the time of arrival of the signals at the various satellites placed GRB's sources at distances of at least several million kilometers, ruling out the Sun and Earth as the sources.

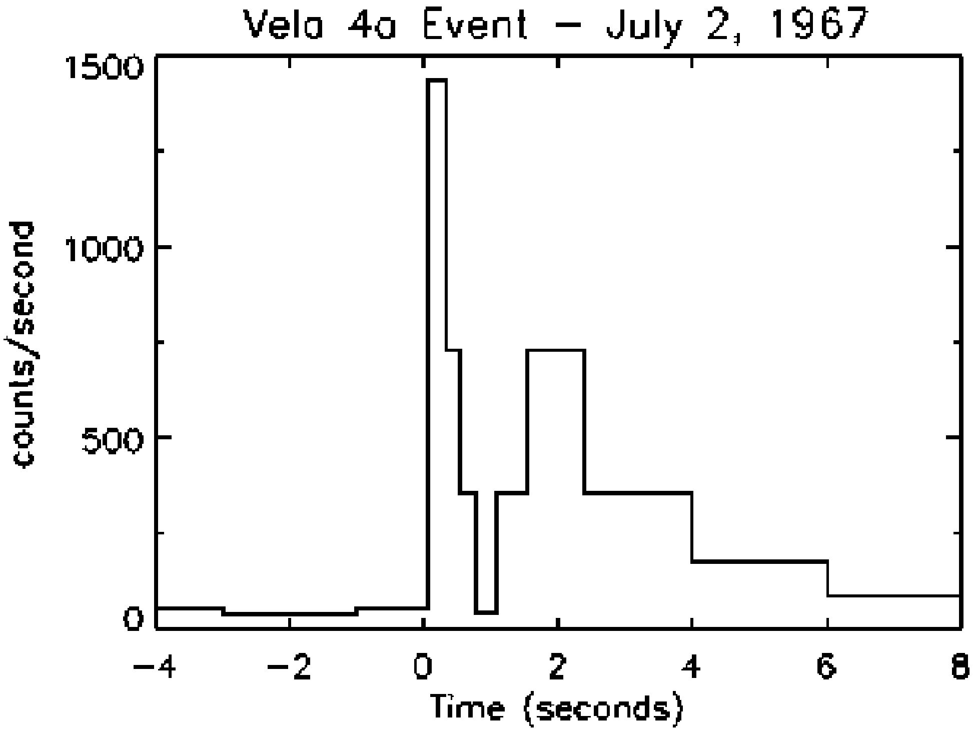

Figure 1.1: Lightcurve of the first Gamma-Ray Burst. It was observed by VELA 4a on July 2nd, 1967. The lightcurve shows the counts per second accumulated by the detector in sequential time intervals. Time equal to zero corresponds to the trigger time. This lightcurve has two well defined peaks at $\sim$0.3 and 2s presenting evidence of structured GRB ligthcurves, later observed in other GRBs.

Several experiments such as PROGNOZ [KU88, AT85], GINGA [ST98], VENERA [MA82, HI90, AT85], SIGNE [AT85], PVO [AT85], ISEE [AT85], SMM [HA98, SH92], OSO-6 [KA77] and OGO-5 [KA77], observed a few hundreds of GRBs during the nineteen years following the publication of the GRB discovery. Most of these experiments were sensitive to a decade of energy in the keV regime. The results from these observations already pointed to some of the now-well-known properties of GRBs. However they were not sufficiently conclusive mainly because they were attributed to the detector sensitivity in such a short energy range.

In 1991, the Compton Gamma-Ray Observatory was launched carrying the Burst and Transient Source Experiment, BATSE, and the Energetic Gamma-Ray Experiment Telescope, EGRET [1] as two of its four detectors, see figure 1.2. BATSE was very successful because its full sky coverage made possible the observation of 2704 GRBs in nine years; and because its sensitivity to the large energy range of 20-2000keV in up to 256 channels with time resolution as small as 64ms allowed the study of the detailed energy and temporal evolution of the GRB spectra. EGRET was able to observe the most energetic γ-ray from GRBs.

Prior to the BATSE observations, the galactic or cosmological origin of gamma-ray bursts was a topic of great debate. Some observations strongly suggested their galactic origin [AT91], and the amount of energy required to be at cosmological distances was huge. However, the angular distribution in galactic coordinates of the bursts observed by BATSE showed that there was no-clustering in the galactic plane region as expected for galactic bursts, see figure 1.3. Furthermore, if a homogenous distribution of bursts in Euclidean space with a standard total energy released is assumed, the number of bursts N, with photon flux above a given value S, should depend on S as follows, $\log(N) \propto -3/2\log(S)$; but the BATSE data showed a deviation from this relation when bursts with smaller photon flux were included [ME92], see figure 1.4 (the peak photon flux is used as equivalent of the total photon flux). Although the cosmological

[1] For a detailed description of BATSE and EGRET refer to chapter 2 and 3.

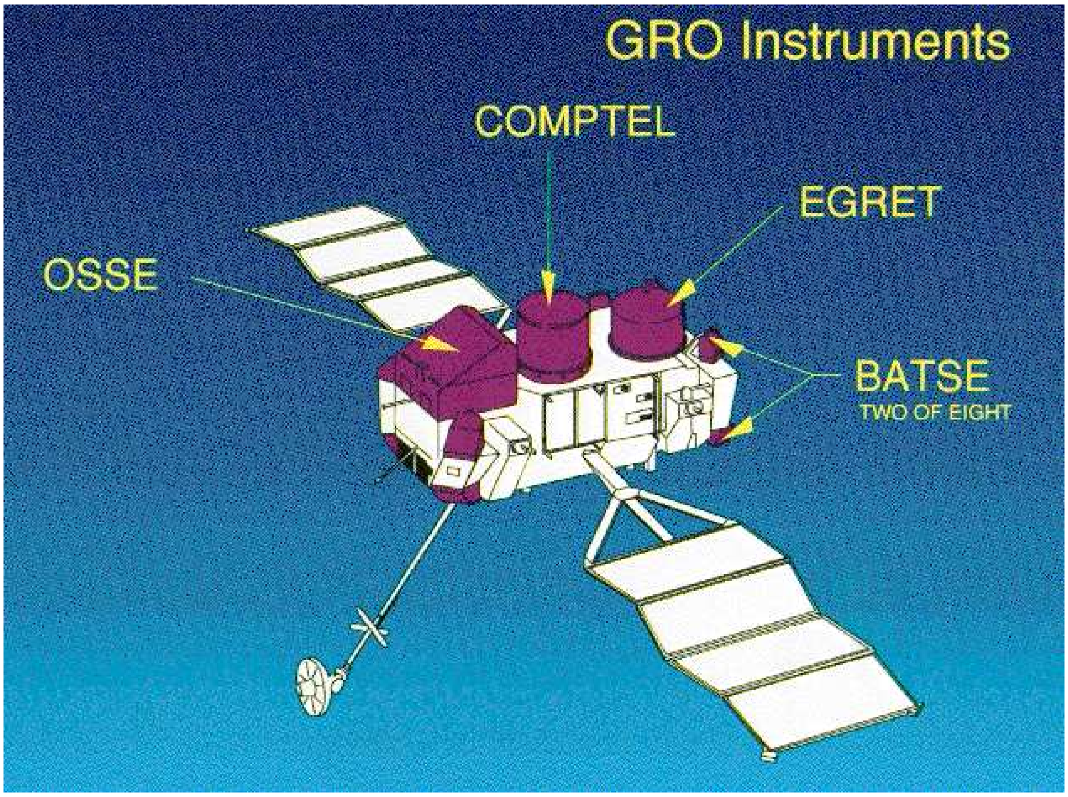

Figure 1.2: Cartoon of the Compton Gamma-Ray Observatory. It carried 4 detectors, OSSE, COMPTEL, BATSE and EGRET. All detectors together covered the energy range of 0.02-30000MeV. BATSE observed the largest GRB catalog giving conclusive results on basic GRB properties. EGRET observed the highest energy emission from GRBs up to now.

origin of gamma-ray bursts could not be concluded from these two results, the galactic origin was rejected.

The variety of lightcurves already observed by prior experiments was also observed in BATSE's bursts [FI95], see figure 1.5. The duration of the bursts showed a bimodal distribution suggesting two different classes of bursts [KO93], see fig. 1.6. However the GRB spectra had general features for all bursts; see 1.7. They had a monotonic continuous non-thermal behavior with a maximum around the 250 keV and most of them

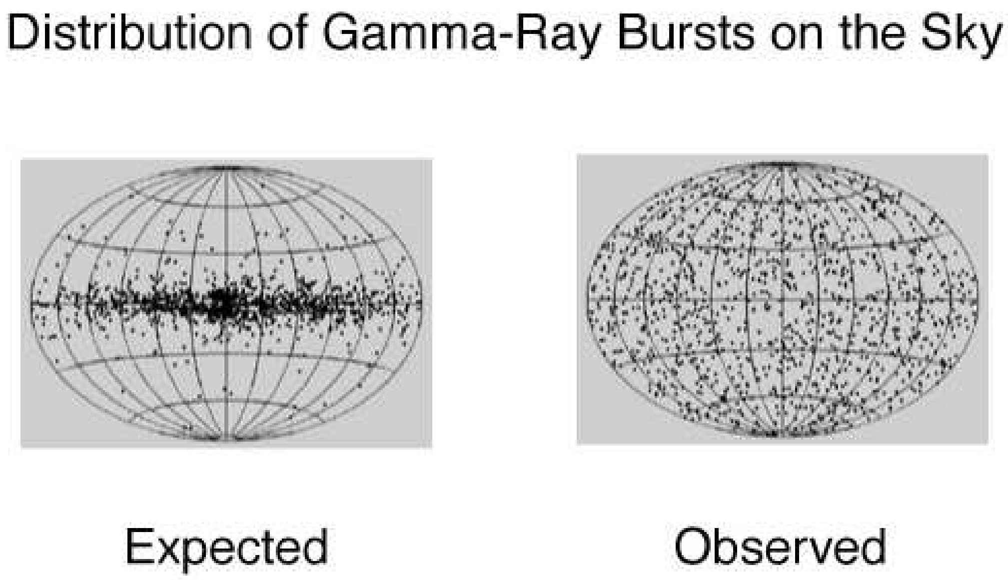

Figure 1.3: Angular distribution of GRB in galactic coordinates. The angular distribution of GRB with hypothetical galactic origin is shown on the left. The measured angular distribution of GRBs is shown on the right.

were fitt using the "GRB function" [BA93] (or Band function, for details see section 1.2). The temporal evolution of GRB spectra was studied using the Band function for the brightest bursts [PR98, PR00], refer to section 1.2 and 1.3 for details. As mentioned before, BATSE results were not unexpected since prior experiments already observed them. However a good understanding of the detector as well as its large energy coverage confirm them as burst properties rather than experimental methodology effects.

In order to study high energy emission CGRO was provided with EGRET. EGRET had a multilevel thin-plate spark chamber designed to detect photons in the energy range from 20MeV to about 30GeV. The most relevant observation was GRB940217 (see figure 1.8). This burst had 2 photons with an energy of $\sim$ 3GeV simultaneously with the keV

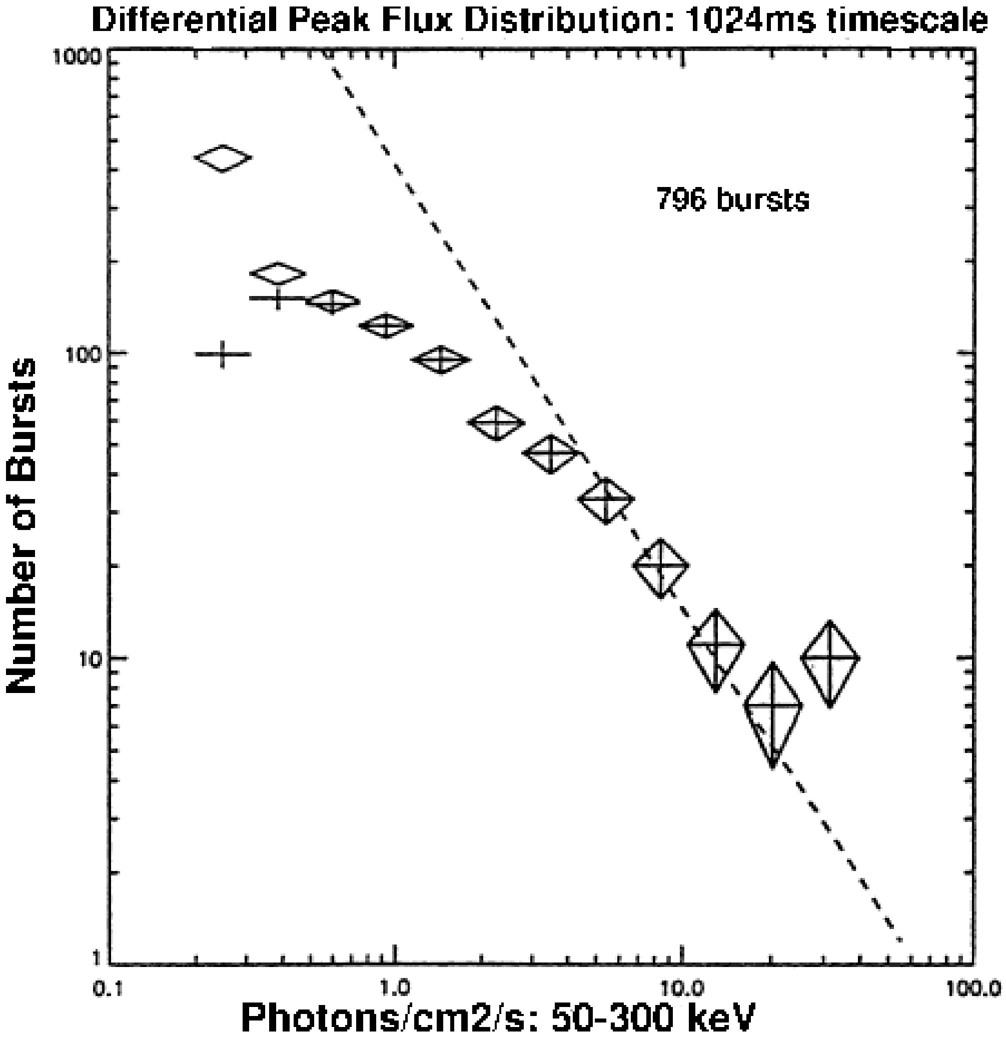

Figure 1.4: Luminosity distribution of GRBs. This plot shows the number of bursts with photon peak flux equal or greater than the value given by the x-axis. If we assume that a homogenous distribution of bursts, a constant total energy emitted and a Euclidean geometry (valid for bursts in the galaxy) then, the luminosity distribution must follow a straight line with slope -3/2 in a log-log plot, as shown by the dashed line. The deviation of the data from the dashed line for smaller photon peak fluxes is an evidence of the cosmological nature of GRBs.

detection and one photon with energy of 18GeV 90 minutes after the keV detection. This observation showed that gamma-ray bursts had prompt and delayed high-energy emission. Because of the lack of statistics, EGRET was not able to characterize this

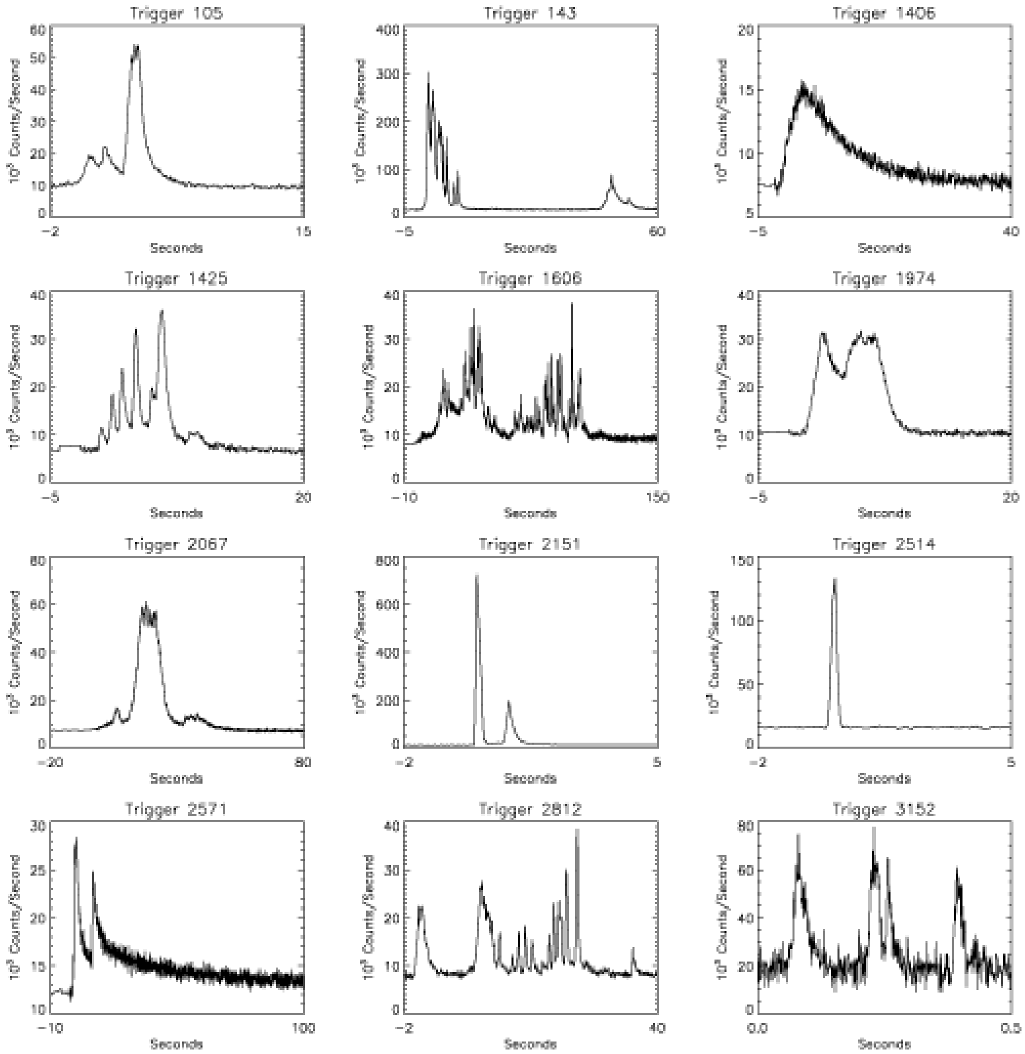

Figure 1.5: Example of different GRB lightcurves. Some bursts present multi-peaked lightcurves. Some peaks are smooth and well-defined while others have substructure. The x-axis is in different scale for each one showing short and long bursts.

emission. And, it did not observed many other bursts because of its small field of view. However it showed the need of develop instruments to observed bursts at energies higher than 1MeV.

While BATSE results were rejecting the galactic origin of GRBs, BeppoSax was launched in 1996. BeppoSax was able to observe bursts with an position error of ar-

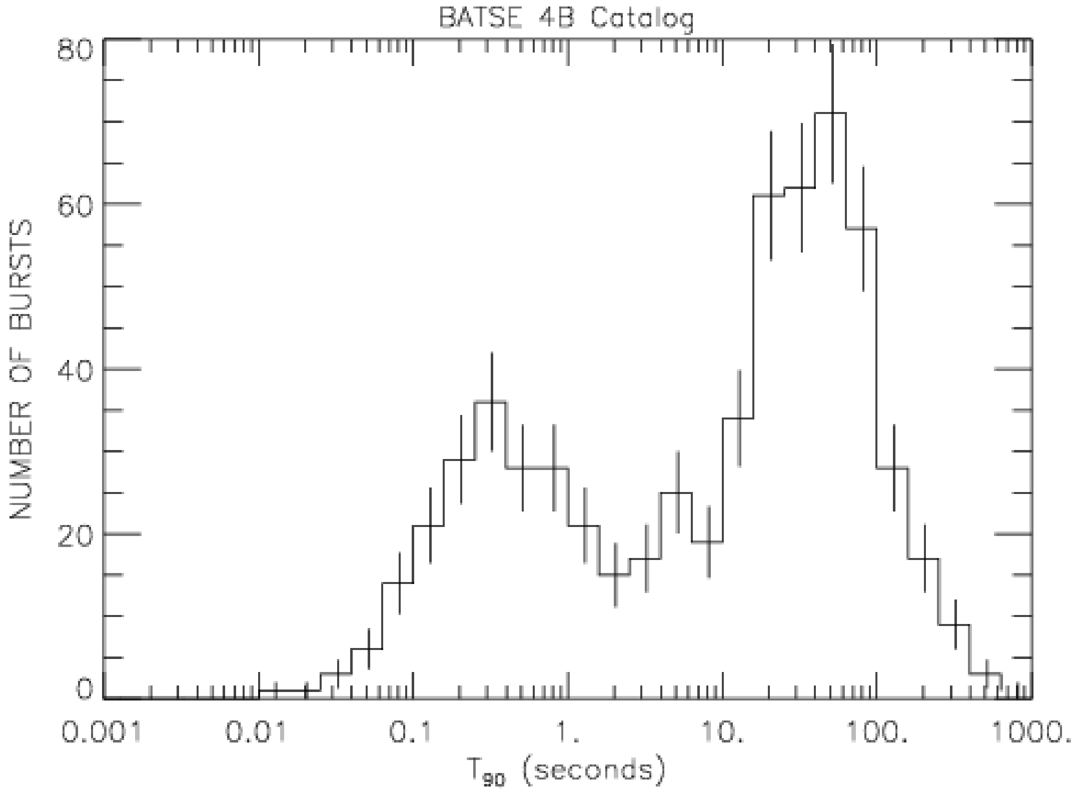

Figure 1.6: Distribution of GRB durations (T90). The duration of a burst is defined as the time interval within which 90% of the burst fluence is detected. They go from tens of milliseconds to thousands of seconds. A bimodal distribution is observed suggesting two different classes of bursts.

cminutes using a Wide Field Camera (WFC) sensitive from 2-30keV. This made possible to promptly slew the satellite in the found direction and then observe the region with its Narrow Field Instrument (NFI) in the energy range of 0.1-10keV. Thanks to the prompt dissemination of the coordinates through the Gamma-Ray Burst Coordinates Network (GCN), ground base telescopes pointed to the burst direction and detect optical, X-ray and radio afterglows 1.9. Two main important observations came from these fast follow-ups. One, the first redshift of a burst was measured. Second, breaks in optical afterglows were observed, like the one observed in GRB030226 (see figure 1.10).

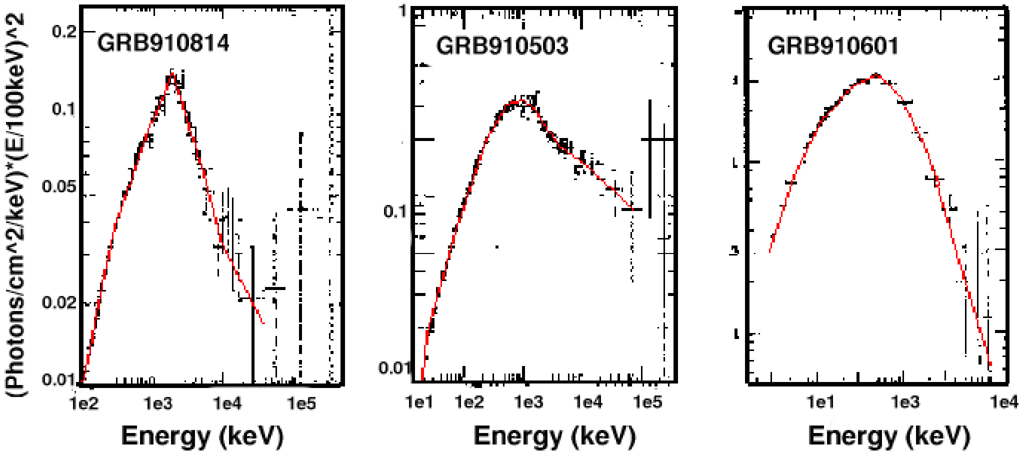

Figure 1.7: GRB spectra for three different bursts. All of them show the same features. The GRB spectrum is given as E^2dN/dE i.e., the energy flux per logarithm of energy unit. The GRB spectrum corresponds to non-thermal emission. It increases in energy reaching a maximum, and then decreases in energy. The maximum of the spectrum lies in the hundreds of keVs

Most of the observed bursts had X-ray afterglow, and only 60% of these had optical afterglow. Radio afterglows were detected in about half of all GRB afterglows.

1.2 Theory of GRBs

This section only summarizes the most relevant theories to the understanding of this thesis. For more details, see Reference [ME03] a great review on GRBs.

Although the observational facts are numerous, only the most important results to understand the basis of the Standard Fireball model were discussed in the previous section. They are summarized below.

- Prompt GRB emission is at energies of 100keV - 10MeV

- They do not repeat from the same direction.

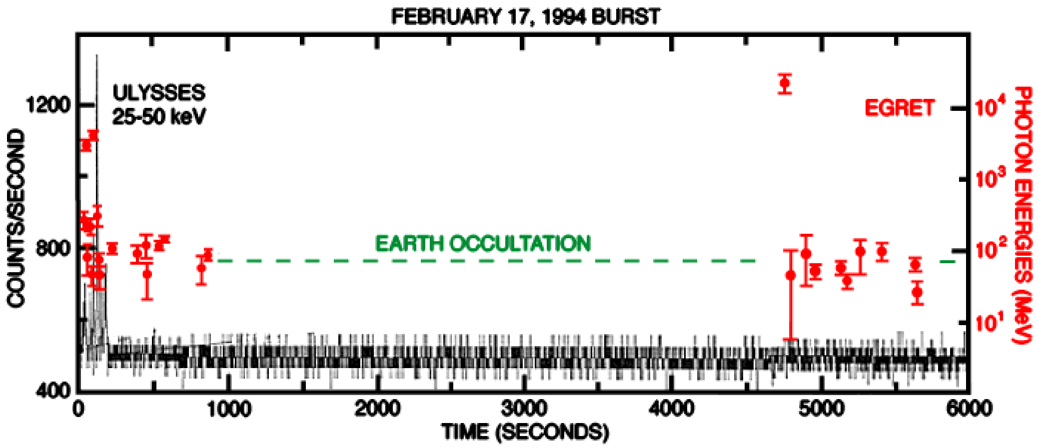

Figure 1.8: Prompt and delayed high energy emission from GRB940217. The prompt emission as observed by Ulisses in the energy range of 25-50keV is shown as solid black line. It lasted 150s. The red symbols represent every photon observed by EGRET. In the right side, the energy for each photon is given. It is observed that the high energy photons came even after thousand of seconds after the end of the prompt emission. Unfortunately the Earth occultation did not allow to follow the high energy emission for ∼4000s.

- There are extreme differences in burst morphologies. Some of them show strong variability. No periodicity has been observ.

- Time durations go from 30ms to 100s. It is possible to classify them as short or long with the dividing duration of ∼ 2 sec.

- The energy spectrum is continuous and definitely non-thermal.

- Some burst have emission beyond 10MeV.

- For some GRBs, counterparts in X,radio and optical wavelengths were measured.

- Lightcurve breaks were observed in some optical afterglows.

- They are at cosmological distances.

A theoretical understanding of gamma-ray burst will comprise a consistent site with

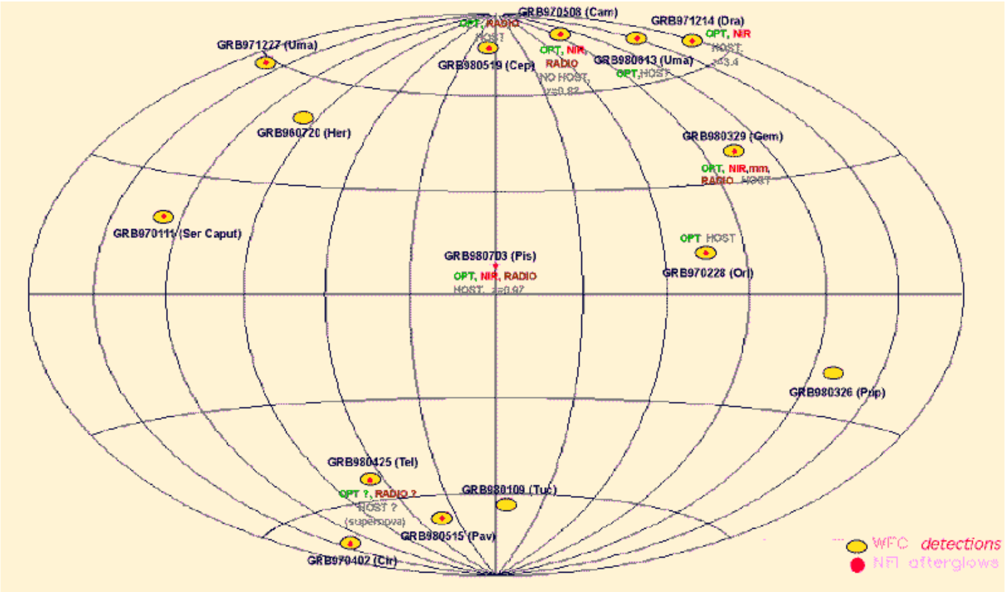

Figure 1.9: Map of GRB observed by BeppoSax in 1997-1998 with their associated afterglows. Yellow symbols represent Wide Field Camera detections. Red symbols indicate the positive detection of an X-ray afterglow by the BeppoSAX X-ray imaging telescopes. Detection of the afterglow at optical or radio wavelenghts is also reported when available. Most of the observed bursts had X-ray afterglow, and only 60% of these had optical afterglow. Radio afterglows were detected in about half of all GRB afterglows.

the observed isotropy and inhomogeneity, an energy source sufficient to produce the observed intensities for the distances assumed and emission mechanisms able to reproduce the time scales and the spectra observed.

Knowing that GRBs are at cosmological distances and the energy released in their prompt emission, it is possible to estimate the total energy released in a burst. The resulting value of $1{\times}10^{51-53}$erg plus the fact that GRBs do not repeat from the same direction, suggest the "deaths of stars" as the GRB progenitor. There are several models for the engines; the most popular ones involve merger of two compact objects such as neutron stars or black holes or, the core collapse of a very massive star. The merger of

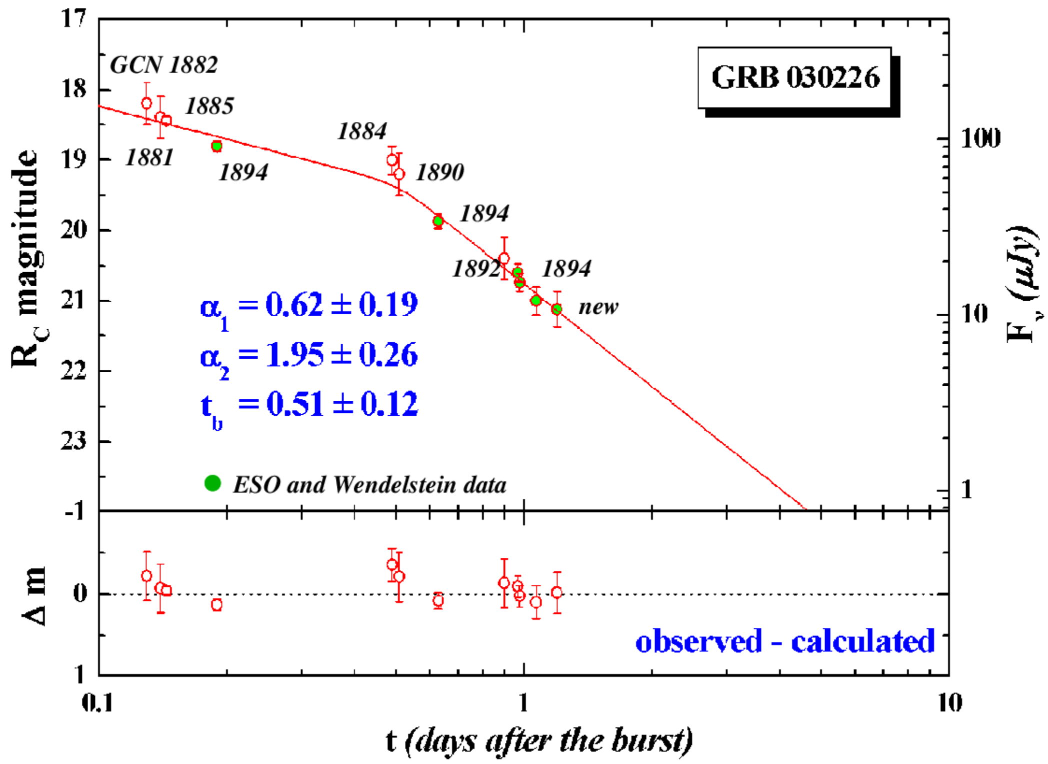

Figure 1.10: Observed optical afterglow for GRB030226. The optical lightcurve is described by a power law function with $\alpha_1 = -0.62$ and $\alpha_2 = -1.95$ as the power law indexes before and after $t_b = 0.5$ days, respectively. In other words, a lightcurve steepening was observed around ~0.5 days.

a binary system model is believed to be the progenitor of short bursts, while the core collapse model is believed to be the progenitor of long bursts. There are other GRB progenitors considered in the literature such as the magnetar (rapidly rotating neutron stars with surface magnetic fields) or core collapse of a neutron star to a strange star (these stars have been never observed).

Most models result in a black hole and a surrounding torus which is accretes on to the black hole. The energy sources considered in the models are the gravitational binding energy of the torus, the spin energy of the black hole and the magnetic energy. The different models give varying total energy, duration, variability, baryon loading, and birth rate among others. Therefore, the mechanisms of GRB prompt emission may help to uncover the mechanism that powers the central engine.

Ruderman [RU75] and Schmidt [SC78] independently argued that GRBs could not originate from cosmological distances because considering causality and the rapid temporal variability of gamma-ray bursts, the emission had to come from regions smaller than $\sim 10^6$km. Then, the high observed luminosity implies a high photon density fireball and therefore is opticall thick to photons. This was called the compactness problem. It was solved assuming relativistic motion of the radiative site.

The observed non-thermal GRB spectra imply radiative processes such as synchrotron radiation, Inverse Compton Scattering, Bremmstrahlung or hadronic showers as the responsible processes of the burst emission. This is not unusual in astrophysical phenomena. For instance, synchrotron radiation and Inverse Compton Scattering have been observed in active galactic nuclei and supernova remnants.

The break in the optical afterglow plus the fact that relativistic motion is needed lead to the probability that the burst emission was not isotropic but rather contained in a jet. Therefore, the observed break in the aftergloow light curve is a consequence of the beaming and the open angle of the jet. When the beaming angle is smaller than the jet angle, the observed region of the jet is determined by the beaming angle being bigger for deceleration of the jet. When the beaming angle is greater than the jet angle, the observed lightcurve decreases faster since it is not compensated by an increase of the observed region.

Almost all the elements to construct the Fireball model have been deduced. The remaining issue is to convert the kinetic energy of radiative region into internal energy of the radiative particles. This is solved by introducing Fermi acceleration in shock.

Therefore, cosmological gamma-ray bursts(GRB) are believed to be produced in the fireballs resulting from death of stars, when a large amount of energy is released over a few seconds in a small volume and with a small baryonic load (to reach the relativistic velocities). The energy is released in a collimated jet and eventually transferred to the baryons (mainly because they lose their energy slower than electrons) which are accelerated to ultra-relativistic velocities. A substantial fraction of the kinetic energy of the baryons is transferred to a non-thermal population of relativistic electrons through Fermi acceleration at the shocks. The accelerated electrons cool down via inverse Compton scattering and synchrotron emission in the post-shock magnetic fields and produce the hard X-ray emission observed in GRBs and their afterglows. Emission from Bremmstrahlung is negligible. External shocks arise from the interaction of the shell with the external matter after the fireball becomes optically thin. Internal shocks arise from collisions between fireball shells caused by source variability. This summarizes the Standar Fireball Model in its simplest version, see figure 1.11.

Synchrotron radiation in external shocks has been successful to explain broad band GRB afterglows. One observable consequence is that the emission from an individual

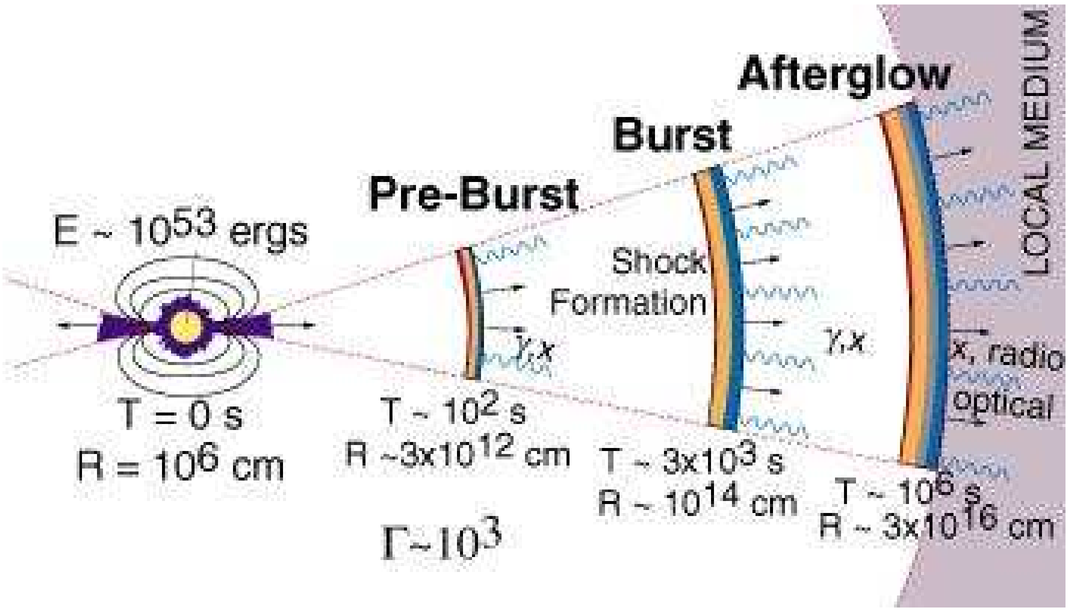

Figure 1.11: Cartoon of the Standar Fireball Model

particle is polarized, thus the afterglow emission should be partially polarized.

The shock scenario and the radiation process involved in the prompt keV-emission are unknown and topic of great debate. The internal shocks scenario reproduces the temporal profiles of GRB prompt emission lightcurves as consequence of the temporal behavior of the central engine. The relative Lorentz factor between internal shocks is one of the parameters in this scenario. It also requires a large relative Lorentz factor dispersion in the flow to explain the fact that the prompt emission is of the same order of the afterglow kinetic energy. It requires a strong bimodal distribution of Lorentz factors to explain the narrow E_{peak} (characteristic peak energy of the GRB spectra when described by a Band function, discussed later in this section) distribution within the same burst observed in BATSE bright bursts. Outflows with lower Lorentz factors imply higher E_{peak} values in the internal shocks scenario. In the other hand, external shocks scenario requires a clumpy interstellar medium to reproduce the spiky GRB lightcurves. The absolute Lorentz factor of the outflow is one of the parameters in this scenario. Some correlations between observables such as $\mathrm{E_{peak}}$, duration, flux, brightness, etc, are expected. Only a few of them have been observed. Contrary to internal shocks, outflows with lower Lorentz factors imply lower $\mathrm{E_{peak}}$ values in the external shock scenario. Internal and external shocks scenarios are not mutually exclusive and could coexist in all bursts but individually dominate in different bursts. Future observations may help to identify the shock scenario for the prompt emission.

Before discussing the radiation processes involved in the prompt emission, let's introduce some differential photon flux functions that are used to analyze and describe the prompt emission. The most common ones are the "Power Law" (PL, equation 1.1), "Smooth Broken Power Law" (SBPL, equation 1.2) and "Band function" (Band or GRB, equation 1.3). They are defined as follows:

"Power Law"

$$F_{PL} = A(\frac{E}{E_{piv}})^{\gamma} \tag{1.1}$$

where A is the amplitude in $\mathrm{photos/s-cm^2-keV}$, E_{piv} is the pivot energy in keV and, γ is the photon index.

"Smooth Broken Power Law"

$$m = \tfrac{\beta-\alpha}{2}$$

$$b = \frac{\alpha+\beta}{2}$$

$$d_{piv} = \frac{\log(E_{piv}/E_b)}{\Delta}$$

$$c_{piv} = m\Delta \ln \frac{(\exp d_{piv} + \exp - d_{piv})}{2}$$

$$d = \frac{\log(E/E_b)}{\Delta}$$

$$c = m\Delta \ln \frac{\exp(d) + \exp(-d)}{2}$$

$$F_{SBPL} = A(E/E_{piv})^b 10^{(c-c_{piv})} \tag{1.2}$$

where A is the amplitude in $\mathrm{photos/s-cm^2-keV}$, E_{piv} is the pivot energy in keV, E_b is the break energy in keV, Δ is the break scale in decades of energy, and α and β are the low and high energy spectral indexes respectively.

"Band function"

$$F_{Band} = A(\frac{E}{100})^{\alpha} \exp \frac{-E(2+\alpha)}{E_{peak}}$$

$$\text{if } E < (\alpha-\beta)E_{peak}/(2+\alpha),$$

$$F_{Band} = A(\frac{(\alpha-\beta)E_{peak}}{100(2+\alpha)})^{\alpha-\beta} \exp(\beta-\alpha)(E/100)^{\beta} \tag{1.3}$$

$$\text{if } E \geq (\alpha-\beta)E_{peak}/(2+\alpha)$$

where A is the amplitude in $\mathrm{photos/s-cm^2-keV}$, E_{peak} represents the peak energy and is in keV and, α and β the low and high energy spectral indexes respectively.

SBPL and Band functions are a summation of two power law functions smoothly jointed. The power law with spectral index α/β describes the spectra below/above the peak or break energy (E_{peak} or E_{break}). There is a simpler version of the SBPL called "Broken Power Law" (BPL). In general, the most used to described sub-MeV emission is the "Band function" and the "Power Law" for data above the peak energy (~1MeV) is only available. BATSE observed a temporal evolution of the spectral parameters. In general, they became more negative with time. This kind of behavior is called "hard to soft" evolution. Clearly the oposite is "soft to hard" evolution.

As mentioned before, the GRB afterglows are explained by synchrotron radiation. For the prompt emission, synchrotron radiation hardly explains several observational facts but well-describes many GRB spectra. If the GRB prompt spectra are due to synchrotron radiation, the low energy spectral index should not exceed the value of -2/3. This value is derived from the synchrotron single-particle emission spectrum and it is called the "line of death". Thus, a violation of the "line of death" implies that the low energy spectral index gets values below -2/3. Twenty three bursts from the BATSE catalog violate the "line of death" [PR98a]. There have been proposed ways to go around the "line of death" violation. For instance, some authors argue that BATSE sensitivity at energies of tens of keV is too low to give accurate low energy spectral indexes. Other authors had introduced a small-angle "jitter" radiation, anisotropic electron pitch angle distribution, synchrotron self-absorption and photospheric emission. But there is nothing conclusive. Another problem with the synchrotron radiation is that its cooling time scale is very short. This should be reflected in a value of -2/3 for the low or high spectral indices that is not apparent in the observations. Again, there are ways to go around this problem including complicated acceleration and cooling processes, but nothing conclusive. Although these and other problems with the synchrotron radiation, it is the leading radiation mechanism to interpret the prompt emission.

There have been considered other radiation mechanisms in the literature to understand the prompt emission. For example, it could be due to self-Inverse Compton scattering of synchrotron emission in the optical band. Different models could be tested by observing or not the dependences of E_{peak} with various parameters such as the redshift and the bulk Lorentz factor.

In section 1.1, the most relevant observations for the understanding of GRBs were discussed. It was mentioned that EGRET detected MeV-GeV photons for GRB940217. Some other detectors had observed emission above MeV energies for other bursts but most of them have been consistent with a continuation of the sub-MeV emission without cutoff. Since EGRET observations, several models for the high energy emission have been developed, mainly to explain the emission above GeV energies. These models can be grouped in two kinds, leptonic and hadronic. The first one is based on the Inverse Compton Scattering (IC) of electrons in different emission sites, while the hadronic, can be explain by proton synchrotron, π synchrotron emission and π decay from photo-meson and photo-pion interactions in different emission sites. In principle the following processes could emit in the GeV range or above.

- Electron self-Inverse Compton from the external forward shock.

- Electron self IC from the external reverse shock or the cross-IC between the reverse and the forward shocks.

- Electron self-IC from the internal shocks.

- Synchrotron proton emission in the external shock.

- Photon meson cascade emission from the external shocks.

- Proton synchrotron and photon meson cascade from the internal shocks.

- Cascade emission resulting from pn in elastic collision during the early face of the fireball evolution, when the neutrons decouples from the protons.

- Baryonic photosphere component (and possible its comptonization component).

The above is not an exhaustive list and not all the above processes may be operative at any time over all models. The present high-energy observations are not conclusive enough to reject or validate any of these processes. In order to improve our knowledge in high energy GRB emission, this thesis focuses on a further analysis of EGRET data.

There are several radiation and particle emissions (such as neutrinos, gravitational waves or afterglows) that have been not discussed in this section because they are beyond the scope of this thesis. But a wide review can be found in the reference [ME03].

1.3 Last Results. 2003 - 2004

Last section was dedicated to introduce the fireball model as a result of the most relevant observations previous to 2003. It was until 2003 that some of the expected consequences of the Fireball model were undoubtedly observed. Two main examples are the super nova connection [ME03a, HJ03] and the polarized prompt emission [CA03].

Observation of afterglows had yielded tantalizing hints that supernova and GRBs are related. The case was circumstantial though relaying on irregularities in the lightcurve or the colors of the afterglow. Another indication of the supernova connection was GRB980425 because a peculiar type of Ic supernova, SN1998bw, was observed consistent with the burst direction. GRB030329 provided the first firm evidence of this connection. The burst was very bright at a redshift of 0.1685. The observed optical afterglow was typical for a burst. It started to show peaks typical for a supernova 7.67 days after the burst trigger that brighten with time. The optical afterglow was similar to the emission of SN1998bw. Observing the initial afterglow evolving in to the emission of a supernova was crucial to relate both phenomena.

It was reported the discovery of linear polarization in the prompt gamma-ray emission from GRB021206, indicating that it is synchrotron emission from relativistic electrons in a strong magnetic field the responsible radiation mechanism. The polarization was at the theoretical maximum requiring a uniform, large-scale magnetic field. Such a field constrains possible progenitors to those either having or producing organized fields. A large magnetic energy densities in the progenitor environment (comparable to the kinetic energy densities of the fireball), combined with the large-scale structure of the field were suggested, indicating that magnetic fields drive the GRB explosion.

The Fireball model is not fully complete and many issues remain unclear, but certainly observing direct predictions of the model shows that it is going in the right direction.

1.4 Goals of this thesis

As mentioned in section 1.1, the Burst and Transient Source Experiment, BATSE observed the largest GRB data set with excellent energy and time resolution at keV energies. One of the general results from these observations (discussed in section 1.1) was the non-thermal nature of the GRB spectra and the ability to fit most of them with the "Band function". A series of papers, [BA93, FO95, PR96, PR98, PR00], etc, were dedicated to the detailed analysis of the GRB spectra using BATSE data. The results relevant to this thesis are summarized below.

In reference [BA93], the global properties of the GRB spectra averaged over entire burst and in the energy range of $\sim 0.01 - 2$MeV were studied for 54 bursts. The "Band function" was proposed as a 4-parameter function to describe GRB spectra. No universal parameters for all bursts were found, the need of the high-energy power law component was required for an appropriate description of the GRB spectra, and no correlation between the Band function parameters were found or with GRB properties such as the hardness or location. An interesting observation in that analysis was the influence of the detector sensitivity and the energy range used to constrain the high-energy spectral index (β) and to determine the peak energy (E_{peak}). The uncertainty in β was much bigger than the one for the spectral index of the low-energy power law, α; and the determination of E_{peak} was biased by the energy range selected in the analysis.

In reference [FO95], the temporal evolution of the peak energy and its relation with the bursts intensity (or count rate) in 37 long, bright GRBs were studied in the energy range of 0.015-1.5MeV. It was found that E_{peak} is coupled with the intensity of the burst, either leading or accompanying intensity increases, but is apparently modulated by an envelope decaying in time. In that analysis the determination of E_{peak} was worse than in reference [BA93] because the required time resolution lowered the signal-to-noise ratio in every spectrum. A balance between these two effects decreased the number of bursts in the analysis.

An extensive analysis of the temporal evolution of the GRB spectra was done by [PR98, PR00] for bright bursts using BATSE data in the energy range of 0.028-1.8MeV. A set of 126 and 156 bursts (respectively) were selected by either their high fluence or photon flux. The distribution of the low-energy spectral index (α) is found to be centered at -1 and broad enough to include values above -2/3 where synchrotron emission alone may not be the responsible radiation process. The distribution of the high-energy spectral index (β) was found to be asymmetric with a higher contribution to more negative values and peaking at -2.25. The peak energy (E_{peak}) was shown to be mainly constrained in a decade of energy peaking at $\sim$ 220keV. Sixty six percent of the bursts showed a high-energy spectral index inconsistent with being constant through the burst duration. Predominantly the GRB showed hard-to-soft evolution. No correlation between the temporal behaviors of the other parameters was found. These analyses had the same restrictions as those described above. It is interesting to point out that in 10% of the cases a spectral model other than a "Band model" model is needed, since in previous analyses the "Band model" was shown to be sufficient to describe all GRB spectra. This need came from the fact that the peak energy was above the BATSE energy range resulting in an ill defined or too negative β, and that the "Band model" was not able to described sharp curvatures in the spectra. Physical implications may be derived from the existence of spectra with sharp curvature; however it could be another consequence of the detector sensitivity.

In section 1.2, the different explanations for the prompt emission and the importance of describing the non-thermal GRB spectra to constrain the radiation processes, the magnetic fields, Lorentz factors, redshifts and acceleration processes involved were discussed. BATSE observations are a huge step toward this goal. Empirical laws (for details refer to [ZH03]) and a large set of BATSE bursts have been found to support the most "natural" and accepted emission process, which is the synchrotron emission in either internal or external shocks. However BATSE results have also shown the violation of the "line of death" [PR98a] by some bursts as well as a narrow peak energy distribution that contradicts the synchrotron model consequences (see section 1.2). Some authors [LL00] had explained the violation of the "line of death" as a consequence of the BATSE detector sensitivity to determine accurate low energy spectral indexes at such low energies. Also the narrow peak energy distribution was concluded to be intrinsic to the GRB spectra by studying data in the energy range of 0.8-10MeV from the Solar Maximum Mission (SMM) Gamma Ray Spectrometer. Certainly, both assumptions can be tested by experiments more sensitive over broader energy range. The observed temporal evolution of the high energy spectral index contradicts the constant and less than -2.2 predicted β obtained from relativistic Fermi particle acceleration [GA99]. As discussed above, the determination of β and consequently of its temporal evolution had problems for bursts with peak energies in the higher part of BATSE energy sensitivity, therefore a better study of β for these bursts is necessary over a broader energy range.

The GRB spectrum does not seem to have a cut off or a change of the spectral index after the peak energy at least up to 1MeV as BATSE showed. Even more, experimental results such as the long-lived GeV emission detected in GRB940217 [HU94], the averaged spectra above 100MeV over 200 seconds of 4 bursts observed by EGRET spark chambers [DI01] and the 175 bursts observed by SMM [SH92] in the energy range of 0.8-10MeV, were shown to be consistent with a continuation of the Band spectrum observed at keV-energies. The only experimental observation that hints to a change in the GRB spectra is the 3σ burst observed by Milagrito, GRB970417, at energies near 1TeV. In fact, it suggested the existence of a spectral component that can be explained by self-Compton emission related to the Band spectrum at keV energies as discussed in section 1.2. The Milagro detector has not observed this TeV emission in any other burst or self-triggered on any TeV-burst in its almost 3 years of operation [AT04]. Therefore, where the GRB spectra end and if a different spectral component exists, are still open questions.

The progress in understanding the GRB prompt emission achieved with the detailed analysis of the GRB spectra has been discussed. The resulting paradigms and the remaining open questions have also been explained. It is clear that studies of the GRB spectra in a broader energy range are needed. Some up coming experiments such as GLAST that will operate in the energy range 10keV-300GeV or running ones such as Milagro, may contribute to our understanding, but in the meantime existent data may complement our knowledge and surprise us.

The goal of this thesis is to use the existent data from the EGRET experiment to extend and analyze the GRB spectra from 20keV up to 30GeV. Therefore, different selections in the BATSE bursts are applied to increase the chance of detecting them by EGRET. The goals of this thesis are going to be achieved in the following way. In the second chapter limits of a probable long-lived emission similar to the one observed in GRB940217 are set for different duration times using the EGRET spark chambers. In the third chapter, a complementary analysis to the one [PR98, PR00] performed by the BATSE team is carried out. Data from the EGRET calorimeter, TASC, is used to extend the GRB spectra up to $\sim$200MeV for a better determination of the peak energy and the high-energy spectral index as well as their temporal evolution. The fourth chapter is a consequence of the results in the third chapter. A new, unexpected, high-energy spectral component is clearly seen in one of the bursts. This component evolves with time completely independent to the keV-component and lasts longer. It keeps a constant spectral index of -1 and contains 2 times the energy in the keV-component. In chapter fourth, this new component is searched for in other bursts and limits in its extension in energy are addressed by using data from the spark chambers.

Chapter 2

Upper limits to the GRB's emission at 30MeV-30GeV

The EGRET spark chamber detector observed significant emission in the energy range of 0.03-30GeV from four of the brightest BATSE bursts. These bursts were GRB910503 [SC92], GRB930131 [SO94], GRB940217 [HU94] and GRB940301 [SC95]. Most of their emission above 30MeV was within T90 (as defined by their sub-MeV emission) and its detection at longer times was marginal for most of them. For three of these bursts, EGRET observed photons after T90 consistent with the bursts direction. For instance, GRB910503 had a 9.6GeV gamma-ray 84s after the burst trigger (T90 is 50s) and, GRB930131 had four gamma-rays after T90 (19s) and before 200s after the burst trigger. The most significant EGRET observation of long-lived emission above 30MeV was the gamma-ray up to 18GeV over an hour after the beginning of GRB970217. Although the duration of the emission above 30MeV was not determined, the observed photons at longer times hinted to a high-energy emission above 30MeV simultaneous and longer than the observed sub-MeV emission.

Emission above 30MeV has been studied by [DI95, DI01, DI98, DI01b] for the brightest bursts, as defined by sub-MeV flux and fluence, in EGRET's field of view. Limits to these burst's energy fluences have been calculated for T90 [DI01b]. Also, [DI01, DI95] have searched for significant detection in 200s, 1000s and one hour after the BATSE trigger for some bursts. The goal of this chapter is to constrain the high-energy emission for all bursts detected and not detected by EGRET but in its field of view. Therefore, limits to the energy fluence released in the energy range of 30MeV-30GeV are calculated in a systematic way and with slightly different considerations to that reported in the literature. The calculation assumes different durations of the high-energy emission.

2.1 EGRET-Spark Chambers

Detailed descriptions of the instrument are given by [KA88, HA92]. Also, details of the instrument calibration, before and after launch, are given by [NO92, TH93]. Therefore only a brief description of EGRET is given in this section since a detailed description is not relevant for this analysis.

The Energetic Gamma-Ray Experiment Telescope was one of the four detectors of CGRO. EGRET was formed of an anticoincidence system to discriminate against charged particle radiation, a multilevel thin-plate spark chamber system to convert gamma rays and determine the trajectories of the secondary electron-positron pair, a triggering telescope of a four by four scintillator array of two levels that detects the presence of the pair with the correct direction of the motion, and an energy measuring calorimeter of NaI(Tl) crystal, TASC. A schematic diagram of EGRET is given in figure 2.1.

EGRET was able to determine the energy and direction of gamma-rays in the energy range of 30MeV-30GeV. The energy resolution was approximately 20% FWHM over the energy range. EGRET's effective area was 1500cm^2 between 200 MeV and 1000 MeV, falling at higher and lower energies. The efficiency decreased with angle off axis dropping to about half the on-axis value of 18^o, and one sixth by 30^o. The angular resolution was strongly energy dependent, with a 67% confinement angle of 5.5^o at 100 MeV, falling to 0.5^o at 5 GeV on axis; bright gamma-ray sources were localized with approximately 10arcmin accuracy. The timing accuracy was 0.1ms and the dead time per trigger was 100ms. All events triggered were scrutinized to determine if the tracks and energy deposition were consistent with a gamma-ray and not the more plentiful charged particle background.

2.2 Methodology

2.2.1 Data and software

All EGRET data is available from the web page ftp://cossc.gsfc.nasa.gov/pub/data/egret/. Beginning in Cycle 6, an alternate procedure was followed to extend the life of EGRET, wherein observations were minimized and used only the central telescopes, or at most a subset of the total sub-telescopes. Therefore, only EGRET data up to cycle 6.0 were included in the analysis.

To select BATSE bursts in the field of view of EGRET, they were required to have an incoming angle less than 40 degrees off the CGRO axis (as determined by BATSE) and a BATSE angular error less than 5 degrees. Several bursts were excluded from this

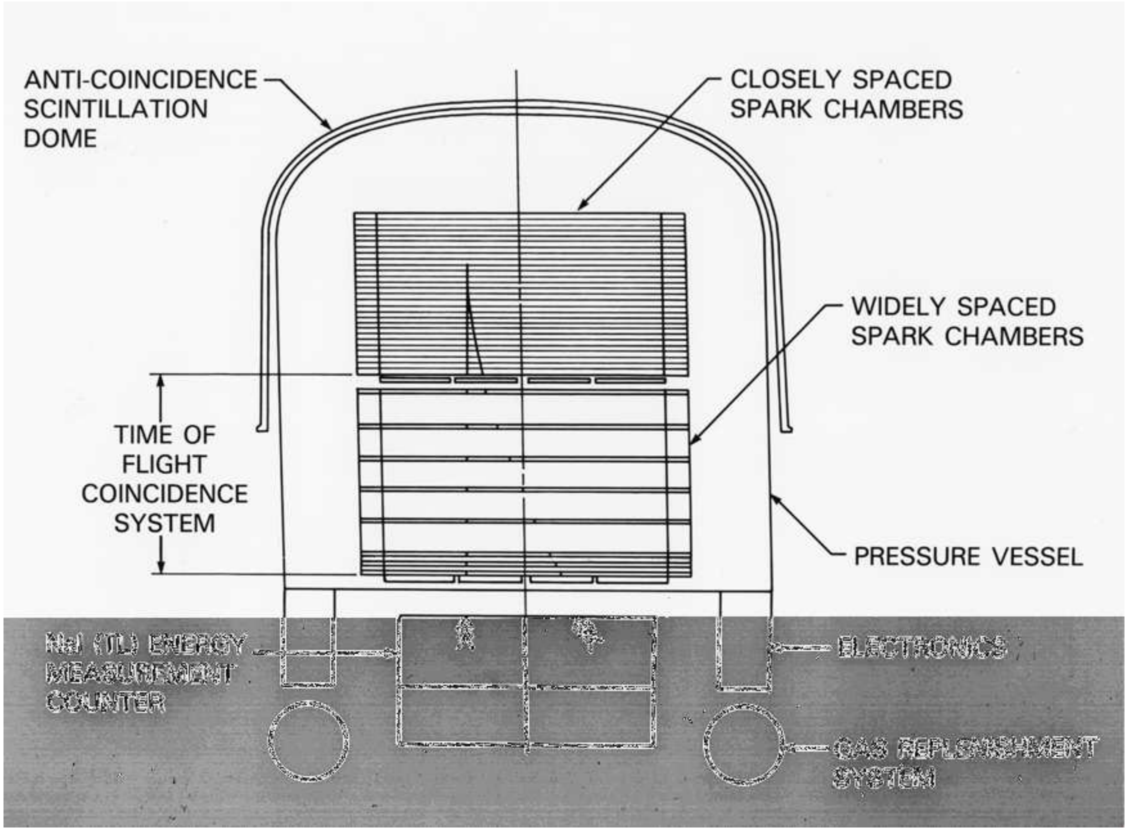

Figure 2.1: Schematic description of the EGRET instrument

analysis when their T90 and BATSE fluence were not available in the BATSE catalog because of data gaps or when their EGRET exposure was zero. The included bursts in this analysis are shown in Tables 2.1 and 2.2.

The determination of the exposure is especially complex for EGRET. The telescope was divided into 96 sub-telescopes that were organized into groups that pointed in 9 different directions. During any orbit, the directional groups were dynamically commanded "off" and "on" depending on whether or not the Earth was in the field of view for that direction. Typically the determination of exposure involves integrating the product of live-time, detection efficiency, and solid angle for each bin on the sky, considering the time varying mode changes. An exposure history database contains pointing and instrument mode information needed for determining the exposure maps. The "xpose" software uses the database to compute the exposure of a single burst direction for a given time interval. This software is given by the EGRET team in the web page [EGRETdoc]. The exposure integrated oven energy depends on the differential photon spectral index which was chosen to be -2.4.

Table 2.1: Upper Limits For EGRET Energy Fluences. They were calculated for the energy range of 30MeV-30GeV and confidence level of 90%. The values in the three first columns were taken from the BATSE Catalog. The upper limits were calculated for different time windows. The fourth column refers to the upper limit in T90 as defined by BATSE. The last seven columns refer to time windows following T90. They are also plotted in figures 2.3-2.8.

date	BATSE	T90	UPPER LIMITS FOR EGRET ENERGY FLUENCES (erg/cm^2)							
	fluence	(s)	T90	10s	20s	50s	100	200s	500s	10000s
910503	2.92E-04	50.82	3.23E-06	2.84E-06	2.75E-06	4.80E-06	4.34E-06	5.30E-06	9.27E-06	9.41E-06
930131	6.66E-05	19.20	3.15E-05	1.31E-05	1.30E-05	1.29E-05	2.19E-05	2.49E-05	2.32E-05	2.47E-05
940619	6.00E-05	88.45	3.29E-06	—	—	—	—	—	—	—
911118	5.90E-05	19.20	2.02E-05	6.71E-05	1.07E-04	1.67E-04	2.04E-04	4.13E-04	4.46E-04	6.83E-04
950522	4.43E-05	59.07	4.78E-06	2.86E-05	2.86E-05	2.84E-05	5.06E-05	4.98E-05	1.37E-04	8.06E-05
920627	3.53E-05	52.80	2.46E-06	1.33E-05	1.32E-05	1.30E-05	1.25E-05	1.17E-05	9.73E-06	3.32E-05
940520	3.41E-05	32.83	1.52E-06	5.05E-06	5.03E-06	4.95E-06	4.80E-06	4.53E-06	1.70E-05	5.65E-06
930309	2.84E-05	90.11	7.88E-07	8.04E-06	7.91E-06	7.57E-06	1.34E-05	2.26E-05	1.92E-05	2.21E-05
960524	2.62E-05	80.64	4.89E-06	3.97E-05	3.97E-05	3.96E-05	3.94E-05	3.89E-05	3.78E-05	3.58E-05
920617	2.48E-05	67.71	1.63E-06	1.16E-05	1.16E-05	1.13E-05	1.13E-05	1.20E-05	1.15E-05	2.15E-05
931222	2.38E-05	57.66	6.05E-07	3.61E-06	3.58E-06	3.50E-06	3.37E-06	3.10E-06	9.75E-06	1.07E-05
930612	2.22E-05	41.98	4.04E-05	3.16E-04	3.16E-04	5.52E-04	5.13E-04	5.58E-04	1.40E-03	2.79E-03
940128	2.20E-05	45.25	3.93E-06	1.79E-05	1.79E-05	1.78E-05	2.62E-05	6.32E-05	9.13E-05	1.83E-04
941128	1.62E-05	108.51	3.26E-07	3.66E-06	3.65E-06	3.61E-06	3.55E-06	3.42E-06	3.02E-06	7.68E-06
960912	1.47E-05	19.46	8.98E-06	1.75E-05	1.75E-05	1.73E-05	1.72E-05	1.67E-05	1.60E-05	1.77E-05
921227	1.26E-05	26.05	3.42E-06	8.98E-06	8.95E-06	8.84E-06	8.61E-06	3.34E-05	1.54E-05	1.36E-05
940826	1.11E-05	5.18	5.61E-05	2.91E-05	2.89E-05	2.88E-05	3.57E-05	4.23E-05	8.48E-05	1.69E-04
950111	1.08E-05	102.91	3.46E-06	3.58E-05	3.58E-05	3.56E-05	3.55E-05	6.34E-05	5.38E-05	4.79E-05
940622	8.93E-06	3.63	2.27E-05	8.19E-06	8.12E-06	7.99E-06	1.18E-05	2.17E-05	5.41E-05	1.08E-04
930720	8.19E-06	35.01	2.72E-06	9.63E-06	9.59E-06	9.43E-06	9.23E-06	8.79E-06	7.52E-06	1.67E-05
910717	7.72E-06	4.86	1.73E-05	8.32E-06	8.11E-06	7.48E-06	6.46E-06	5.27E-06	1.10E-05	4.91E-06
910523	7.12E-06	73.09	4.24E-07	3.66E-06	3.57E-06	3.30E-06	2.86E-06	4.94E-06	8.78E-06	4.57E-06

Table 2.1: *continued*

date	BATSE fluence	T90 (s)	UPPER LIMITS FOR EGRET ENERGY FLUENCES (erg/cm^2) T90	10s	20s	50s	100	200s	500s	10000s
930614	6.86E-06	140.06	1.30E-06	1.75E-05	1.75E-05	1.74E-05	1.73E-05	1.46E-05	1.23E-05	1.03E-05
910621	6.44E-06	85.44	2.48E-06	2.18E-05	2.17E-05	2.16E-05	2.11E-05	2.03E-05	3.52E-05	4.52E-05
910609	6.28E-06	0.46	1.12E-04	9.12E-06	8.99E-06	8.80E-06	1.16E-05	1.05E-05	1.22E-05	2.24E-05
930606	6.17E-06	67.84	7.99E-07	5.62E-06	5.58E-06	5.41E-06	9.66E-06	9.15E-06	7.54E-06	1.35E-05
910501	5.74E-06	182.02	2.26E-06	2.38E-05	2.37E-05	2.34E-05	2.30E-05	2.20E-05	1.94E-05	3.65E-05
920925	5.47E-06	14.02	2.39E-05	3.41E-05	3.45E-05	3.46E-05	3.47E-05	4.22E-05	8.69E-05	1.74E-04
931226	5.42E-06	124.86	3.17E-07	4.28E-06	4.26E-06	4.17E-06	4.03E-06	3.75E-06	9.06E-06	1.03E-05
911221	3.78E-06	27.71	7.07E-06	1.98E-05	1.97E-05	1.93E-05	1.88E-05	1.77E-05	1.46E-05	4.95E-05
960409	3.55E-06	25.86	8.25E-04	2.13E-03	2.13E-03	2.13E-03	2.13E-03	2.13E-03	2.13E-03	2.12E-03
960129	3.40E-06	51.68	3.62E-06	—	—	—	—	—	—	—
911219	3.28E-06	23.74	3.19E-06	7.66E-06	7.60E-06	7.37E-06	1.31E-05	1.24E-05	1.02E-05	1.64E-05
941114	3.25E-06	45.82	1.74E-05	8.02E-05	8.02E-05	7.99E-05	7.96E-05	7.93E-05	7.76E-05	7.65E-05
910730	3.16E-06	56.06	3.24E-06	1.87E-05	1.86E-05	1.83E-05	1.76E-05	1.65E-05	2.78E-05	3.40E-05
920804	2.99E-06	52.16	8.19E-06	4.33E-05	4.31E-05	4.25E-05	4.11E-05	7.26E-05	7.03E-05	3.44E-05
940219	2.99E-06	0.68	5.65E-03	2.97E-04	4.89E-04	4.67E-04	3.13E-04	8.69E-06	7.63E-06	6.08E-06
950317	2.96E-06	19.81	4.85E-04	7.91E-03	7.91E-03	7.91E-03	7.91E-03	7.91E-03	7.91E-03	7.91E-03
910517	2.10E-06	62.66	2.67E-06	1.75E-05	1.75E-05	1.71E-05	1.65E-05	1.59E-05	3.56E-05	6.90E-05
920714	1.97E-06	23.74	3.35E-06	8.16E-06	1.47E-05	1.43E-05	1.35E-05	1.20E-05	2.22E-05	2.03E-05
951030	1.93E-06	12.48	7.00E-05	8.73E-05	8.73E-05	8.70E-05	8.62E-05	8.55E-05	8.23E-05	7.76E-05
930127	1.77E-06	61.38	3.64E-06	2.29E-05	2.28E-05	2.25E-05	2.20E-05	3.92E-05	5.25E-05	6.00E-05
921206	1.66E-06	21.89	1.52E-06	3.45E-06	3.36E-06	3.07E-06	2.62E-06	4.45E-06	5.97E-06	5.10E-06
941012	1.64E-06	20.93	6.55E-05	6.06E-05	6.03E-05	6.01E-05	5.93E-05	6.11E-05	7.56E-05	1.51E-04
940111	1.63E-06	20.54	1.20E-04	2.47E-04	2.47E-04	3.68E-04	6.77E-04	1.23E-03	3.07E-03	6.14E-03
940427	1.41E-06	4.86	7.68E-06	3.70E-06	3.66E-06	3.52E-06	3.29E-06	2.82E-06	4.48E-06	5.72E-06
940602	1.17E-06	9.92	4.94E-05	4.90E-05	4.90E-05	4.88E-05	4.86E-05	7.12E-05	5.73E-05	5.88E-05
960812	9.30E-07	8.06	2.46E-05	1.97E-05	1.97E-05	1.95E-05	1.91E-05	1.85E-05	1.68E-05	2.25E-05
960819	9.11E-07	28.77	3.76E-05	1.13E-04	1.13E-04	1.12E-04	1.12E-04	1.11E-04	1.10E-04	1.06E-04

Table 2.1: *continued*

date	BATSE fluence	T90 (s)	UPPER LIMITS FOR EGRET ENERGY FLUENCES (erg/cm^2)							
			T90	10s	20s	50s	100	200s	500s	10000s
910802	8.93E-07	1.47	7.26E-05	1.06E-05	1.05E-05	1.04E-05	1.01E-05	9.53E-06	1.62E-05	1.90E-05
950916	8.92E-07	22.02	3.42E-05	7.53E-05	4.44E-05	3.52E-05	3.27E-05	3.10E-05	2.82E-05	3.18E-05
950612	7.60E-07	0.70	3.53E-04	2.46E-05	2.45E-05	2.41E-05	2.36E-05	2.25E-05	2.03E-05	2.66E-05
930102	7.36E-07	7.17	1.65E-05	1.18E-05	1.18E-05	1.17E-05	1.23E-05	1.23E-05	2.71E-05	5.42E-05
910717	5.51E-07	0.51	9.69E-04	4.92E-05	4.90E-05	4.86E-05	1.97E-05	9.69E-06	2.86E-05	2.96E-05
910526	4.81E-07	12.35	4.29E-06	5.32E-06	5.23E-06	4.92E-06	4.38E-06	7.78E-06	1.15E-05	1.94E-05
930903	3.18E-07	0.36	2.81E-04	9.95E-06	9.74E-06	1.72E-05	1.63E-05	1.45E-05	1.55E-05	8.66E-06
940706	0.00E+00	23.65	4.38E-06	1.04E-05	1.04E-05	1.02E-05	1.00E-05	9.54E-06	1.14E-05	2.27E-05
940217	6.62E-04	150.14	6.02E-07	1.79E-06	1.77E-06	3.14E-06	3.05E-06	2.88E-06	5.49E-06	6.74E-06
910601	1.50E-04	28.54	7.86E-07	3.38E-06	4.16E-06	4.50E-06	3.91E-06	7.04E-06	1.36E-05	2.71E-05
940301	1.12E-04	42.50	1.87E-06	1.54E-06	1.51E-06	1.42E-06	1.27E-06	1.09E-06	1.55E-06	4.38E-06
940708	8.17E-05	66.98	7.65E-07	2.11E-06	2.03E-06	1.77E-06	1.49E-06	4.64E-06	2.58E-06	3.34E-06
910627	2.12E-05	15.17	1.51E-06	2.32E-06	2.27E-06	4.01E-06	6.77E-06	6.88E-06	4.15E-06	3.02E-06
931106	2.04E-05	152.06	3.03E-07	2.80E-06	2.78E-06	2.69E-06	2.53E-06	2.24E-06	7.75E-06	1.55E-05
941023	1.68E-05	34.88	3.56E-05	1.24E-04	1.24E-04	1.24E-04	1.24E-04	1.60E-05	1.01E-05	1.85E-05
930704	1.41E-05	144.93	2.96E-05	4.29E-04	4.29E-04	4.29E-04	4.29E-04	7.68E-04	8.59E-04	1.46E-03
940728	1.08E-05	37.38	7.16E-07	2.73E-06	2.71E-06	2.66E-06	2.55E-06	4.50E-06	5.42E-06	1.03E-05
950625	1.01E-05	26.50	7.76E-05	2.06E-04	2.04E-04	1.92E-04	1.88E-04	1.16E-05	2.29E-05	1.48E-05
920830	9.17E-06	17.34	1.30E-06	2.28E-06	2.24E-06	2.10E-06	1.88E-06	1.57E-06	9.28E-07	2.49E-06
950421	8.67E-06	19.20	4.27E-06	8.22E-06	1.11E-05	1.11E-05	1.10E-05	1.36E-05	1.30E-05	1.74E-05
940722	5.92E-06	89.34	3.45E-06	5.61E-05	5.51E-05	2.09E-05	1.48E-05	8.10E-06	3.79E-06	2.67E-06
930214	4.60E-06	25.28	8.63E-07	2.25E-06	2.21E-06	2.07E-06	3.66E-06	4.68E-06	4.74E-06	3.59E-06
930819	4.41E-06	38.08	7.28E-07	2.53E-06	2.46E-06	2.27E-06	1.91E-06	1.56E-06	3.18E-06	2.30E-06
950417	2.61E-06	19.90	2.11E-06	4.23E-06	4.19E-06	4.09E-06	3.91E-06	3.58E-06	5.91E-06	1.02E-05
931206	2.58E-06	5.38	5.16E-06	2.74E-06	2.68E-06	2.47E-06	4.08E-06	3.31E-06	3.03E-06	7.90E-06
930506	1.81E-06	0.80	2.03E-05	1.53E-06	2.72E-06	2.39E-06	2.90E-06	1.96E-06	4.09E-06	8.24E-06
921214	1.68E-06	0.22	5.84E-05	1.14E-06	9.82E-07	2.37E-06	1.66E-06	1.59E-06	1.59E-06	6.63E-07

Table 2.1: *continued*

date	BATSE fluence	T90 (s)	UPPER LIMITS FOR EGRET ENERGY FLUENCES (erg/cm^2) T90	10s	20s	50s	100	200s	500s	10000s
951030	1.66E-06	1.74	2.34E-05	3.98E-06	3.90E-06	3.60E-06	3.11E-06	2.55E-06	3.26E-06	3.86E-06
930106	1.54E-06	15.30	1.70E-06	2.62E-06	2.59E-06	2.49E-06	6.11E-06	5.77E-06	4.76E-06	3.23E-06
940823	1.38E-06	49.25	7.12E-07	3.86E-06	3.76E-06	3.50E-06	3.57E-06	3.52E-06	5.04E-06	1.01E-05
910602	1.28E-06	0.38	4.50E-05	1.63E-06	1.54E-06	1.28E-06	2.19E-06	2.42E-06	1.39E-06	3.67E-06
910718	1.01E-06	0.25	7.64E-05	1.72E-06	1.52E-06	1.14E-06	4.77E-06	1.01E-05	9.99E-06	2.18E-05
960813	1.01E-06	20.10	2.18E-06	4.46E-06	4.39E-06	4.16E-06	3.81E-06	3.21E-06	2.03E-06	5.52E-06
920508	8.21E-07	0.38	5.85E-05	2.18E-06	2.15E-06	2.03E-06	1.84E-06	3.22E-06	2.25E-06	4.33E-06
911127	7.21E-07	18.11	1.32E-06	2.48E-06	2.36E-06	2.01E-06	1.66E-06	9.70E-07	8.62E-07	1.30E-06
941230	6.84E-07	1.25	3.50E-05	4.35E-06	4.32E-06	4.23E-06	5.01E-06	5.83E-06	1.15E-05	2.29E-05
911225	6.53E-07	6.08	9.82E-06	5.92E-06	5.75E-06	5.27E-06	6.18E-06	3.80E-06	6.08E-06	1.13E-05
930820	3.49E-07	36.51	6.72E-07	2.80E-06	2.67E-06	2.28E-06	5.81E-06	5.79E-06	7.66E-06	1.17E-05
940226	2.69E-07	1.26	1.07E-05	1.32E-06	1.28E-06	1.17E-06	1.00E-06	7.94E-07	9.50E-07	1.01E-06
930922	2.43E-07	0.13	1.61E-02	5.50E-06	5.41E-06	5.21E-06	4.91E-06	3.57E-06	3.99E-06	1.26E-06
940223	1.33E-07	2.75	1.30E-05	3.57E-06	3.53E-06	3.42E-06	3.23E-06	2.44E-06	3.05E-06	4.93E-06
930614	6.23E-08	0.13	6.17E-02	8.02E-04	8.02E-04	8.02E-04	8.02E-04	7.98E-04	7.98E-04	3.31E-05
940728	0.00E+00	31.23	1.02E-04	3.17E-04	3.17E-04	3.17E-04	3.17E-04	3.33E-04	4.09E-04	6.69E-04
950317	0.00E+00	0.13	3.76E-04	4.84E-06	4.78E-06	4.64E-06	8.26E-06	7.74E-06	7.96E-06	1.59E-05
940314	0.00E+00	70.34	2.42E-07	1.87E-06	1.85E-06	1.76E-06	1.61E-06	1.37E-06	2.06E-06	3.23E-06
920610	0.00E+00	4.22	4.54E-06	1.90E-06	1.86E-06	1.76E-06	1.58E-06	1.33E-06	7.79E-07	7.95E-07

Table 2.2: Lower Limits For EGRET Energy Fluences. They were calculated for the energy range of 30MeV-30GeV and confidence level of 90%. The values in the three first columns were taken from the BATSE Catalog. The lower limits were calculated for different time windows. The fourth column refers to the lower limit in T90 as defined by BATSE. The last seven columns refer to time windows following T90. They are also plotted in figures 2.3-2.8. The lower limits for a burst were not reported when all were zeros.

date	BATSE fluence	T90 (s)	LOWER LIMITS FOR EGRET ENERGY FLUENCES (erg/cm^2)							
			T90	10s	20s	50s	100s	200s	500s	1000s
910503	2.92E-04	50.82	8.49E-07	0.00E+00	0.00E+00	0.00E+00	0.00E+00	0.00E+00	0.00E+00	0.00E+00
930131	6.66E-05	19.20	1.16E-05	2.72E-07	2.11E-07	0.00E+00	2.79E-06	3.80E-06	2.60E-06	1.95E-06
911118	5.90E-05	19.20	0.00E+00	0.00E+00	0.00E+00	0.00E+00	0.00E+00	9.53E-06	8.26E-06	1.11E-05
950522	4.43E-05	59.07	0.00E+00	0.00E+00	0.00E+00	0.00E+00	4.73E-07	0.00E+00	0.00E+00	0.00E+00
930309	2.84E-05	90.11	0.00E+00	0.00E+00	0.00E+00	0.00E+00	0.00E+00	1.44E-06	0.00E+00	0.00E+00
931222	2.38E-05	57.66	0.00E+00	0.00E+00	0.00E+00	0.00E+00	0.00E+00	0.00E+00	2.99E-07	0.00E+00
930612	2.22E-05	41.98	0.00E+00	0.00E+00	0.00E+00	1.40E-05	1.30E-05	1.28E-05	3.21E-05	6.42E-05
940128	2.20E-05	45.25	0.00E+00	0.00E+00	0.00E+00	0.00E+00	0.00E+00	7.37E-07	0.00E+00	0.00E+00
950111	1.08E-05	102.91	0.00E+00	0.00E+00	0.00E+00	0.00E+00	0.00E+00	1.03E-06	0.00E+00	0.00E+00
910609	6.28E-06	0.46	0.00E+00	1.27E-07	0.00E+00	0.00E+00	0.00E+00	0.00E+00	0.00E+00	0.00E+00
940219	2.99E-06	0.68	0.00E+00	0.00E+00	1.24E-05	1.18E-05	7.93E-06	0.00E+00	0.00E+00	0.00E+00
920714	1.97E-06	23.74	0.00E+00	0.00E+00	1.37E-07	0.00E+00	0.00E+00	0.00E+00	0.00E+00	0.00E+00
941012	1.64E-06	20.93	1.51E-06	0.00E+00	0.00E+00	0.00E+00	0.00E+00	0.00E+00	0.00E+00	0.00E+00
940602	1.17E-06	9.92	0.00E+00	0.00E+00	0.00E+00	0.00E+00	0.00E+00	9.91E-07	0.00E+00	0.00E+00
940217	6.62E-04	150.14	1.59E-07	0.00E+00	0.00E+00	0.00E+00	0.00E+00	0.00E+00	4.16E-07	5.75E-07
910601	1.50E-04	28.54	0.00E+00	2.01E-07	4.20E-07	4.50E-07	0.00E+00	5.73E-07	5.97E-07	1.19E-06
940301	1.12E-04	42.50	5.12E-07	0.00E+00	0.00E+00	0.00E+00	0.00E+00	0.00E+00	0.00E+00	0.00E+00
910627	2.12E-05	15.17	0.00E+00	0.00E+00	0.00E+00	0.00E+00	6.32E-07	9.18E-07	0.00E+00	0.00E+00
930704	1.41E-05	144.93	0.00E+00	0.00E+00	0.00E+00	0.00E+00	0.00E+00	1.94E-05	1.98E-05	3.36E-05
940728	1.08E-05	37.38	0.00E+00	0.00E+00	0.00E+00	0.00E+00	0.00E+00	0.00E+00	0.00E+00	1.22E-06
950421	8.67E-06	19.20	8.87E-08	1.89E-07	9.65E-07	9.09E-07	8.14E-07	1.68E-06	1.06E-06	8.41E-07

Table 2.2: *continued*

date	BATSE fluence	T90 (s)	LOWER LIMITS FOR EGRET ENERGY FLUENCES (erg/cm^2) T90	10s	20s	50s	100s	200s	500s	1000s
940722	5.92E-06	89.34	0.00E+00	1.42E-06	1.27E-06	1.95E-07	0.00E+00	0.00E+00	0.00E+00	0.00E+00
930106	1.54E-06	15.30	0.00E+00	0.00E+00	0.00E+00	0.00E+00	2.51E-07	0.00E+00	0.00E+00	0.00E+00
910718	1.01E-06	0.25	0.00E+00	0.00E+00	0.00E+00	0.00E+00	0.00E+00	1.34E-06	0.00E+00	0.00E+00

2.2.2 Calculation

Let's suppose there is a photon source emitting gamma-rays with a differential photon flux dN/dE. A detector with effective area $A(E)$ and efficiency $\epsilon(E,t)$ observed the source for T time units. If the differential photon flux is a power law distribution of index $-\alpha$ (this is $\frac{dN}{dE} = CE^{-\alpha}$) then, the observed energy fluence is given by:

$$Fluence = \int\int E\frac{dN}{dE}\,dE\,dt = CT\int E^{1-\alpha}\,dE \tag{2.1}$$

The detector exposure is given by:

$$[Xpo(cm^2 s)] = \frac{\int\int \frac{dN}{dE}A(E)\epsilon(E,t)\,dE\,dt}{\int \frac{dN}{dE}\,dE} = \frac{N_s}{C\int E^{-\alpha}\,dE} \tag{2.2}$$

where N_s is the total number of observed events from the source in the observational time T. Therefore, from equations 2.1 and 2.2, the energy fluence is given by:

$$\Longrightarrow Fluence = \frac{N_s T}{Xpo}\frac{\int E^{1-\alpha}\,dE}{\int E^{-\alpha}\,dE} \tag{2.3}$$

The integral limits are from 30 MeV to 30 GeV. Therefore, the calculation of the energy fluence requires knowing the detector exposure, the total number of observed photons from the source in the observational time T and the differential photon flux index. For this analysis, the EGRET exposure is obtained for every burst as explained in the previous section. The spectral index was set to -2.4. The chosen value does not dramatically affect the fluence calculation when it is less than -2.0, see figure 2.2, since the EGRET effective area is not strongly E dependt. It is possible to approximate the energy fluence for different differential photon flux index multiplying by the factor $\frac{\int E^{-\alpha}\,dE}{\int E^{1-\alpha}\,dE}\frac{\int E^{1-\beta}\,dE}{\int E^{-\beta}\,dE}$. When no significant excess signal is detected, the true value of N_s is clearly unknown. The best that can be done is to find and acceptable interval for its mean $\overline{n}_s$ depending on the observed number of photons (source and background), n_o, and the expected number of photons from the background, b. The statistical method to determine this interval is carefully explained in the reference [FE98].

For each burst, n_o is the total number of photons detected in the time period T within the angular window centered at the burst direction. The duration of a burst is defined as the time interval within which 90% of the burst fluence is detected and it is called T90. The width of the angular window is determined from the BATSE burst location error added in quadrature with the E dependent EGRET point spread function. b was obtained by obtaining the total number of photons detected in the time period D within the same angular window used for n_o. D was typically set to two weeks washing out any increment in the background due to the burst emission. Then $b(T) = b(D)Xpo(T)/Xpo(D)$.

2.3 Results

Following the statistical approach described in [FE98], the 90% confidence level upper and lower limits for the energy fluence of the bursts in Table 2.1were calculated. When

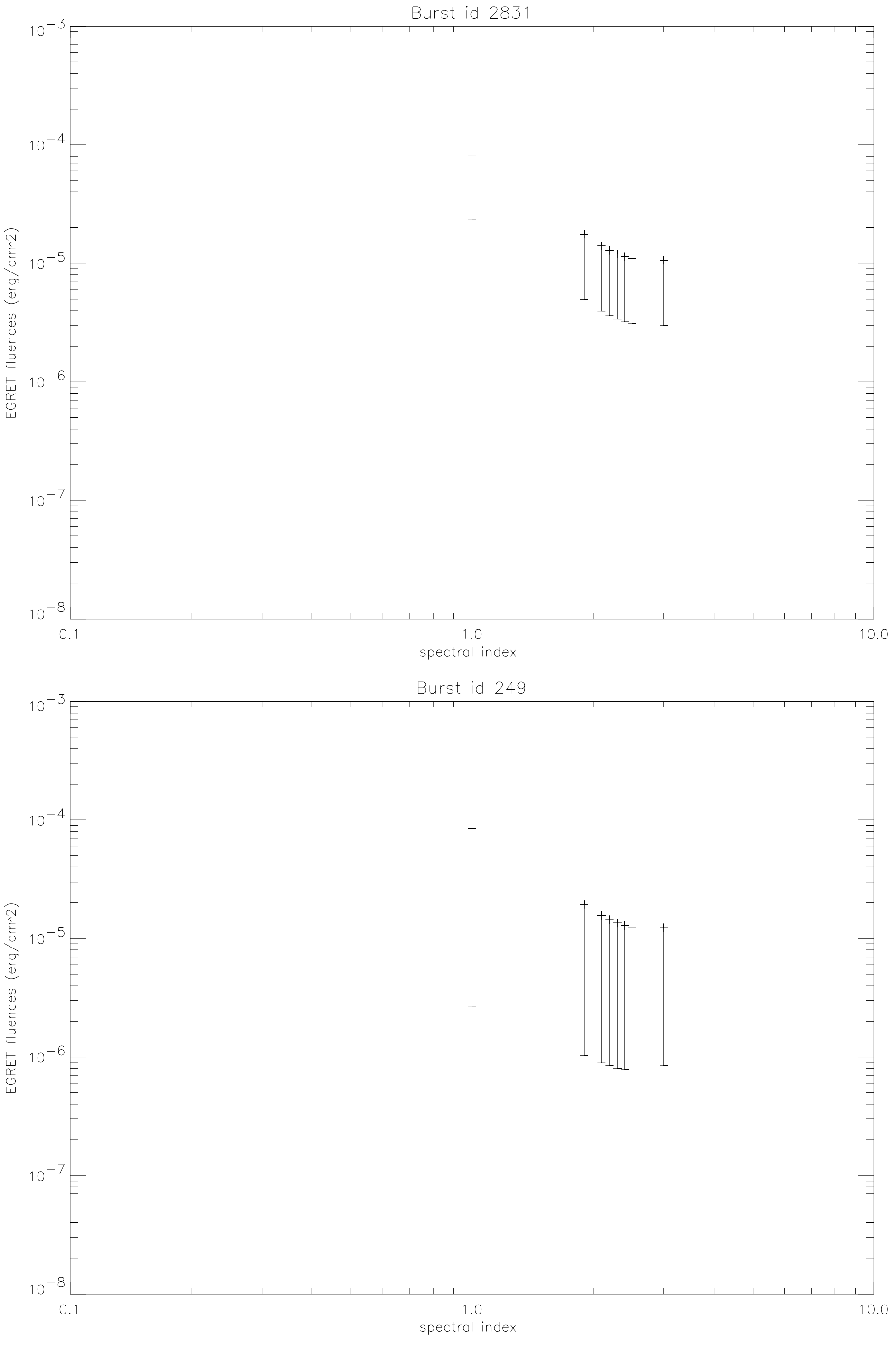

Figure 2.2: Limits to the EGRET energy fluences as function of the assumed spectral index. The limits are shown for GRB940217 (upper panel) and GRB910601 (lower panel).The energy fluences were calculated for the energy range of 30MeV-30GeV, 90% confidence level and the corresponding T90. The arrow head and tail correspond to the upper and lower limit of EGRET fluences, respectively. The upper limits change less than a factor of 2 for spectral indices less than -2.0. Similar results are obtained for other burst.

the lower limit was zero, only the upper limit was plotted as a small arrow head. Otherwise an arrow was plotted with the lower and upper limits as the arrow edges. It is important to point out that only lower limits are completely determined since a rapid variability of the high-energy emission on time scales comparable with the EGRET dead time yields higher upper limits, this is only true when non zero events were detected. In the case of T90 it is possible to correct the upper limits of the energy fluences by assuming the variability is equal to that observed in the sub-MeV emission. For durations longer than T90, this is not possible.

Figure 2.3 shows the energy fluence's limits for T90 seconds after the BATSE trigger time. The four arrows in the right side of the plot correspond to the four prior detections of the high-energy emission in T90. Slightl differences are observed between the limits reported here and in [DI01b]. These discrepancies are due to events found in EGRET data by a search posterior to the burst observations that have not been incorporated in the EGRET database but reported in the literature. Two extra arrows correspond two low significant detections (less than 3σ), GRB950421 and GRB941012.

Figure 2.4 shows the upper and lower limits of the energy fluences for 200s after the burst trigger. As calculated, the duration of the high-energy emission could be misinterpreted when an arrow in the plot claims detection. For instance, GRB910305 had 8 photons in T90 and 9 photons 200s after the BATSE trigger. This means that only one photon was observed in the 150s after T90 ($\sim$50s). Despite the arrow for GRB910305 in the calculation for T=200s, there is not significant 200s duration high-energy emission since the expected background is above 1 photon. GRB940301 is a similar case. Therefore, a different approach to constrain either a long-lived or a late high-energy emission is taken in this analysis. This approach is based on one fact and one assumption. First, if most of the high-energy emission has been observed in T90 then adding it to the calculation of energy fluences at longer times may yield fake significant detections. Second, if the high-energy emission after T90 does not present a rapid variability after T90, then a long-dim or a short-bright high-energy emission can be constrained by taking long and short observational times starting right after T90, respectively. In this calculation the observational times were taken as 10, 20, 50, 100, 200, 500 and 1000s. Figures 2.5- 2.8 show the energy fluence limits for each burst in Table 2.1.

Figures 2.5-2.8 show the energy fluence limits for all bursts, but only when the detection is above 3σ the limits are given by a blue arrow and the number of observed photons, the expected background and the probability of a excess due to chance is listed in the plot.

The high-energy emission in T90 was most likely detected by EGRET spark chamber for BATSE brightest bursts as shown in Figure 2.3. The high-energy emission in other weaker burst during T90 may be present but it was not observed by EGRET because of its low sensitivity doesn't seem significant Two moderate detections slightly above 3σ were observed for GRB950421 and GRB940219 in the 20s following T90, see bottom panel in 2.5. However, a total of 95×7 upper limits were calculated in this search,

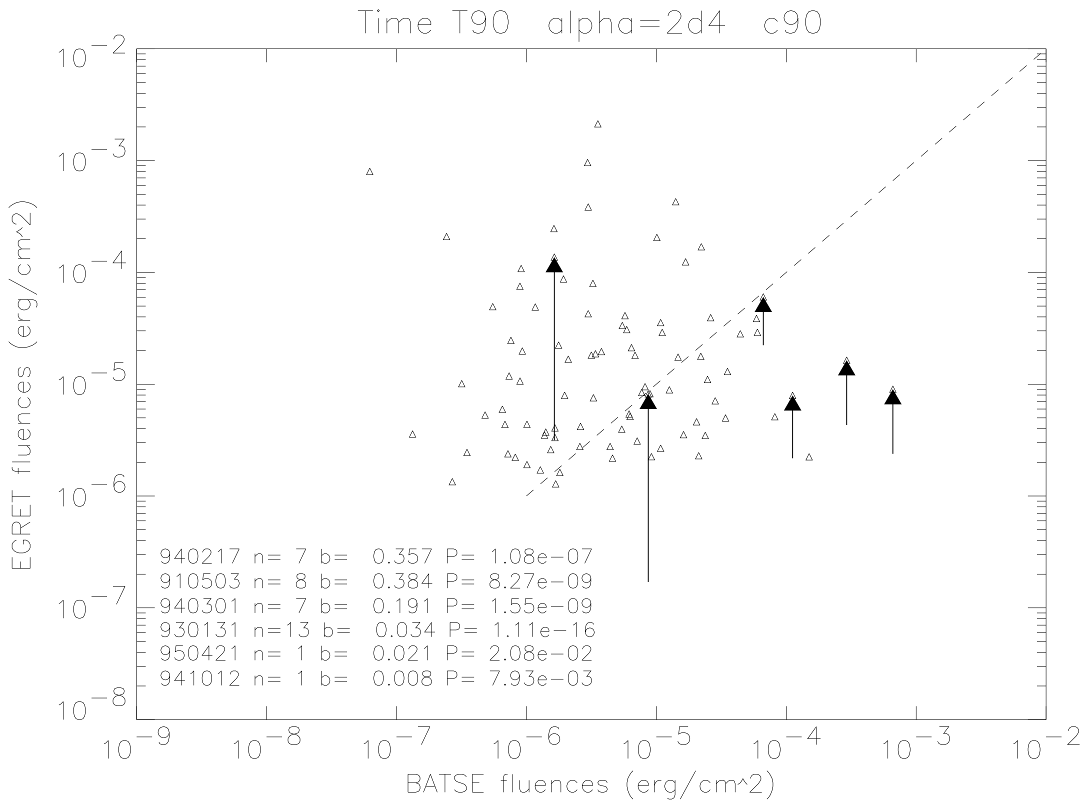

Figure 2.3: Limits to EGRET energy fluences in T90 for bursts given in Table 2.1. They are calculated in the energy range of 30MeV-30GeV, for 90% confidence level, spectral index equal to -2.4 and the corresponding T90 for each burst. They are plotted as function of the BATSE fluence for each burst. When the lower limit was equal to zero, only a triangle has plotted for the upper limit. The arrow heads and tails correspond to the upper and lower limits of EGRET fluences, respectively. When an arrow was plotted for a burst, the number of observed events n, the expected value b and the probability P of observing those events in T90 as fluctuation of the background are given in the plot, starting with bursts with higher to lower BATSE fluences. The dashed line corresponds to equal fluences in BATSE and EGRET energy sensitivity. The arrows with highest BATSE fluences correspond to the previous EGRET observations. The remaining two arrows are detections with significance less than 3σ.

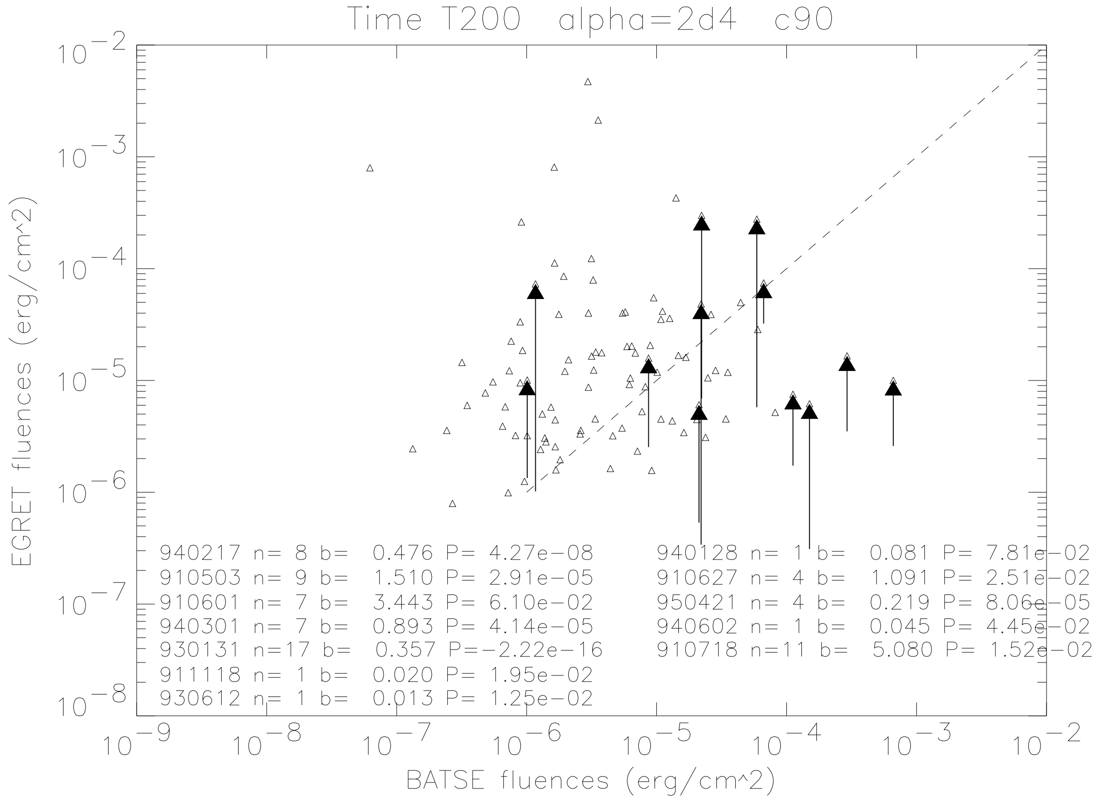

Figure 2.4: Same as Fig. 2.3, but for a 200s time interval starting at the BATSE trigger. GRB910305 showed 8 and 9 photons in T90($\sim$50s) and 200s after the BATSE trigger, respectively. Despite the arrow for GRB910305, there is not significant 200s-duration high-energy emission since the expected background is above 1 photon and only one photon was observed in the 150s following T90. GRB940301 is a similar case.

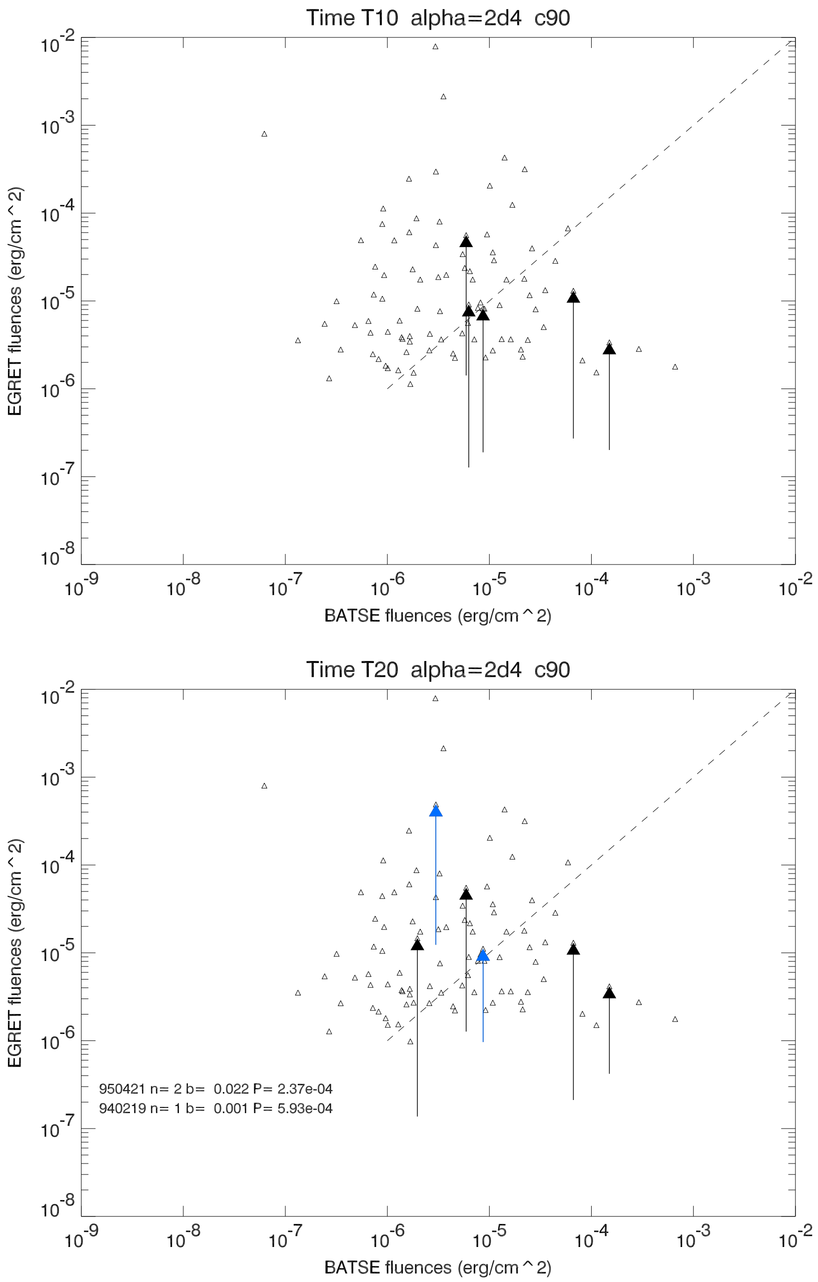

Figure 2.5: Limits to EGRET energy fluences for bursts given in Table 2.1. They are calculated in the energy range of 30MeV-30GeV, for 90% confidence level, spectral index equal to -2.4 and time intervals of 10s (upper panel) and 20s (lower panel) both starting at T90 seconds after the BATSE trigger. They are plotted as function of the BATSE fluence for each burst. When the lower limit was equal to zero, only a triangle has plotted for the upper limit. The arrow heads and tails correspond to the upper and lower limits of EGRET fluences, respectively. When an arrow was plotted for a burst, the probability P of observing n events as fluctuation of the expected background b was calculated. Blue arrows correspond to detections at least 3σ significant; n, b and P were given in the plot for these cases starting with bursts with higher to lower BATSE fluences. The dashed line corresponds to equal fluences in BATSE and EGRET energy sensitivity.

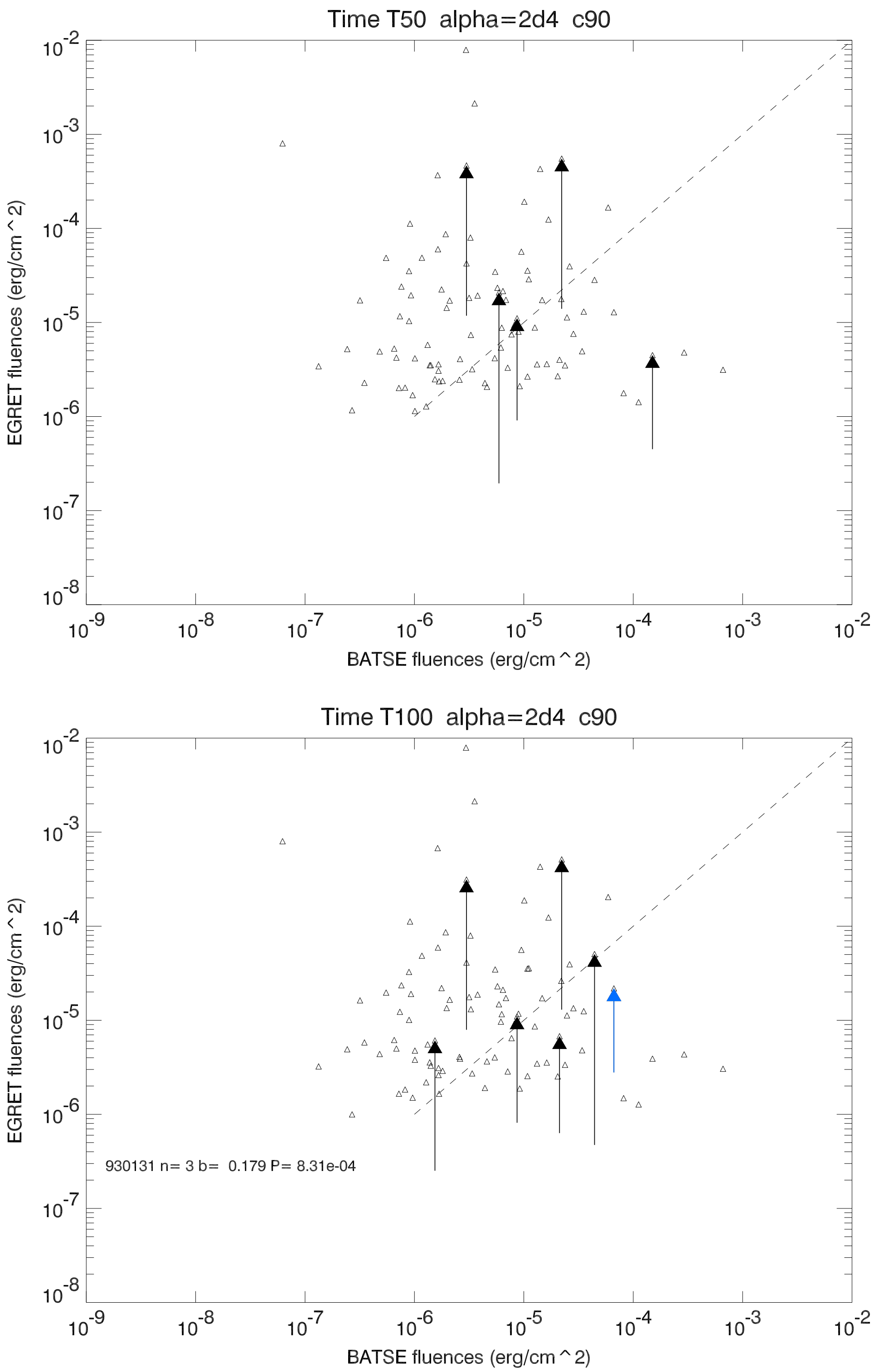

Figure 2.6: Same as Fig. 2.5 but for time intervals of 50 (upper panel) and 100 (lower panel) seconds, both starting at T90 seconds after the BATSE trigger.

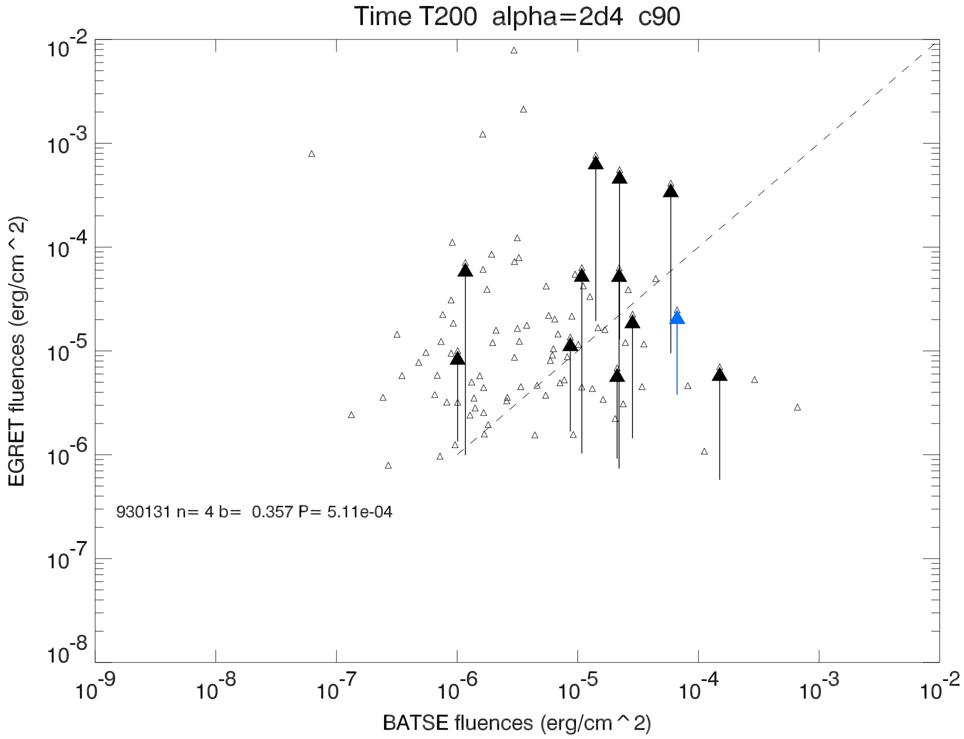

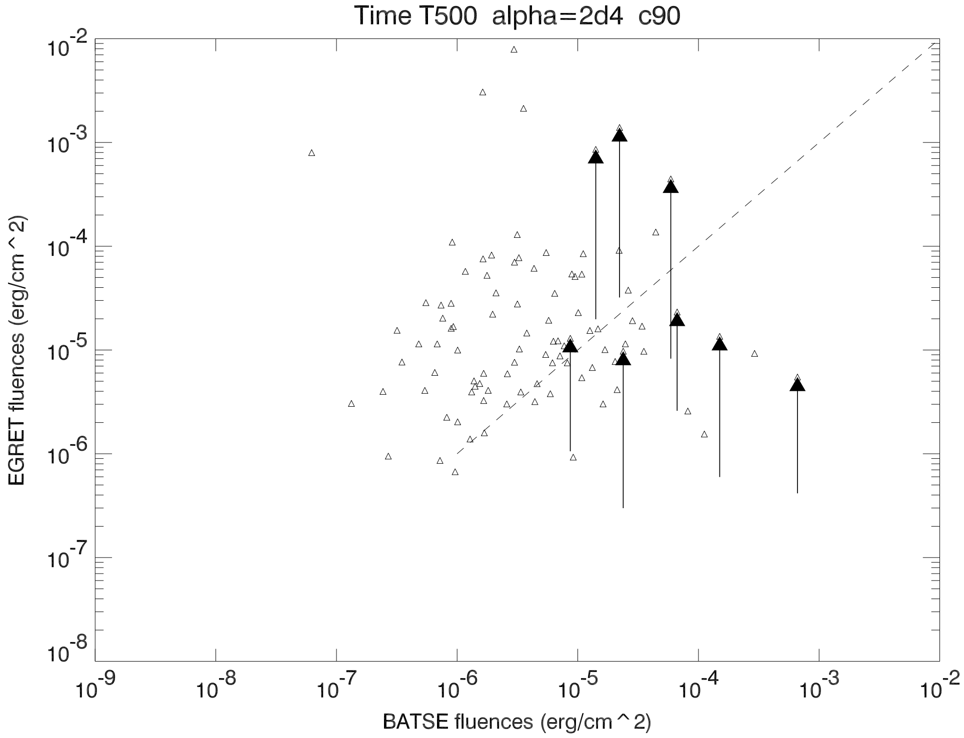

Figure 2.7: Same as Fig. 2.5 but for time intervals of 200 (upper panel) and 500 (lower panel) seconds, both starting at T90 seconds after the BATSE trigger.

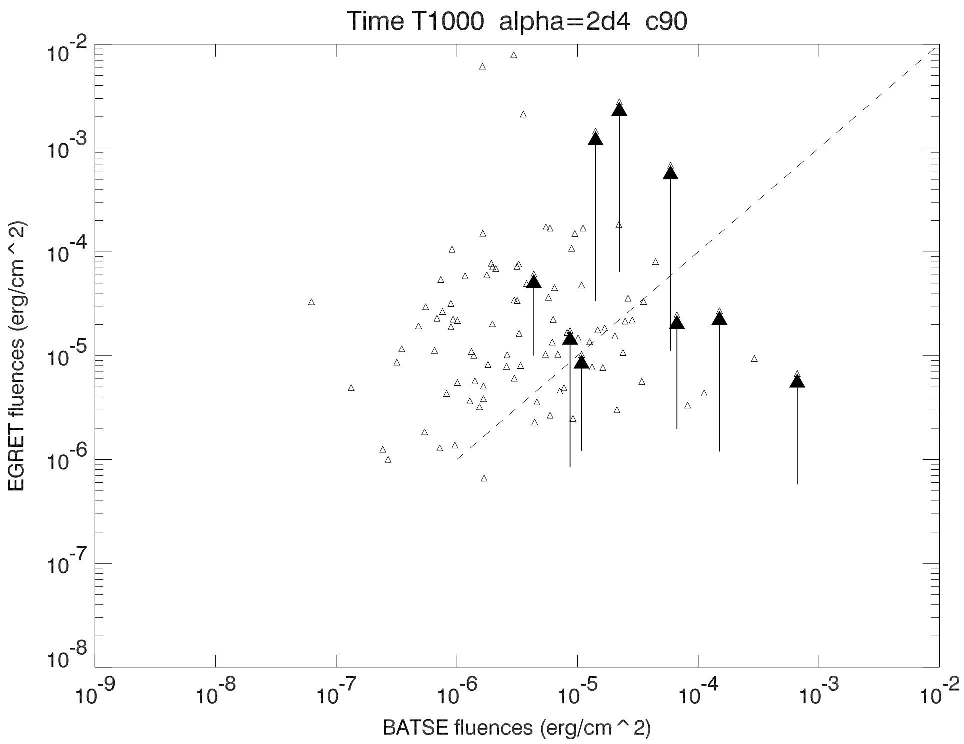

Figure 2.8: Same as Fig. 2.5 but for time interval of 1000 seconds, starting at T90 seconds after the BATSE trigger.

thus these are not significant to proof delayed emission in these bursts. For longer observational times following T90, there was not a new burst with high-energy significant detection. GRB930131 (T90 is $\sim$20s) was well known to have a high-energy emission up to 200s after the trigger time [DI95]. Figures 2.6 and 2.7 show that most of this emission came between 50s and 200s after the sub-MeV emission was over. Note that GRB941017 shows a marginal detection of the high-energy emission for 500s and 1000s after the sub-MeV emission is over. This does not mean that the high-energy emission did not extend to longer times but that the brightness of the high-energy emission is much dimmer after T90 than within T90. Therefore it gave a marginal EGRET detection after T90. Clearly, the key point to identify the long-lived high-energy emission in GRB940217 was its detection in T90 and the high energy of the photons coming after T90.

2.4 Conclusions

Limits to the energy fluence were calculated for BATSE bursts in EGRET's field of view. A new approach for the calculation was proposed with the advantages of obtaining a better constrain for the duration of the high-energy emission since misinterpretations may raise from the standard approach which included the prompt emission during T90. For instance, it was determined that most of the high-energy emission of GRB930131 was within T90 and between 50s and 200s after the sub-MeV emission was over.

The existence of high-energy emission in other weaker BATSE bursts but not observed by EGRET has been speculated (for example in [DI01b]). It was showed that a weak high-energy emission like the marginal observation in GRB940217 after T90 did not result in a significant EGRET detection.

High-energy emission lasting a few tens of seconds after the sub-MeV emission finished was observed in two bursts with a significance slightly above 3σ, GRB950421 and GRB940219. No significant detection of long-lived high-energy emission in any other burst was observed.

Chapter 3

GRB's emission from 0.02-200 MeV

The goal of this chapter is to increase our knowledge of the GRB prompt emission. The ideal experiment, for this purpose, is one that covers several orders of magnitude in energy with a fine energy and time resolution. The closest experiment to the ideal that ever existed is the Compton Gamma Ray Observatory, CGRO that covered six orders of magnitude in energy (from 30keV to 30GeV) with its four separated detectors, OSSE, BATSE, COMPTEL and EGRET. Joining data from these detectors could give GRB spectra in a broad energy range if a bursts is detected simultaneously by more than one detector with sufficient energy resolution to get a spectrum and, with overlapping energy ranges.

BATSE detected almost three thousand bursts, the largest set of bursts available, because of its full sky coverage. For most of these bursts, there are spectra covering three orders of magnitude in energy with at least 16 energy bins for 2ms accumulation time. BATSE also sent a trigger to the other three detectors when a burst was observed, assuring data acquisition with a better time resolution by the other detectors. Therefore BATSE data are the basic set of bursts for this analysis.

EGRET with the spark chambers covered the highest energy range (up to 30GeV) within its 40 deg of field of view. However, EGRET's spark chamber data is not useful for this analysis because it observed [SC93] only four bursts with no more than 18 photons each making impossible to obtain a spectrum for each burst.

OSSE and COMPTEL were detectors with energy ranges of 0.05-10MeV and 0.8-30MeV, respectively. They observed tens of bursts whose time-averaged spectra were analyzed and reported in some references such as [SH92b] and [KI96]. There have been some efforts to joint BATSE spectra with OSSE and COMPTEL; in fact, data from the EGRET's calorimeter TASC have also been used for this purpose. For example, in reference [SC96], the time-averaged spectra for 2 bursts were analyzed from 0.03-200MeV (obtained by including TASC) and for 20 bursts from 0.04-1.5MeV. All analyses using time-averaged spectra combining data from BATSE and OSSE or/and COMPTEL agreed with a GRB MeV-emission consistent with being a smooth continuation of the observed keV-emission.

OSSE had two scintillation detectors optically coupled. The primary one is made of NaI(Tl) covering the energy range of 0.05-10MeV. The secondary one is made of CsI(Na) covering the energy range of 10-250MeV. The field of view of OSSE was $3.8^o \times 11.4^o$(FWHM) and its time resolution for a BATSE trigger was 4ms. Therefore, it may be possible to use the whole OSSE capabilities to perform a time resolved analysis up to 250MeV of the GRB spectra jointly with BATSE. However, due to OSSE limited field of view and effective area, few bursts were observed to higher energies.

There is an easier way to obtain spectra up to 200MeV with a small cost in time resolution and sensitivity but a considerable gain in field of view, this is using TASC data. TASC data has been used to analyzed E time-average spectra in T90 [CA98], time resolved spectra [SC92, WR02] and, joint spectra using other experiments such as CGRO [BR99a] and BATSE+GINGA [SC98]. All these analyses also agreed with a GRB MeV-emission consistent with being a smooth continuation of the observed keV-emission.

A simple conclusion from previous analyses could be that the GRB spectrum continues smoothly to the MeV-regime without an obvious cutoff or extra component. However, there are two arguments against this conclusion. First, analysis of time-averaged spectrum is dominated by the brightest period of the burst, so even if the spectrum is strongly different during a dim period it will be unnoticed. Second, analysis of time-resolved spectrum at MeV-energies without previous knowledge of the spectrum at keV-energies may yield in a poor description of the high-energy spectral index (β in case of using the Band function), especially when the peak energy is close to the overlapping energies. Therefore, an analysis of time-resolved spectra using data from BATSE and TASC detectors, to enlarge the energy range, will lead to more conclusive results than previous analyses. In the following sections I will describe the details of such analysis as well as the results obtained.

3.1 BATSE

BATSE calibrated data are available for each observed burst in the CGRO web page http://cossc.gsfc.nasa.gov/batse . The detailed description of the BATSE instrument, including electronics, trigger generation, calibration, detector response and data types, is given in several references such as [FI89, PE95, PR00]. Therefore, only a summary description, to understand the choice of data types and the analysis, is given in this section.

BATSE consisted of 8 separated identical detector modules located at the corners of CGRO spacecraft on the faces of a regular octahedron. Each module had two NaI(Tl) scintillation detectors coupled with photomultiplier tubes (PMTs): a Large Area Detector (LAD) optimized for sensitivity and directional response and a Spectroscopy Detector (SD) optimized for energy coverage and resolution. Each detector had different energy capabilities; LAD had a constant energy range of 0.02-1.9MeV while SD had an adjustable energy range between 0.01 and 100MeV depending on the PMT's gains. Even thought SD was sensitive over a broader energy range, LAD's has a collecting area 16 times bigger than SD. Therefore, data from LAD is the most suitable for the purposes of this analysis

Each detector module was independent. Data were processed and accumulated to construct various data types with different energy resolutions and accumulation times in the Central Electronics Unit. The different data types contain either spectrum from each of the four detectors with the highest count rate or spectrum summed over all the triggered detectors. Data from a single detector was preferred, when possible, because the difficulty of calculating the detector response of 2-4 combined LADs. All BATSE data types have accumulation times either of 2, 16, 64 or 128 ms while TASC data have a minimum accumulation time of 1s. Therefore, performing a joint BATSE-TASC analysis requires of combining several BATSE spectra to obtain spectra for 1s or longer accumulation times. In the worst case, the mismatch between BATSE and TASC spectra time intervals will be of 128ms, which is small enough to not affect our analysis.

For data from a single LAD, the High Resolution Burst (HERB) data type was used because it has the highest energy resolution data in 128 energy channels for the energy range of 0.03-2MeV. HERB accumulation time is 64ms with time coverage depending on the burst count rate, being shorter than the burst duration for very bright or long bursts. When HERB data type does not cover the whole burst duration, the Continuous (CONT) and the Medium Energy Resolution (MER) data types were used. CONT data type also contains data from a single LAD but in only 16 energy channels. Its accumulation time was set to 2.048s because it is used mainly for background estimations. Therefore, CONT data type was useful only for long burst when the accumulation time of the TASC spectra is above 32s (maximum TASC accumulation time). MER data type contains spectra summed over the triggered LADs in 16 energy channels. MER accumulation time is 16ms for the first 2048 spectra and 64ms for the following 2048 spectra having total time coverage of about 164s. Therefore MER data type was used when the burst was very bright and shorter than 32s.

An example of a BATSE spectrum in HERB data type is shown in figure 3.1. The symbols correspond to background subtracted data for the first 7s after the trigger on a burst lasting 50.82s. A smooth continuous behavior is observed except for the

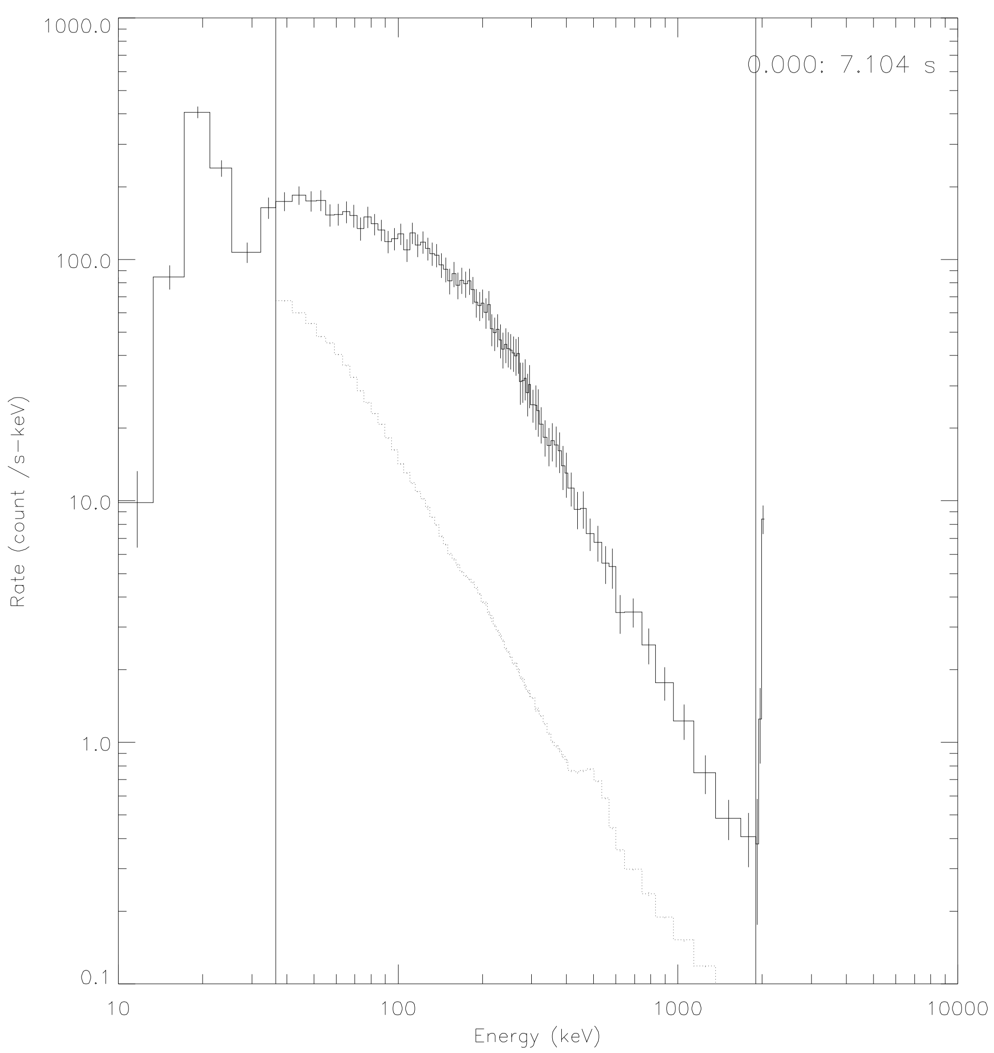

Figure 3.1: Typical BATSE spectrum in HERB format. BATSE time accumulated spectrum for the first 7s after the BATSE trigger of GRB910503 is shown. The crosses are for BATSE data. Depending on the data format, different channels were excluded from the analysis. In general, for HERB format the lowest seven channels were excluded because they were below the lower level discriminator energy threshold and, few of the highest channels were also excluded because they were saturated. The energy channels between the solid lines are the channels included in the analysis. The dotted line represents the background model (see text for details).

lowest and highest energy channels. This is because, the lowest energy channels were below the analog lower level discriminator and the highest energy channels suffered from saturation in the pulse amplifier. Therefore in both cases they are unusable and were thrown out for the analysis. The solid line corresponds to the calculated background for the same time period (details of the background calculation are given in section 3.5). Similar features are observed in MER and CONT data types.

3.2 EGRET - TASC

The Total Absorption Shower Calorimeter (TASC) was located at the base of the high-energy telescope and was not covered by the anticoincidence scintillation dome or any other active shield. It was a monolithic $76 \times 76 \times 20\text{cm}^3$ scintillation calorimeter formed by 36 NaI(Tl) blocks optically coupled. It was viewed by two groups of 8 interleaved Photomultiplier Tubes (PMT), each feeding a pair of Pulse Height Analyzers (PHA). One pair of PHA processed low-energy events (1-200MeV), while the other processed high-energy events (0.02-30GeV). Although TASC was part of the EGRET instrument in charge of measuring the energy of each useful event triggering the spark chambers (mainly done with the high-energy PHA), it was also an independent detector sensitive to gamma-rays and charged particles (using the low-energy PHA).

As an independent detector, TASC had its highest gamma-ray sensitivity in the same direction as the high-energy telescope, but it was sensitive to all particles from any direction. TASC was not able to differentiate between photons and charged particles; therefore physical information can be only obtained from accumulated low-energy events. This is why the accumulation time of 32.77 for low-energy spectrum was the normal and continuous mode of data acquisition, also called "solar" mode. For the particular case of studying GRBs using TASC data, it was necessary to have an external trigger from BATSE since TASC was not self-triggered. When the BATSE trigger was received a special acquisition mode, called "burst mode", was started and four spectra were accumulated for 1, 2, 4 and 16s sequential time intervals. In comparison with BATSE data, TASC solar and burst spectra are not available to the public. They are not cleaned or calibrated or corrected by the detector deadtime. Some codes to calculate the detector response and internal memos on the data format, deadtime and electronics have been written by EGRET collaborators but are not available to the public. In the following sections I will combine all this information to explain how the spectra and the detector response used in the analysis were obtained.

3.2.1 TASC data

As mentioned above, two low-energy PHAs received the analog sum of one of the PMT groups. The PHAs digitalized the energy signals over a range of 4096 channels that are later compressed and stored in only 256 channels. For the compressed spectrum, the first 64 channels have a compression factor of 1 with the compression factor doubling for every set of 32 channels after the initial 64. Therefore, the energy bin width corresponding to each channel must take into account the compression factor. The only difference between the solar and burst mode is the accumulation time, but both have the same format. According to preliminary EGRET memos (no final versions where available), data were not accumulated in the solar mode while the burst mode was active. However, solar spectra taken at the same time as burst spectra showed to be consistent with the background when no significant burst detection was observed, and having the same general behavior of the burst mode when a bright burst was observed. Therefore, no additional corrections to the count rates where made to the solar mode when used in the analysis.

The TASC spectra were accumulated, telemetered and saved in the compressed format. The first channel in the compressed format kept count of PHA livetime, the following 26 channels were mostly zeros and the observed counts were kept after channel 28.

The following errors mainly due to telemetry problems, were observed in the low-energy compressed spectra. Low or missing values were found in the livetime counter channel. When this error was observed, the livetime was derived from the total number of counts in the spectrum. Some spectra were shifted toward lower channels, then compression breaks were in a previous channel and the count number in the last channel was artificial. This error was a fixable by adding a zero in any of channels 2-10. When non-zero values were found in channels 2-27, they were ignored. Sets of zeros or dropouts were found in the spectrum due to lack of continuous telemetry coverage. This error was not fixable, so the spectrum was not used in the analysis. Many burst spectra were completely zeros, so they could not be used. Some spectra taken in the early part of the mission had wrong starting times because the GRO clock was wrong. Therefore corrections depending on the Truncated Julian Date and Seconds of the day were necessary. All spectra were carefully checked and corrected for this analysis.

3.2.2 Calibration

As explained in the section above, the data is stored in compressed spectra with 256 channels each. Every channel corresponds to a fixed voltage bin set by the PHA's digital conversion factor. The energy-voltage equivalence is determined by the PMT gains which drifted during the mission. The PMT high voltages were increased several times to increase the average gain. Therefore, in-flight measurements are used to determine the time-dependent calibration of TASC spectra.

The spacecraft structure contained two radioactive materials whose spectral lines are observed in TASC spectra: potassium-40 (1.46MeV) and thorium-232 (2.615MeV). Three more features are observed: the spectral line due to neutron capture of iron (7.6MeV), the spectral contribution of cosmic muons (around 100MeV) and an instrumental artifact (in the channel 500 of the uncompressed spectrum). The potassium line is used to determine the energy-voltage equivalence needed to calibrate the TASC spectra since it is the best defined.

A single 32.77s spectrum does not have enough statistics to find the potassium-40 line location. The drift of the PMT average gain varied between 0.14% and 0.024% per day during the mission. Therefore the energy-voltage equivalence is considered constant during 1hr around the burst trigger time and the spectra were added to find

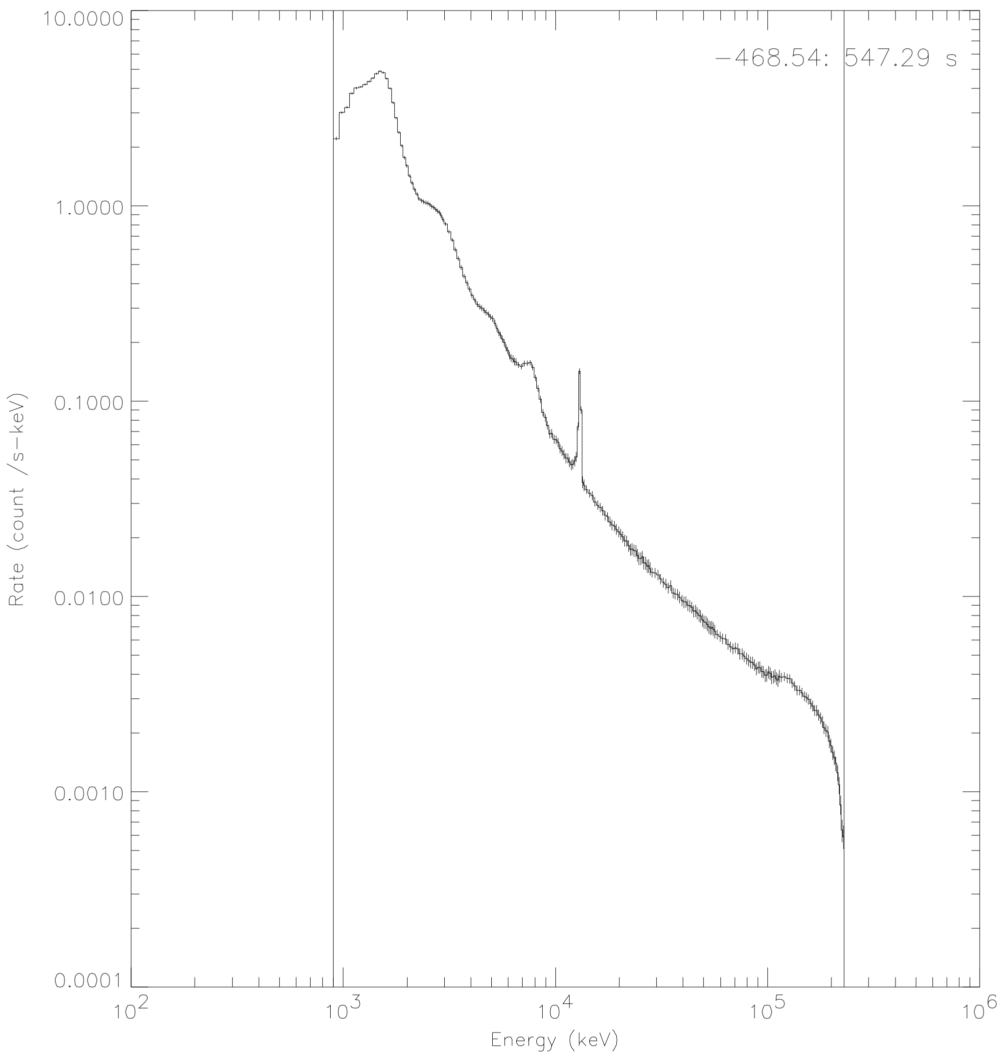

Figure 3.2: Typical TASC solar spectrum. TASC time accumulated solar spectra for ∼1000s is shown. Spectral lines are observed at 1.46MeV, 2.61MeV, 7.64MeV, ∼10MeV and beyond 100MeV corresponding to ^{40}K, ^{232}Th, neutron capture of Fe, an instrumental artifact and cosmic muons respectively. The potassium line is used to calibrate TASC data.

the potassium-40 line. Figure 3.2 shows an example of solar time-averaged spectrum over ∼1000s after being calibrated and corrected by the detector deadtime. The spectral features are clearly observed. The energy-voltage equivalence is determined using only solar spectra but is used to calibrate solar and burst spectra.

The energy-voltage equivalence (EV) is calculated as follows:

$$EV = \frac{1.46\mathrm{MeV}}{\mathrm{K40chan} - \mathrm{ZEROchan}}$$

where K40chan is the channel where the potasium-40 line was found and, ZEROchan is the channel that corresponds to 0MeV (assumed to be 12).

3.2.3 Deadtime

The compressed spectra contain the number of events detected in every energy interval corresponding to each channel. Solar and burst spectra are used together in this analysis. Therefore the spectra were converted to counts per unit of time per unit of energy or count rates that were corrected by the detector deadtime, mainly given by the electronics.

There are two different ways of obtaining the detector deadtime. One is using the counts collected in the first channel of the compressed spectra. An independent circuit to the PHAs polled the PHA every 512μs. If the PHA was live, one count was added to channel one (taking 1μs of storage time or polling deadtime) and the detector was assumed to be live for $512 - 1\mu$s. Therefore the deadtime is given by:

$$\mathrm{DeadTime}_1 = \mathrm{AccuT} - 511 \times 10^{-6}\mathrm{s} \times \mathrm{N}_1$$

where N_1 is the number of counts in channel 1 of the compressed spectra and AccuT is the accumulation time of the spectrum. Because of telemetry problems, the information of the channel 1 was lost in some spectra and a zero value was found instead. This problem was more frequent in burst spectra. Fortunately, it was possible to derived the deadtime using the total number of counts in the spectra.

The derived deadtime was calculated considering the PHA's conversion, compression and storage times as well as the polling time explained above and the hazard time. The conversion time depended linearly on the energy, ranging from 0 to 256μs. The maximum conversion time was given by the PHA's internal 16Mhz clock. If a pulse arriving from the PMTs needed more than 256μs to convert, the conversion was stopped and no result was recorded. The compression and storage times are unknown, but they were deduced by matching $\mathrm{DeadTime}_1$ with the derived deadtime as possible. A total value of 165μs was set for all spectra since compression and storage times are not expected to change with time. Finally, each event had a 20μs extra deadtime or hazard time that updated if additional events occurred while processing. Therefore the derived deadtime considering all contributions except the polling time is given by:

$$\mathrm{DeadTime}_{\mathrm{CCSP}} = 10^{-6}\mathrm{s}\ (256\Sigma_i(\mathrm{C}^i_{\mathrm{last}}\mathrm{N}_i) + 165\Sigma_{\mathrm{i}}\mathrm{N}_i + \mathrm{N}_1)$$

where $\mathrm{C}^i_{\mathrm{last}}$ is the number of the last channel of the uncompressed spectra included in

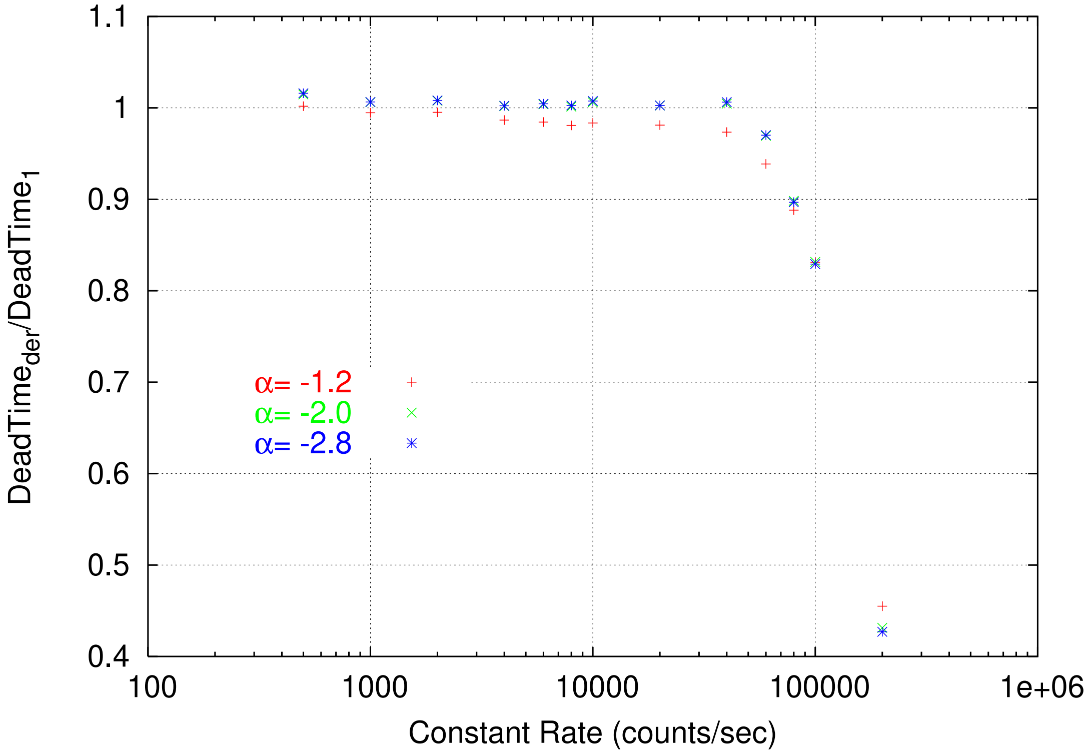

Figure 3.3: Two different ways to estimate TASC dead time are compared for different count rates and spectral indexes. DeadTime$_{\text{der}}$ refers to the derived dead time and DeadTime$_1$ refers to the obtained using the number of counts in channel one (see text). The discrepancy is at most 5% for count rates below 60,000 counts per second independently of the spectral index.

the compressed i-channel and N_i is the number of counts in the compressed i-channel. Then the derived deadtime considering the hazard time is deduce from:

$$\text{DeadTime}_{\text{CCSP}} = \text{DeadTime}_{\text{der}} \exp(-\text{DeadTime}_{\text{der}} \times 20 \times 10^{-6}\text{s})$$

All spectra, solar and burst, are corrected using the derived deadtime because as mentioned above, the information of channel 1 was not always available. A Monte Carlo simulation of the detector electronics was performed to study the conditions under both derivations agree, quantify the discrepancy and study their limitations depending on

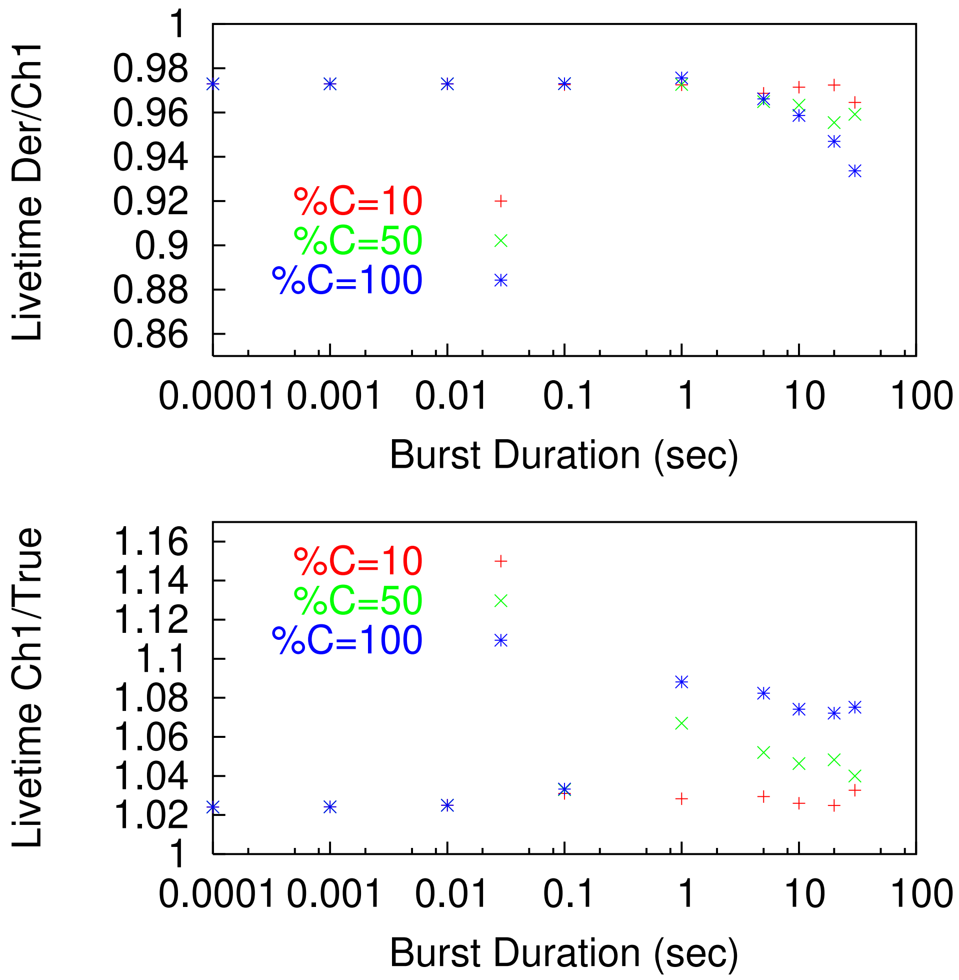

Figure 3.4: Two different ways to estimate TASC live time are compared for different count rates and burst durations in upper panel. The derive TASC live time is compared with the true TASC live time from a Monte Carlo simulation in lower panel. "LiveTime Der", "LiveTime Ch1" and "LiveTime True" refer to derived live time, live time from using number of counts in channel 1 and the true live time from a Monte Carlo simulation, respectively (see text). %C=10,50 and 100 correspond to burst count rates of 1,000, 5,000 and 10,000 counts per second. The disagreement between the true, derived and calculated with channel 1 live times is worse for the brightest burst but it is in less than a 7% for all burst for which TASC is most sensitive (longer than a few seconds). The derived live time showed a better agreement with the true live time than the calculated with channel 1.

spectral index, count rates and burst duration.

In Figure 3.3 the ratio of the derived deadtime over the one calculated using channel one is shown as function of background count rate for three different spectral indices. The background is considered constant in time. As observed in the figure, the discrepancy between both calculations does not strongly depend on the spectral index, in fact in most of the cases it is below 3%. The highest discrepancy rises when the count rate increases. For count rates above 60,000 counts per second, the discrepancy starts to be considerable, it is above 5%. However, even for the brightest bursts, the observed count rates are below 20,000 counts per second.

In Figure 3.4, two livetime ratios are shown as a function of burst duration for three different values of the burst count rate. One is the ratio of derived livetime over the one calculated with channel 1 and the other is the livetime calculated with channel 1 over the true livetime. The background rate is fixed to 10,000 counts per second and the burst count rate is set to 1,000, 5,000 and 10,000 and, the background spectral index is taken as -1.8. As observed in 3.3 the burst spectral index has a small effect on the deadtime. The disagreement between the true, derived and calculated with channel 1 deadtimes is worse for the brightest burst but it is in less than a 7% for all burst for which TASC is most sensitive (longer than a few seconds). The derived deadtime showed a better agreement with the true deadtime. Figure 3.2 shows calibrated TASC spectrum after corrected by the detector deadtime.

3.2.4 Response Matrices

Deducing the photon flux reaching the detector from the observed spectrum requires knowing the detector response to radiation of different energies and incoming directions under the experimental conditions. Since TASC was one of the four detectors in CGRO, its sensitivity was highly dependent on materials and components of the other experiments and spacecraft. Then, a detailed GRO mass model was used with Monte Carlo code EGS4 [NE85] to calculate the detector response for a finite number of gamma-ray energies and directions. A validation of the calculated values were made by radioactive source surveys [TH93] using cobalt-60, prior to launch.

Figure 3.5 shows TASC response as a function of the zenith and azimuth angles. TASC response is given as TASC area multiplied by its efficiency. The zenith and azimuth are relative to the pointing-axis direction of CGRO. Zenith angle 0^o represents the pointing direction of EGRET and CGRO. Azimuth angle of 0^o points from TASC toward COMPTEL and OSSE and, azimuth angle of 180^o is the largely unobstructed direction away from the other instruments. The experimental data were normalized to predicted values given in the figure caption. Data and predicted values show discrepancies that could be attributed to the CGRO mass model. For example, at zenith angle of 120^o and azimuth angle of 168^o, the mass model may be underestimating the intervening material. Although the GRO mass model is imperfect, data and predicted TASC response have similar general trend and their discrepancies are small when compared with the evolution with the zenith/azimuth angle. It is also observed that the TASC

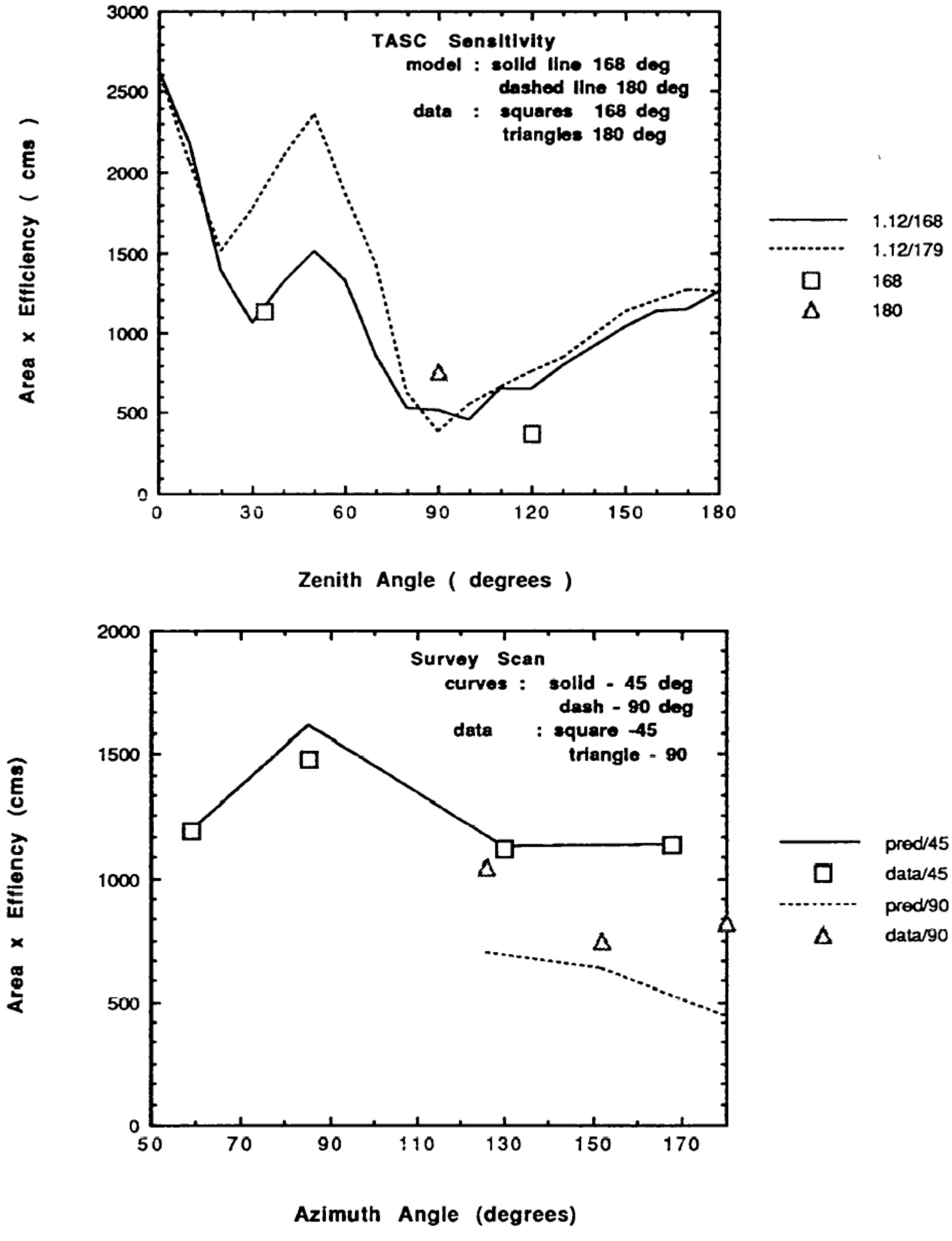

Figure 3.5: TASC sensitivity as function of the zenith and azimuth angles. TASC sensitivity is shown for the energies of cobalt-60 lines as a function of zenith (upper panel) angle for fixed azimuth angles of 168 (squares and solid line) and 180 (triangles and dotted line) degrees and, as a function of azimuth (lower panel) angle for fixed zenith angles of 45 (squares and solid line) and 90 (triangles and dotted line) degrees. Data and Monte Carlo predicted trends are consistent. The discrepancies are attributed to the CGRO mass model because of an underestimation of the intervening spacecraft material.

response dependency on the zenith angle is much stronger than its dependency on the azimuth angle.

In order to understand the general characteristics of TASC response, the simulation results are plotted as function of energy and zenith angle in figures 3.6 and 3.7. The electronics and the detector energy resolution are not included in the simulation. Six thousand gamma-rays were thrown for each of the following energies: 0.75, 0.80, 0.90, 1, 1.20, 1.50, 2, 4, 6, 8, 10, 20, 30, 40, 50, 60, 70, 80, 100, 120, 150 and 200 MeV for each burst direction. Figure 3.6 shows the number of detected photons with a given energy normalized by the total number of thrown photons with three different energies and two directions. As observed, most of the photon energies are reconstructed close to their original value. This is because pair-production is the predominant interaction and, the large dimensions of TASC allow the annihilation of the resulting positron inside the calorimeter. Also, as the thrown energy increases, the probability of stopping the resulting electron decreases, then the reconstructed photon energy slightly decreases broadening the pair-production peak. The continuous small contribution preceding the pair-production peak is due to Compton scattering. Although the peak at 0.511 MeV is below the TASC threshold energy (dotted line), it is showing that the surrounding materials are taken into account in the calculation of the TASC response.

Clearly, the incident direction of the gamma-ray does not change the general features of TASC response, as observed in figure 3.6. However, it affects the total TASC efficiency. Figure 3.7 shows the total number of detected photons normalized by the

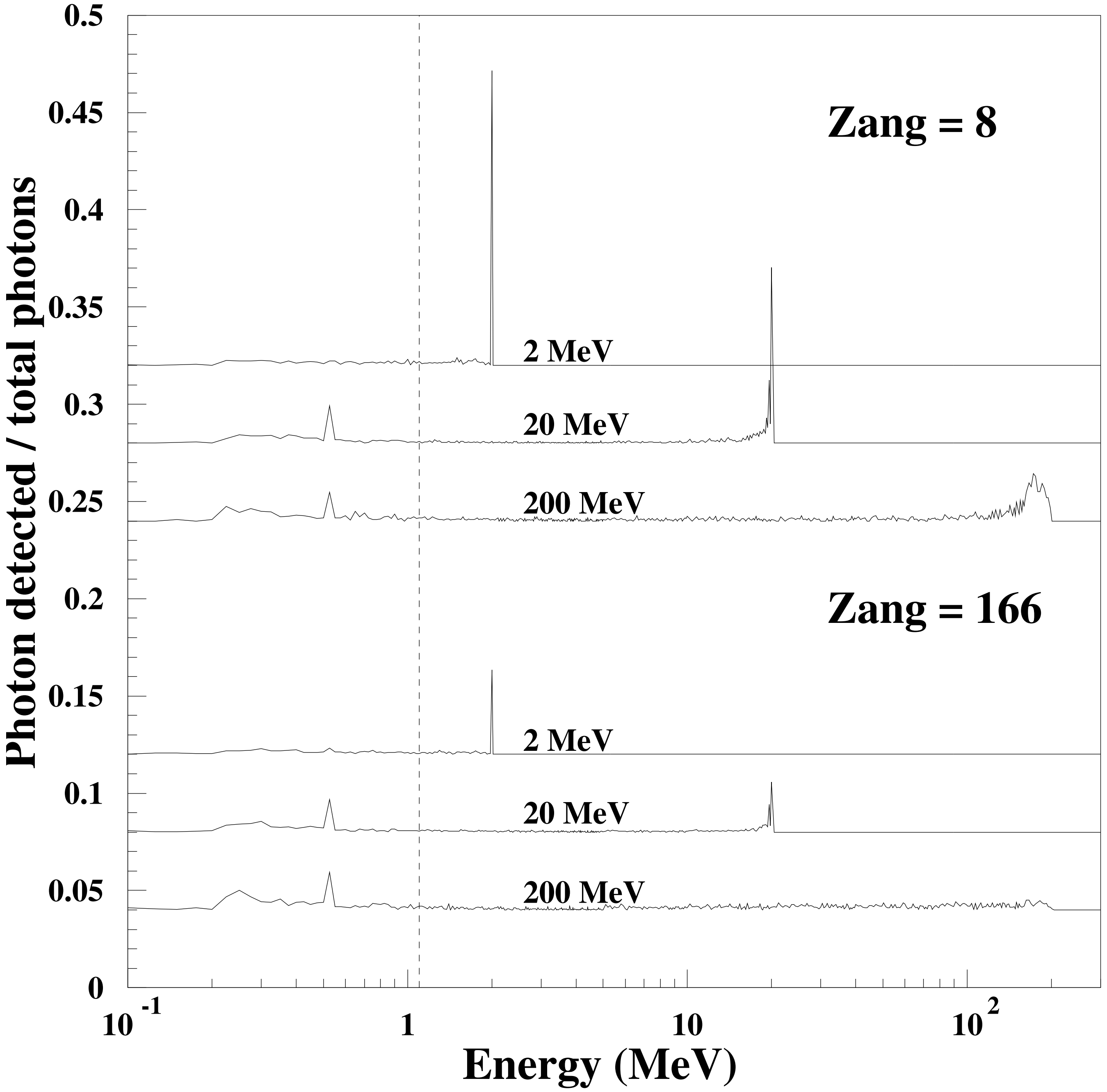

Figure 3.6: TASC response simulation for different incoming-photon energies and zenith angles. Most of the photon energies are reconstructed close to their original one. The highest energy peaks are due to pair-production of the incoming-photon. The peaks at 0.511 MeV show that the surrounding materials are taken into account.

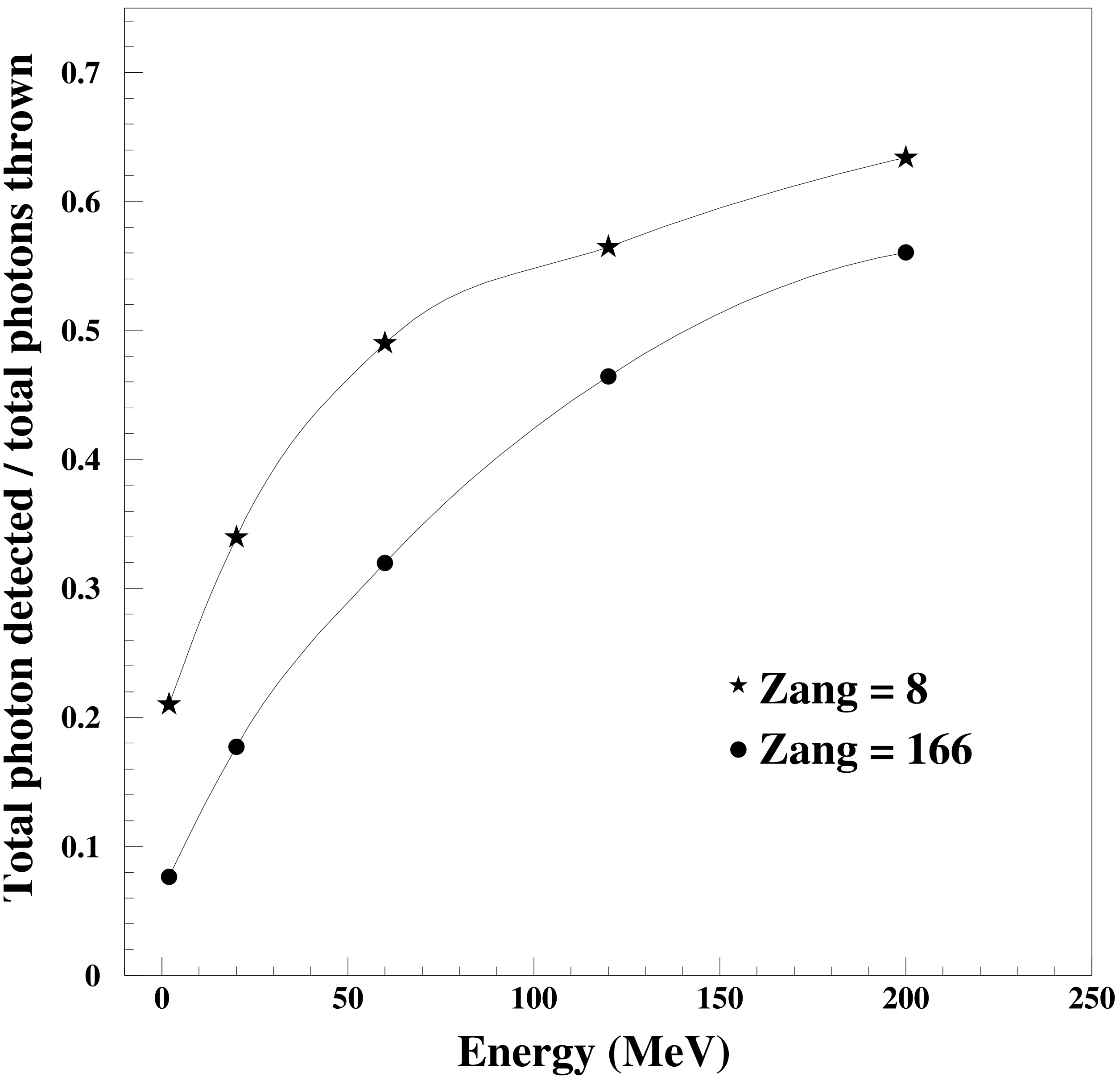

Figure 3.7: TASC efficiency for different incoming-photon energies and two fixed zenith angles. TASC efficiency increases with energy since pair-production is the main interaction.

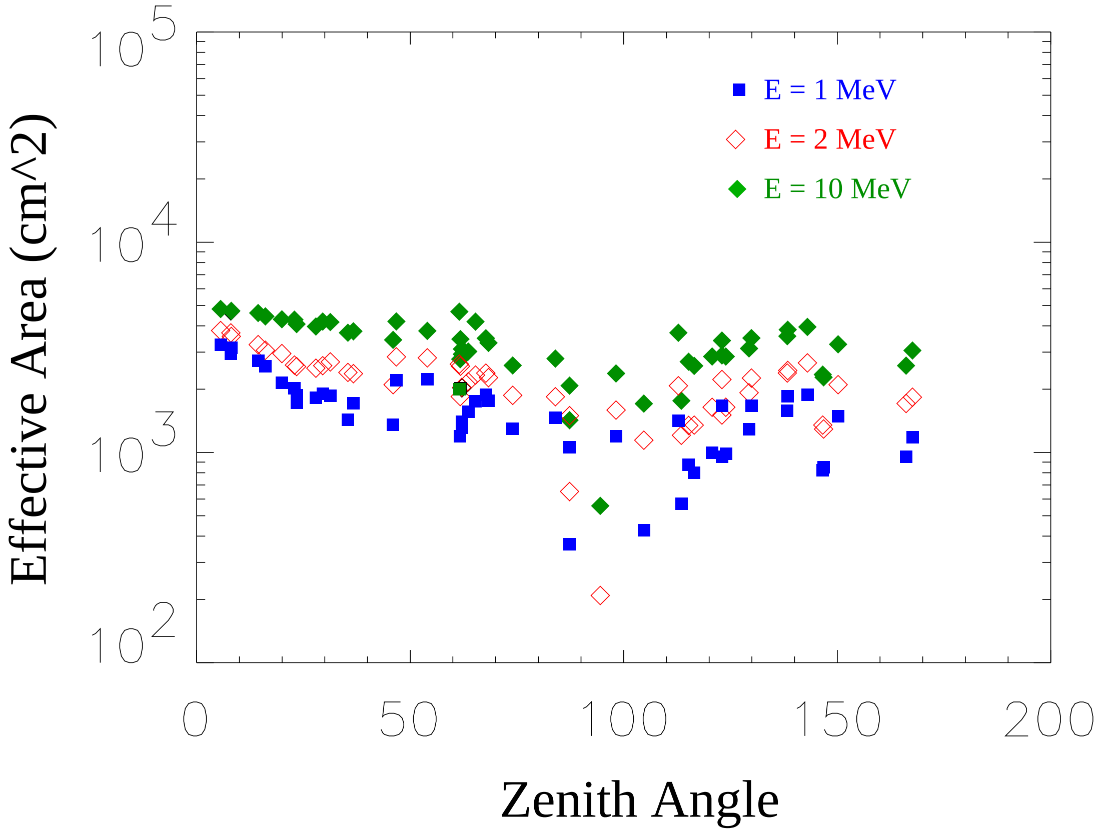

Figure 3.8: TASC effective area for different zenith angles and three fixed energies. TASC efficitive area reaches its lower value and is "almost symmetric" around 90^o as expected for a calorimeter with the TASC geometry.

total number of thrown photons as a function of the thrown photon energy for two different directions. TASC efficiency increases with energy reflecting the predominance of pair-production as the main interaction. The highest TASC efficiency for a zenith angle close to 0^o is affected by the intervening material since photons coming from the front find a mostly unobstructed path to the calorimeter and, in both cases the effect of TASC geometry is similar. Figure 3.8 shows same as in figure 3.7 multiplied by the irradiated area, as a function of the zenith angle for 3 different throw energies and fixed azimuth angle ($\sim 0^o$). As observed, TASC efficiency reaches its lower value and is "almost symmetric" around 90^o as expected for a calorimeter with the TASC geometry.

TASC response was calculated and stored as a matrix with each cell corresponding to a given throw energy and reconstructed interval of photon energies. Each energy interval corresponds to an energy bin of the measured spectrum. The values for each cell were interpolated from the Monte Carlo simulation. A value of 20% FWHM [TH93] was used as TASC energy resolution.

3.3 Spectral Fitting Code

For the analysis of BATSE data, a software has been written by the BATSE collaboration. One of these software packages is the RMFIT, an improved version of the Windows Gamma Spectral Analysis code, WINGSPAN [PR94]. It was written as object-oriented code within IDL, with the spectral fitting engine written as a FORTRAN dynamically-linked library. Although RMFIT is not available to the public and is not documented, it was used to analyze combined BATSE-TASC data because of the following features.

- Usage of data storage in Flexible Image Transport System files, FITS format.

- Display of high-energy astrophysical data as time sequences of spectra.

- Interactive selection of regions of interest for spectral fitting.

- Interactive selection of regions for background subtraction. Both numerical and visual cues aid in the evaluation of the goodness of the background model.

- A fast fitting engine that implements model, rather than data, variances to allow for more accurate fitting of data that have both high- and low-counts statistics in their energy spectra.

- User selection from a number of common additive and multiplicative spectral models, including user-defined functions.

- Several ways to analyze time-resolved spectral fit parameters.

- Cross-platform compatibility through IDL.

- Joint fitting of several sets of data from different detectors, instruments, and/or spacecraft. Any normalization mis-match between different sets of data can be resolved via a multiplicative factor as an extra model parameter.

RMFIT obtains the photon flux reaching BATSE and TASC by fitting a photon flux model to the observed BATSE and TASC spectra/count rates. The fitting is done by the standard forward-folding technique where the parameterized photon flux model is evaluated and multiplied by the detector response matrices to obtain the count rate model. Then the count rate model is compared to the count rate data. The parameters of the photon flux model are varied such that the deviation between model and data is minimized as determined by the χ^2 function. The minimization is done via the Levenberg-Marquardt algorithm [PR02]. The fitting is an iterative process until the optimal parameter values are obtained. The estimated parameter uncertainties are derived from the covariance matrix [PR02], which is based upon the derivatives of χ^2 with respect to the model parameters.

3.4 Selected GRBs

In the preceding sections, the convenience of a combined BATSE-TASC analysis was explained. Also, the choice of BATSE data format was justified and the process to obtain the TASC response and then the calibrated and deadtime corrected TASC spectra was described. A general description of the code used for the analysis was given too. Now, this section will talk about the gamma-ray bursts selected for the combined BATSE-TASC analysis.

The goal is to have BATSE triggers that had a significant TASC detection. One way to search is to look for a TASC detection in every BATSE trigger. If the burst spectrum is assumed to have only the Band contribution, then obtaining calibrated and corrected TASC data for each of the three thousand bursts in BATSE catalog could be a very long process with only a few useful bursts. A smartest way to search is by improving the probability of having burst emission at TASC energies requiring the following two conditions in BATSE triggers: having a photon flux above $10 \mathrm{ph/s{-}cm^2}$ and an observed

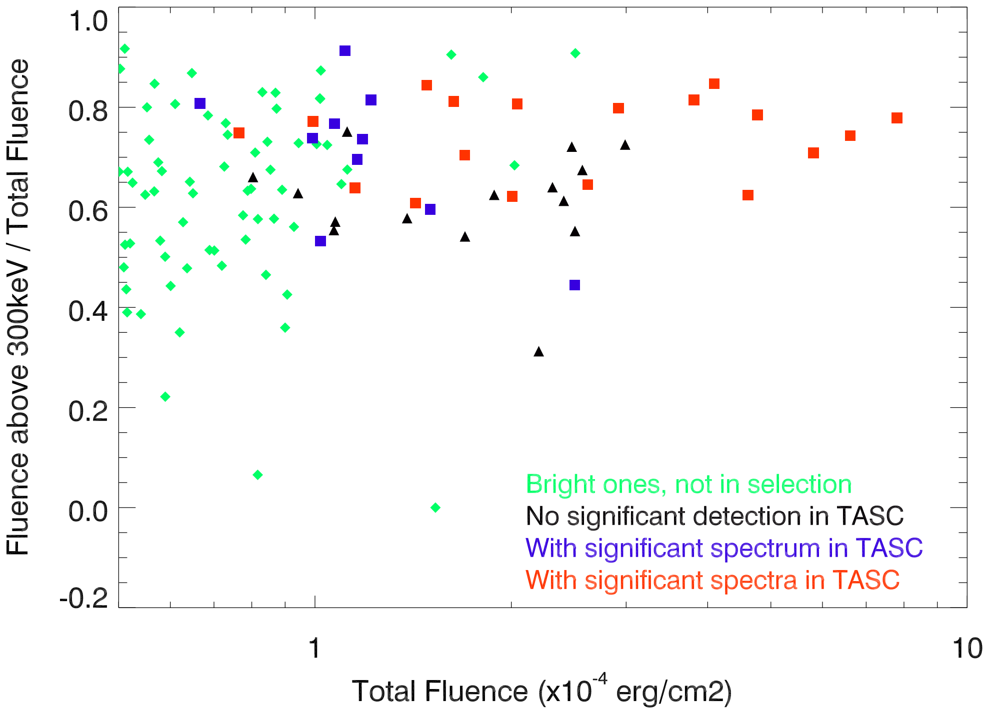

Figure 3.9: BATSE energy fluence above 300keV as function of the Total BATSE energy fluence for the brightest BATSE bursts. The BATSE energy fluence above 300keV is divided by the total BATSE energy fluence to emphasize its contribution to the Total fluence. Black triangles, blue squares and red squares correspond to bursts satisfying the selection criteria with none, one or more than one TASC spectrum with significant detection. Red squares correspond to the bursts included in the analysis of this chapter.

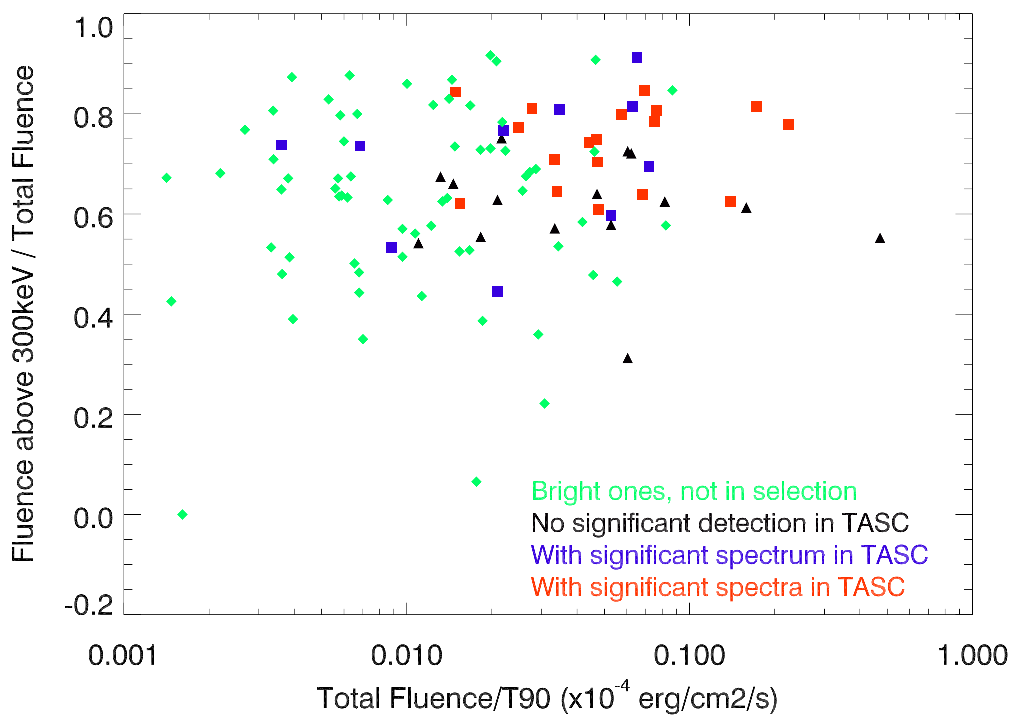

Figure 3.10: BATSE energy fluence above 300keV as function of the Total BATSE energy flux in T90 for the brightest BATSE bursts. The BATSE energy fluence above 300keV is divided by the total BATSE energy fluence to emphasize its contribution to the Total fluence. Black triangles, blue squares and red squares correspond to bursts satisfying the selection criteria with none, one or more than one TASC spectrum with significant detection. Red squares correspond to the bursts included in the analysis of this chapter.

fluence in the BATSE 4th channel (above 300keV) higher than 5×10^{-5}erg/cm^2. Forty three bursts satisfied these conditions. Table 3.1 indicates how many significant TASC spectra (more than 3σ) were detected for each of the forty three bursts as well as any problems in obtaining TASC data or the response matrix and the existing references for each burst.

Table 3.1: TASC spectral information for bursts included in the analysis. Third column indicates how many TASC spectra with significant detection were analyzed for each burst. Fourth column indicates the problems with TASC data when TASC spectra were not available. If none problem is reported, TASC spectra were available but did not have significant detection. Last column reports the existing references for each burst.

BATSE id	**GRB**	**# of TASC spectra**	**Problems**	**References**
3057	940703	2	—	—
2831	940217	3	—	[DI98, DI95, CA98, WI95] [TO97, HU94]
7301	990104	3	—	[WR02]
7343	990123	2	—	[KU99, ME99, DA99, LI99] [FR99, FE99, BL99, SA99] [BL99a, YO99, BR99, HO99] [BR99a, YO00, WI00, SO00] [MI00, HO00, BJ01, WA00] [SO02, FA02, BA99, SO03] [CA99]
3523	950425	2	—	[CA98]
2329	930506	3	—	[CA98]
7113	980923	2	—	[GI00, GI99, BJ01a]
143	910503	4	—	[DI98, DI95, CH99, CA98] [WI92, HA94, SC92, SC93]
7491	990323	NONE	No TASC data available	— —
7575	990518	NONE	—	—
6472	971110	NONE	—	—
3245	941017	7	—	[CA98]
5995	970202	2	—	—

Table 3.1: *continued*

BATSE id	**GRB**	**# of TASC spectra**	**Problems**	**References**
7906	991216	NONE	No TASC data	—
			around trig	—
2798	940206	NONE	No TASC data	—
			available	—
5614	960924	NONE	—	—
6168	970411	2	—	—
7549	990506	3	—	[BL03, BU03, TA00]
7170	981021	2	—	—
1663	920622	4	—	[CA98, GR95, SC95]
6587	980203	NONE	—	—
2856	940302	1	—	—
5477	960529	1	—	—
7695	990803	1	—	—
2156	930201	NONE	—	—
249	910601	1	—	—
3930	951203	1	—	—
1473	920311	2	—	—
7929	000101	NONE	—	—
2994	940526	1	—	—
1625	920525	1	—	—
1541	920406	NONE	—	—
3178	940921	2	—	[CA98]
6124	970315	2	—	—
1886	920902	1	—	—
4368	960114	NONE	—	—
3128	940817	NONE	—	—
3408	950208	NONE	No TASC data	—
			available	—
6985	980810	NONE	—	—
6100	970223	3	—	[CA98, PA97]
3227	941008	1	—	—
2151	930131	1	—	—
3492	950403	NONE	No TASC data	—
			around trig	—

Clearly, the selected bursts belong to the set of brightest BATSE bursts. Figure

3.9 shows the ratio of the fluence observed above 300keV over the total fluence versus the total fluence for all bursts with total fluence above 0.5×10^{-5}ergs/cm^2.Triangle and square symbols represent no TASC detection and detection for the selected bursts, respectively. As observed, the selected bursts have almost all the highest total fluences. Only four bursts with relative high total and 4th channel fluences were not selected. These four bursts have a low photon flux, but their emission is at the highest BATSE energies. They may be interesting candidates for a future analysis. Bursts with TASC significant detection tend to be the ones with the highest total fluence with a large contribution above 300keV, independent of the burst duration. However, they are not the brightest ones as observed in figure 3.10 where the ratio of the fluence observed above 300keV over the total fluence is plotted versus the ratio of the total fluence over the burst's duration given by T90.

As mention above, forty three bursts satisfied the selection conditions. There were no available TASC data for five of these bursts, either because no storage spectra were found in TASC database or because spectra around the trigger time were missing probably due to lack of telemetry coverage after the failure of the GRO's tape drives. Ten bursts did not have significant detection in TASC data. The analysis described in this chapter concentrates on the time resolved spectra. Therefore, only eighteen bursts of the twenty eight detected by TASC that had more than one significant spectrum are described. The time averaged spectra of all 28 GRBs are derived elsewhere [KA05].

Figure 3.11 shows that no systematic is associated with the burst direction in bursts

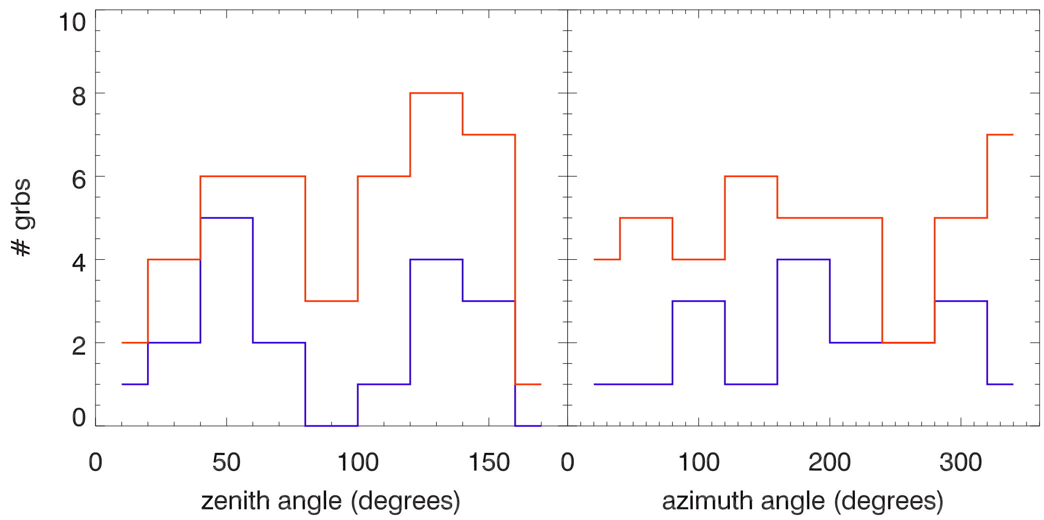

Figure 3.11: Histograms of zenith and azimuth angles for the selected bursts. Red and blue lines correspond to all burst passing the selection criteria and only the ones with more than one TASC spectrum with significant detection, respectively. Same angle distribution is observed in both cases.

with significant TASC detection in more than one spectrum, since they show the same zenith and azimuth angle distributions than the complete set of selected bursts. Therefore, the only obvious characteristic of those bursts with significant TASC detection in more than one spectrum is to have a high total fluence, mainly above 300keV.

3.5 Methodology

All the elements for the analysis of the time-resolved, BATSE-TASC spectra have been discussed in the previous sections. In this section all the details of the analysis procedure will be described.

The BATSE energy ranges used in the analysis were resulting from extracting the lowest and highest energy channels, see section 3.1. The first six energy channels of each

TASC spectra were subtracted from the spectra because of their lower count rates due to edge effects in the discrimination threshold. The last TASC energy channel included in the spectra was the one before the spectral contribution of cosmic muons. BATSE and TASC energy ranges were different for each burst since the spectral calibration was time dependent, see section 3.2.2 and reference [FI89].

As mentioned in section 3.1, BATSE spectra have finer accumulation times than TASC ones, so BATSE spectra were added up to match, as well as possible, the accumulation time and times of TASC spectra.

Because RMFIT fitting code acts on background subtracted spectra, it was necessary to build a background model. This model was based on spectra around the burst trigger since the background mostly depended on the spacecraft position with respect to the Earth's magnetic field. The time dependency of TASC background was modeled by a polynomial of 4th order on each energy bin using spectra for $\sim$500s before and after the burst trigger. The background model for each burst was checked against data corresponding to 15 orbits earlier/later when the spacecraft was located at the same geomagnetic rigidity. Figure 3.12 shows TASC spectra for the BATSE trigger on 990803 and for 15 orbits earlier. As observed, even small and sudden changes in the background are present in data for the BATSE trigger as well as 15 orbits earlier. Clearly, data for 15 orbits earlier/later to the BATSE trigger also helps to differentiate a real burst from a background fluctuation.

Figure 3.13 shows the spectrum for a BATSE trigger with a very significant TASC

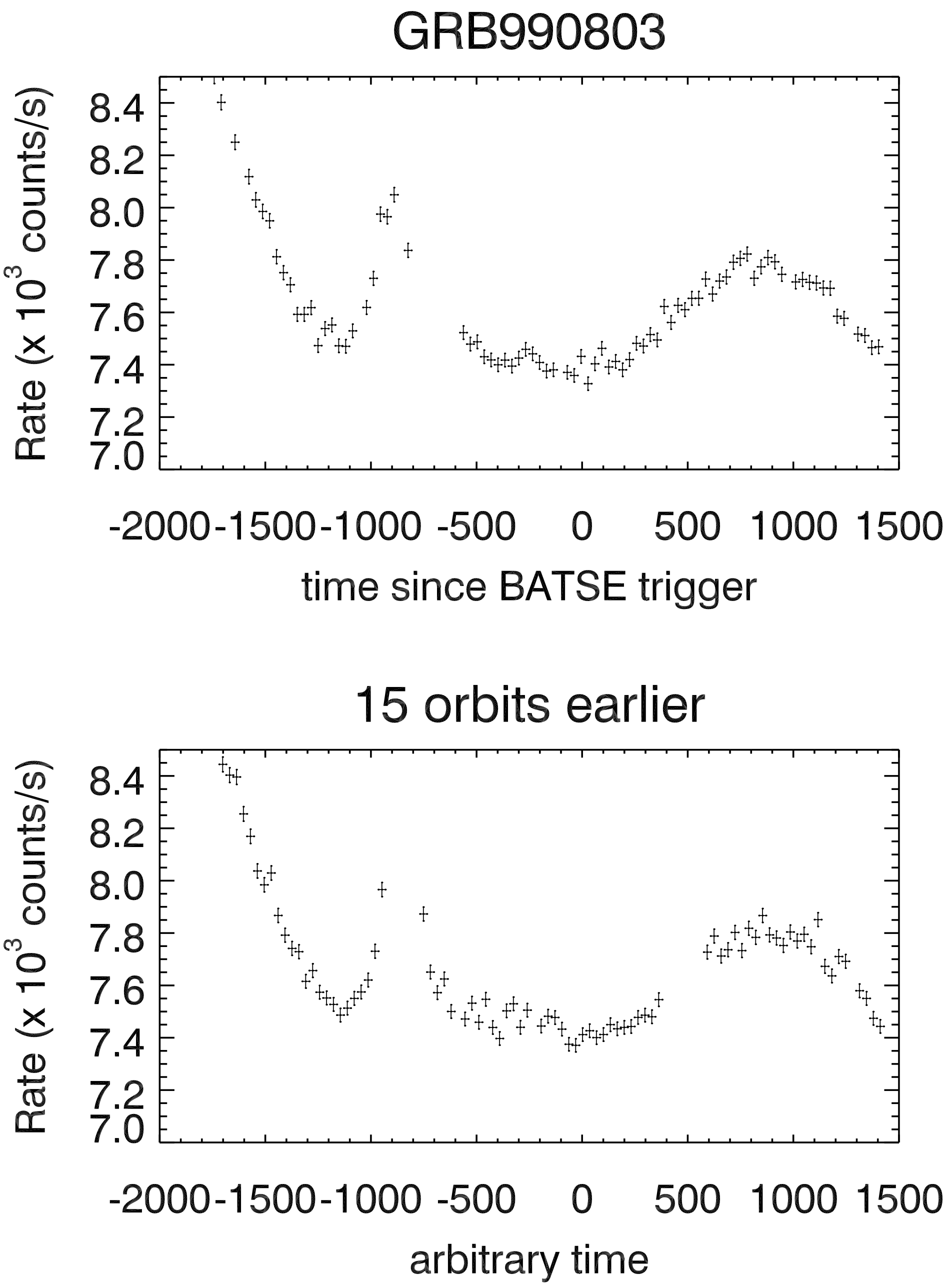

Figure 3.12: TASC count rates for the BATSE trigger corresponding to GRB990803 are shown in the upper panel. There was not TASC detection associated to this BATSE burst. The background model for each burst was checked against data corresponding to 15 orbits earlier (lower panel) or later to differentiate a real burst from a background fluctuation.

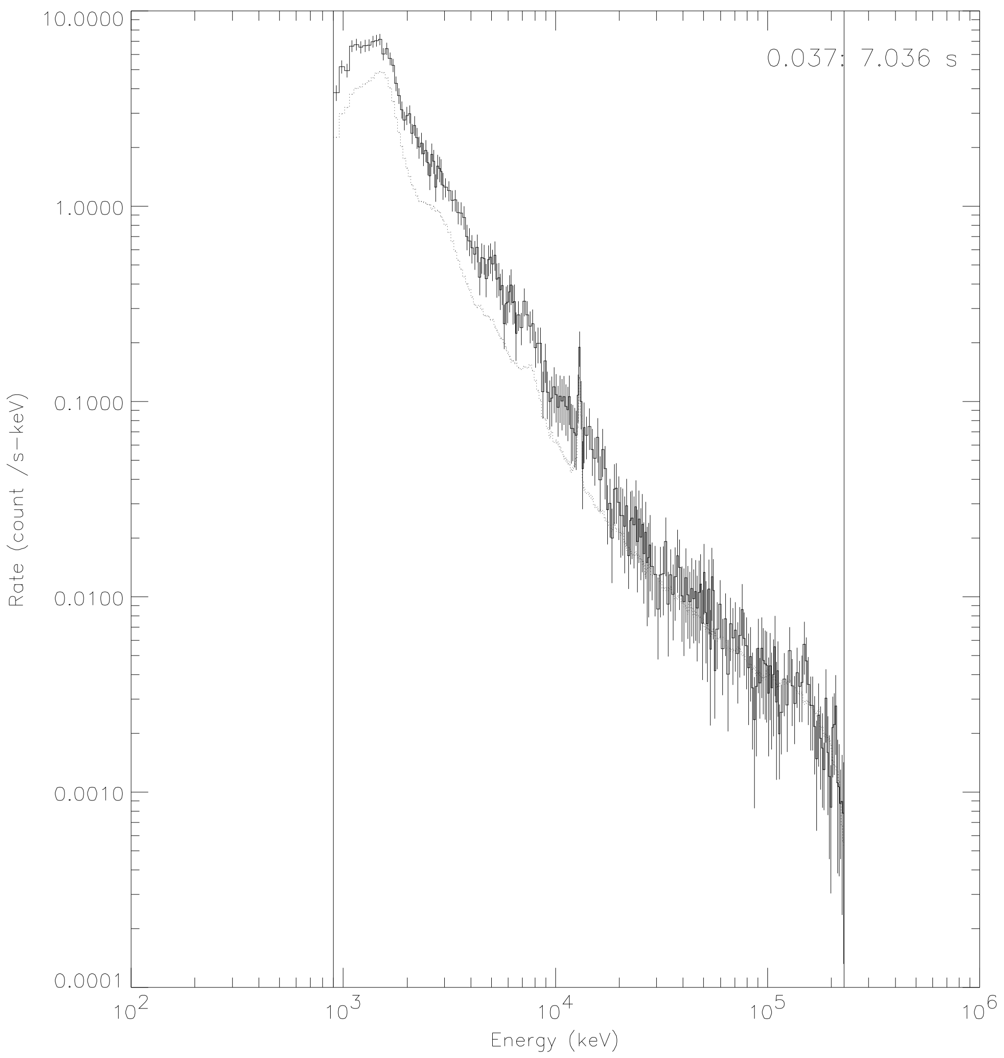

Figure 3.13: Typical TASC spectrum with significant detection. TASC time accumulated spectrum for the first 7s after the BATSE trigger of GRB910503 is shown. The crosses are for TASC data. The dotted line represents the background model (see text for details).

detection. The symbols are the time accumulated spectra for the three burst-spectra (1, 2 and 4s). The dotted line represents the background model for this burst. The difference between the symbols and the curve will yield the background subtracted spectra.

The "Band function" was chosen as the photon flux model since it well-describes most BATSE GRB spectra [BA93, PR98, PR00]. However, for the purposes of this analysis, the choice of photon flux model, at least between "Smooth Broken Power Law", "Broken Power Law" and "Band function", makes no difference in the results. For instance, figure 3.14 shows the characteristic parameters that describe the low and high energy emissions as power law functions for the SBPL and Band function photon models. As observed, the high energy index, β, takes almost equal values for both models. A similar result is obtained when compared with BPL.

As mentioned in section 3.3, RMFIT code has the capabilities of introducing a normalization factor between different data sets. If the detector responses were perfectly known, the normalization factor would be 1. The normalization factor for combining data from two BATSE LADs is close to 1 which is expected for two or more equal detectors. The normalization factor is expected to be constant through the burst duration, but different between bursts. In this analysis, the normalization factor was fixed to that obtained in the combined fit of the most significant TASC spectrum and the related BATSE spectrum.

The "observed energy flux" in a given energy bin is the "predicted energy flux" (de-

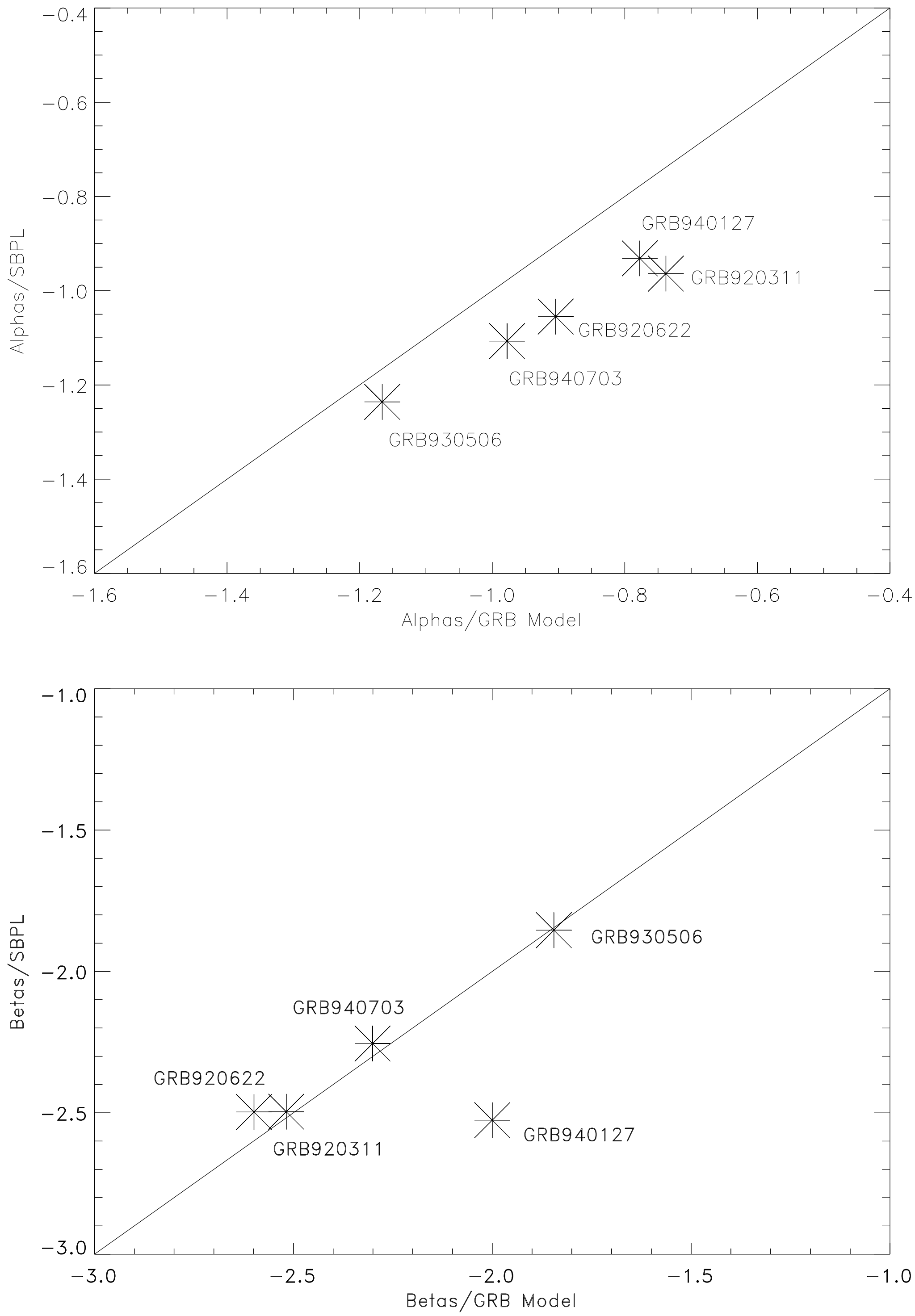

Figure 3.14: Best fit paremeters for the Band and Smooth Broken Power Law photon models are compared. Alpha and beta correspond to the low and high energy spectral indexes for each model. Joint BATSE-TASC data were fitted using these models to show that the choice of photon model is irrelevant to determine the high energy spectral index. The determination of the low energy spectral index and the value of χ^2 are dominated by BATSE data.

duced from the photon flux model) multiplied by the ratio of predicted and observed count rates in the energy bin. The background is assumed to follow a Gaussian distribution, so then the count rates predicted by the background model follow a Gaussian distribution too. The standard deviations of the predicted count rates are calculated for each energy bin. If the "background-subtracted observed count rate" is less than one standard deviation, an upper limit equivalent to two standard deviations will be plotted. This is two standard deviations times the ratio of predicted and observed count rates. Therefore, even though the symbols of the plots represent the data, they are model dependent. The error bars are calculated in the same way. It is important to point out that it is not correct to compare energy fluxes from a different photon flux model with the data given in the νF_ν plots.

3.6 Results for every burst

As mention in section 3.4, this analysis is concentrated only in bursts that had more than one TASC significant spectrum since the goal is to characterized time resolved spectra in a broad energy range. Table 3.2 gives the chosen BATSE spectra (as explained in section 3.1), the type of TASC spectra that presented significant emission, the maximum energy included in the fit (determined as explained in section 3.5), the normalization factor (fixed as explained in section 3.5), the burst duration defined by T90, the time coverage of TASC significant spectra and the percentage of the burst duration that represents. It is also indicated when the burst presented more than one episode or peak in the lightcurve. As observed, TASC data coverage is bad when the burst duration is only a few seconds.

Figure 3.15 shows the normalization factor as function of the burst direction. The correlations of the normalization factor with zenith and azimuth angles can be explained as consequence of the dependency of TASC response on the burst direction, see figure 3.5. The normalization factors also differ greatly from 1 because of the discrepancies observed between the simulated and measured TASC responses.

The Band parameters that describe the observed spectra for each burst as well as the χ^2/d.o.f. for the best fit are summarized in Table 3.3. To better visualize the temporal evolution of the burst spectrum and its implications, the lightcurves observed by BATSE and TASC and the energy fluences are plotted in figures 3.16-3.33 for each of the bursts. χ^2/d.o.f. is minimized to find the best set of Band parameters describing the data, but it is important to point out that a value very close or different to one does not necessary mean a good or bad description of the data behavior. For instance, GRB940217 in the third time interval has a $\chi^2/\text{d.o.f.} = 495/219 = 2.3$, but the errors of the determined parameters are low with respect to the parameter values and the Band parameters describe the general behavior of the combined BATSE-TASC data, see right panel of figure 3.20. GRB941017 in the fourth time interval has a $\chi^2/\text{d.o.f.} = 257/224 = 1.1$, but the parameter's errors are large and the Band parameters do not describe the behavior of the BATSE-TASC data at all, see right panel of figure 3.23. In general, the value of χ^2/d.o.f. is mainly determined by the BATSE data since the BATSE error bars are

Table 3.2: Information on analysis settings. Second and third columns indicate the type of BATSE and TASC data used in the analysis of each burst. Fourth, fifth and seventh columns give the maximum energy, the normalization factor and the time interval covered by TASC data taken for the analysis. BATSE T90 is given in the sixth column.

GRB	**BATSE spectra**	**TASC spectra**	E^{fit}_{max} **(MeV)**	**N**	**T90 (s)**	**TASC time (s)**	**multi peaked**
910503	hh	s,b	201	0.66	50.82	39.77 (0.78)	y
	co	s,b	201	0.58	50.82	39.77 (0.78)	
920311	hh	b	112	0.41	∼23	22.00 (0.96)	n
920622	hh	b	103	0.63	35.97	23.00 (0.64)	n
930506	mc	b	167	0.54	22.14	22.00 (0.99)	n
940217	co	s	177	0.62	150.14	131.10 (0.87)	y
940703	co	s	139	0.35	34.88	65.54 (1.88)	y
940921	hh	b	178	0.58	39.94	20.00 (0.51)	n
941017	co	s	200	0.45	77.06	229.00 (2.97)	n
950425	co	b	166	0.58	59.07	65.54 (1.11)	n
970202	hh	b	100	0.48	26.69	3.00 (0.11)	n
970223	hh	b	99	0.51	16.26	22.00 (1.35)	n
970315	hh	b	171	0.32	16.83	3.00 (0.18)	n
970411	co	s	182	0.30	58.88	65.54 (1.11)	n
980923	co	s	131	0.32	33.02	65.54 (1.98)	y
981021	hh	b	206	0.61	99.58	3.00 (0.03)	n
990104	co	s	193	0.39	174.46	98.30 (0.56)	y
990123	co	s	128	0.79	63.36	65.54 (1.03)	n
990506	hh	b,s	123	0.31	130.05	52.77 (0.41)	y
	co	b,s	123	0.69	130.05	52.77 (0.41)	

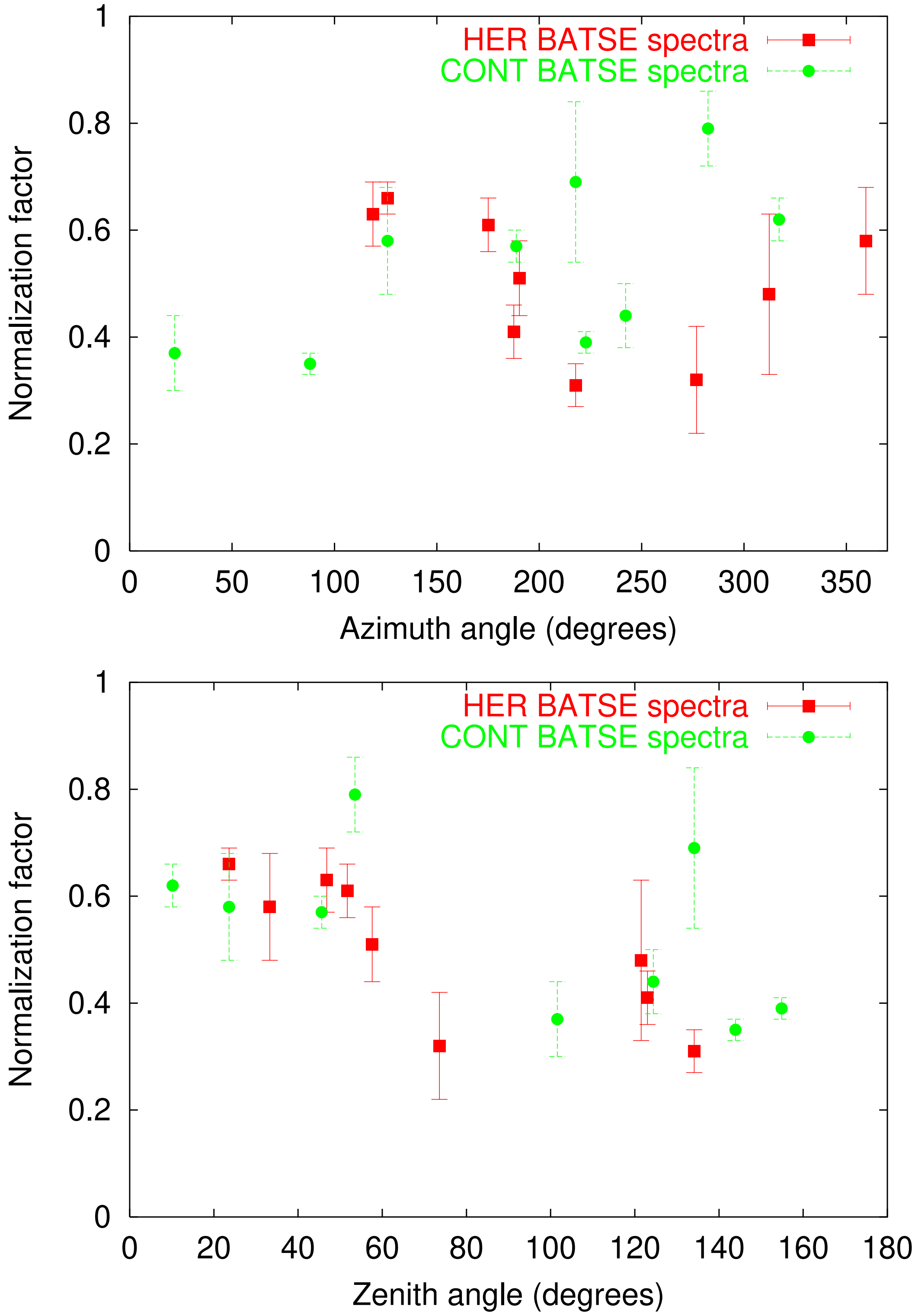

Figure 3.15: Normalization factor as function of the azimuth and zenith angles for the bursts included in this analysis. The observed trends are similar to the observed in the TASC sensitivity, 3.5. The normalization factors differ from 1 because of the discrepancies observed between the simulated and measured TASC responses. Note that the normalization factor used is independent of the BATSE spectrum format.

much smaller than those of the TASC data. Variations in χ^2/d.o.f. are used to find the best parameter set and to judge the need of an extra parameter in the photon flux model.

Table 3.3: Joint BATSE-LAD and EGRET-TASC spectral fits to the Band function.

T from trig(s)	A($\times 10^{-3}$ (phcm^{-2}s^{-1}keV^{-1})	E$_{\mathrm{peak}}$ **(keV)**	α	β	χ^2/d.o.f
GRB 910503					
0 to 1	49.3 ± 0.9	1040 ± 74	-0.51 ± 0.04	-2.03 ± 0.04	374/325
1 to 3	320.7 ± 2.7	727 ± 16	-0.6 ± 0.01	-2.22 ± 0.02	380/325
3 to 7	132.8 ± 1.2	600 ± 15	-0.91 ± 0.01	-2.6 ± 0.05	394/325
23 to 56	9.5 ± 0.1	1128 ± 118	-1.37 ± 0.02	$-2.6^{+0.24}_{-0.58}$	187/223
GRB 920311					
1 to 3	$9.8^{+4.6}_{-1.5}$	387^{+345}_{-161}	$-1.04^{+0.38}_{-0.20}$	$-1.71^{+0.06}_{-0.08}$	301/302
7 to 23	94.0 ± 1.4	303 ± 5	-0.74 ± 0.02	-2.54 ± 0.03	595/302
GRB 920622					
0 to 1	50.7 ± 1.8	605^{+104}_{-84}	-1.30 ± 0.04	$-2.21^{+0.13}_{-0.17}$	312/293
1 to 3	60.7 ± 1.3	554 ± 32	-0.90 ± 0.03	-2.37 ± 0.09	323/293
3 to 7	79.0 ± 1.6	379 ± 14	-0.94 ± 0.02	-2.43 ± 0.07	342/293
7 to 23	58.7 ± 0.4	578 ± 11	-0.90 ± 0.01	-2.58 ± 0.05	441/293
GRB 930506					
1 to 3	41.4 ± 1.3	544 ± 58	-1.06 ± 0.04	-1.92 ± 0.06	211/218
3 to 7	91.3 ± 0.6	1094 ± 38	-0.90 ± 0.01	-1.90 ± 0.02	306/218
7 to 23	72.6 ± 0.4	866 ± 32	-1.24 ± 0.01	-1.91 ± 0.02	286/218
GRB 940217					
-8 to 25	11.1 ± 0.1	1018 ± 32	-0.79 ± 0.02	$-3.17^{+0.22}_{-0.38}$	272/219
25 to 90	12.9 ± 0.1	675 ± 26	-1.21 ± 0.01	$-3.70^{+0.53}_{-\infty}$	218/219
90 to 123	40.2 ± 0.2	676 ± 14	-1.03 ± 0.01	-2.73 ± 0.07	495/219
GRB 940703					
-1 to 32	11.1 ± 0.2	1121 ± 135	-1.09 ± 0.03	-1.92 ± 0.06	199/206
32 to 64	110.6 ± 0.5	613 ± 9	-0.96 ± 0.01	-2.42 ± 0.03	305/206
GRB 940921					

Table 3.3: *continued*

T from trig(s)	A($\times 10^{-3}$ (phcm^{-2}s^{-1}keV^{-1})	E$_{\rm peak}$ **(keV)**	α	β	χ^2/d.o.f
3 to 7	25.4 ± 0.5	810 ± 72	-1.01 ± 0.03	-2.21 ± 0.08	334/320
7 to 23	27.0 ± 0.3	731 ± 31	-1.11 ± 0.02	-2.62 ± 0.11	373/320
GRB 941017					
-18 to 14	0.01 ± 0.0005	503 ± 58	-0.83 ± 0.08	-2.21 ± 0.11	191/224
14 to 47	0.06 ± 0.001	343 ± 8	-0.77 ± 0.02	-2.36 ± 0.03	291/224
47 to 80	0.02 ± 0.002	231 ± 15	-1.05 ± 0.07	-2.35 ± 0.09	268/224
80 to 113	0.006 ± 0.004	90 ± 24	-1.59 ± 0.54	-2.24 ± 0.17	257/224
113 to 210	$0.0004 \pm \infty$	$19 \pm \infty$	$-1.24 \pm \infty$	-1.30 ± 0.06	235/224
GRB 950425					
-24 to 9	16.9 ± 0.1	1125 ± 45	-0.79 ± 0.02	-2.08 ± 0.03	249/210
9 to 42	16.4 ± 0.3	653 ± 44	-0.97 ± 0.03	-1.99 ± 0.03	225/210
42 to 75	10.0 ± 0.1	977 ± 71	-0.93 ± 0.03	-2.42 ± 0.12	191/210
GRB 970202					
0 to 1	38.8 ± 1.9	500 ± 32	0.09 ± 0.08	-2.18 ± 0.09	430/292
1 to 3	42.0 ± 0.9	644 ± 26	-0.21 ± 0.04	$-2.80^{+0.19}_{-0.31}$	360/292
GRB 970223					
1 to 3	$6.2^{+0.7}_{-0.5}$	831^{+578}_{-275}	$-1.01^{+0.16}_{-0.14}$	$-1.80^{+0.12}_{-0.21}$	306/294
3 to 7	35.9 ± 0.7	676 ± 39	-0.80 ± 0.03	-2.11 ± 0.05	295/294
7 to 23	32.6 ± 0.5	439 ± 17	-1.03 ± 0.02	-2.47 ± 0.08	327/294
GRB 970315					
0 to 1	54.9 ± 1.9	572 ± 49	-0.78 ± 0.05	$-2.30^{+0.12}_{-0.17}$	327/317
1 to 3	$79.6^{+7.9}_{-1.5}$	309 ± 21	-0.94 ± 0.05	-2.21 ± 0.07	375/317
GRB 970411					
6 to 39	22.8 ± 0.9	430 ± 42	-1.00 ± 0.04	-1.74 ± 0.02	218/219
39 to 72	10.0 ± 1.9	244 ± 70	-1.09 ± 0.18	-1.82 ± 0.07	190/219
GRB 980923					
-19 to 13	49.4 ± 0.08	344 ± 7	-0.47 ± 0.02	-2.44 ± 0.06	230/198
13 to 46	162.2 ± 1.0	388 ± 4	-0.66 ± 0.01	-2.93 ± 0.06	436/198
GRB 981021					

Table 3.3: *continued*

T from trig(s)	A($\times 10^{-3}$ (phcm^{-2}s^{-1}keV^{-1})	E$_{\rm peak}$ **(keV)**	α	β	χ^2/d.o.f
0 to 1	31.5 ± 0.6	1605 ± 89	-0.50 ± 0.03	$-3.73^{+0.56}_{-1.33}$	344/317
1 to 3	46.8 ± 0.5	1591 ± 57	-0.55 ± 0.02	-2.87 ± 0.12	367/317
GRB 990104					
-5 to 28	23.9 ± 0.9	415 ± 43	-1.17 ± 0.04	$-2.39^{+0.10}_{-0.14}$	266/215
127 to 159	11.3 ± 0.4	2307 ± 352	-1.34 ± 0.06	$-3.06^{+0.37}_{-\infty}$	218/215
159 to 192	131.3 ± 1.2	640 ± 27	-1.22 ± 0.01	-2.38 ± 0.02	305/215
GRB 990123					
0 to 33	30.8 ± 0.2	734 ± 14	-0.62 ± 0.01	-2.49 ± 0.05	277/200
33 to 66	44.6 ± 0.3	541 ± 10	-0.88 ± 0.01	-2.73 ± 0.08	378/200
GRB 990506					
3 to 7	51.2 ± 0.5	878 ± 48	-1.16 ± 0.02	-2.72 ± 0.13	279/298
7 to 23	24.1 ± 0.5	411 ± 16	-0.81 ± 0.04	$-3.49^{+0.38}_{-0.80}$	280/298
70 to 102	56.4 ± 1.6	199 ± 5	-1.02 ± 0.02	-2.25 ± 0.04	251/197
102 to 135	36.9 ± 1.7	178 ± 6	-0.93 ± 0.04	-2.37 ± 0.07	212/197

The lightcurves observed by BATSE and TASC present the same general features for the same burst. A bright episode in TASC lightcurve corresponds to a bright episode in the BATSE lightcurve. This is more obvious for bursts with well separated peaks, see left panels of figures 3.16, 3.20 and 3.33. Even more, a decrease in the emission in the BATSE energy range implies a decrease in the TASC energy range in most of the bursts. This correlation is important to assure that TASC observations correspond to the same source that triggered BATSE. Otherwise this is not evident because TASC can not determine source direction.

Most of the bursts have spectra that can be described by the Band function. There is not an evident need of a sharper photon flux model as the SBPL or BPL, at least up to a few MeV. Except for two bursts (that will be discussed in detail in a later section), there is no evident need of a second spectral break or in other words the inclusion of an extra power law to described the data.

Since the burst emission at MeV-energies is very close to the TASC sensitivity, the significance of the TASC detection extends to higher energies when two conditions stand (see figures 3.16-3.33): 1.-the bursts is very bright as indicated by greater values of the amplitude of the Band function, A and, 2.- The burst spectra peak (in νF_ν presentation) is at energies close to 1MeV as indicated by E_{peak}. In general, the TASC detections are significant up to ~10MeV. To estimate the maximum photon energy observed from the source, the spectra was binned in energy bins of 2 and 3 sigma of significance over the background. Each energy bin was obtained by adding up original energy channels starting from the lowest energies. Table 3.4 shows the energy edges of the last energy bin with 2 and 3 sigma of significance over the background. This energy bin is clearly a lower limit for the maximum photon energy observed from the source.

The results for the temporal evolution of the three Band parameters, low energy spectral index, peak energy and high energy spectral index, for individual bursts are the following:

GRB910503 had 4 TASC spectra with significant detection, see figure 3.16. It had two peaks in two separated episodes. The first and brightest peak yielded three TASC burst spectra covering its brightest section. The second peak is covered by a TASC

Table 3.4: Estimates of mximum photon energy observed by TASC. The energy edges of the last energy bin with 2 and 3 sigma of significance over the background are given in the last 2 columns respectively. For comparison, the maximum energy used in the analysis is given in the second column.

GRB	E^{fit}_{max} **(MeV)**	$E^{det}_{l,2\sigma}$ - $E^{det}_{h,2\sigma}$ **(MeV)**	$E^{det}_{l,3\sigma}$ - $E^{det}_{h,3\sigma}$ **(MeV)**
910503	201	12.9 - 71.4	22.3 - 78.6
920311	112	5.1 - 5.4	4.7 - 5.6
920622	103	5.5 - 19.6	2.8 - 5.6
930506	167	39.6 - 45.4	29.0 - 39.6
940217	177	4.6 - 6.1	4.1 - 12.7
940703	139	24.8 - 101.1	13.2 - 24.8
940921	178	5.1 - 6.1	3.8 - 5.4
941017	200	36.6 - 68.5	8.0 - 13.9
950425	166	59.4 - 86.5	21.6 - 35.2
970202	100	1.6 - 2.7	1.2 - 1.8
970223	99	5.2 - 10.6	3.0 - 5.4
970315	171	0.0 - 171.0	——-
970411	182	13.9 - 26.1	3.8 - 13.0
980923	131	19.8 - 36.3	11.3 - 37.3
981021	206	3.9 - 5.0	3.5 - 4.0
990104	193	24.1 - 30.7	19.5 - 27.6
990123	128	7.0 - 14.7	4.6 - 5.8
990506	123	3.8 - 5.5	2.4 - 2.8

solar spectrum. The second peak lasted about 10 seconds, so the significance of the TASC spectrum was low. The temporal evolution of the parameters for the first peak is from hard to soft. The second peak keeps the same high-energy spectral index but the peak energy increases to higher values than the observed in the first episode. The spectral index for low energies violates the line of death (see section 1.2).

GRB920311 had 2 TASC spectra with significant detection, see figure 3.17. It had three peaks in one episode. The first TASC burst spectrum covers only the rising part of the whole episode. The second TASC burst spectrum covers completely the part of the episode with the third peak that it is also the brightest peak. There is not a clear a monotonic temporal evolution of the low energy spectral index and the peak energy. The high energy spectral index evolves in time from hard to soft.

GRB920622 had 4 TASC spectra with significant detection, see figure 3.18. It had three peaks in one episode. The first peak is covered by the first three TASC burst spectra while the last burst spectrum almost contains the last two peaks of the burst. There is not a clear monotonic temporal evolution of the low energy spectral index and the peak energy. The high energy spectral index evolves in time from hard to soft.

GRB930506 had 3 TASC spectra with significant detection, see figure 3.19. It had a single peak. Most of the peak is covered by the burst spectra. There is not an evident monotonic evolution in the low energy spectral index and the peak energy; their increment from the first to the second time intervals could be due to the increasing burst emission. The high energy spectral index stays constant through the burst.

GRB940217 had 4 TASC spectra with significant detection, see figure 3.20. The second and third spectra were added up for the analysis to increase the significance. It had six separated peaks with only the first four covered by the TASC spectra. There is no TASC spectrum containing only one peak. There is not a clear monotonic temporal evolution in any of the parameters. The temporal evolution for all the parameters seems to have the same behavior.

GRB940703 had 2 TASC solar spectra with significant detection, see figure 3.21. It had three separated episodes. The first TASC spectrum contains the first episode while the second episode is mostly contained in the second TASC spectrum. It is hard to talk about a temporal evolution of the parameters with only two spectra containing separated peaks. However, there is a hard to soft change in the high energy spectral index and the peak energy, while the low energy spectral index changes from soft to hard.

GRB940921 had 2 TASC spectra with significant detection, see figure 3.22. It was a single peak burst. The first TASC spectrum contains a period of increasing flux and the second spectrum contains the brightest and the decaying periods. The three parameters seem to follow a hard to soft evolution.

GRB941017 had 7 TASC spectra with significant detection; the last three spectra were added up to increase significance, see figure 3.23. It had a single episode with one or possibly two peaks. The first 3 TASC spectra contain the main detection as observed by BATSE. The last 4 spectra contain the tail of the BATSE observation. In this case a fit using a Band function did not described the data. The TASC data were not consistent with the model. A lot more high energy emission was detected than predicted by the model. It seems that the spectra increase again for energies above 10MeV at least after the first 47 seconds. This burst will be discussed in a later section because of this second high energy component.

GRB950425 had 3 TASC spectra with significant detection, see figure 3.24. It had two peaks in two separated episodes. The first peak is contained by the first two TASC spectra. The increasing and brightest part of the peak are contained in the first spectrum, while the decaying period of the first peak and part of the second peak are contained in the second TASC spectrum. The second peak is mostly contained in the third TASC spectrum. The is not a monotonic temporal evolution of the parameters through the whole burst. The low energy spectral index and the peak energy change from hard to soft while the high energy spectral index changes from soft to hard for the first peak.

GRB970202 had 2 TASC spectra with significant detection, see figure 3.25. It had a single peak. The two TASC burst spectra only covers the first 3 seconds of the 26.7 seconds burst duration. Both values of the low energy spectral index violate the line of death. The parameters of the best fit are given in the table 3.3 but this burst is not going to be further considered due to the small fraction of the burst duration sampled by the TASC.

GRB970223 had 3 TASC spectra with significant detection, see figure 3.26. It had a single peak. The first two TASC burst spectra cover the increasing period of the emission while the third TASC burst spectrum covers the decaying period. There is not a clear monotonic temporal evolution of the low energy spectral index; its increase in the first two spectra may be because the peak is raising. The high energy spectral index and the peak energy have a hard to soft evolution.

GRB970315 had 2 TASC spectra with significant detection, see figure 3.27. There is no BATSE data for the whole burst, possibly because of saturation of the detector. It had at least two episodes of emission. Even though TASC only covers 3 of the 16.8 seconds of the burst duration, the first episode was almost covered by TASC data, and is thus useful for the analysis. The changes in the low energy power law and the peak energy are from hard to soft while the high energy spectral index changes from soft to hard.

GRB970411 had 2 TASC spectra with significant detection, see figure 3.28. It had a single peak. The first TASC spectrum covers the increasing and brightest period of the burst. All three parameters change with time from hard to soft.

GRB980923 had 2 TASC spectra with significant detection, see figure 3.29. It had one multi-peaked episode. The first TASC spectrum was described by a Band function; however, the second TASC spectra was not well described for energies above 4MeV. The emission above those energies is again more than predicted by the model. It seems that the spectrum rises at higher energy. This burst will be discussed further in a later section.

GRB981021 had 2 TASC spectra with significant detection, see figure 3.30. It had two episodes. TASC spectra cover only a small part of the first episode. Thus, the parameters of the best fit are given in the table 3.3 but this burst is not going to be further considered.

GRB990104 had 3 TASC spectra with significant detection, see figure 3.31. It had two bright peaks and two dim peaks. The first TASC spectrum covers the first dim and bright peaks. The last two TASC spectra cover most of the second bright peak. There is not an obvious monotonic temporal evolution in the parameters. For the second bright peak, the high energy spectral index evolves with time from hard to soft while the low energy spectral index evolves from soft to hard.

GRB990123 had 2 TASC spectra with significant detection, see figure 3.32. It had one multi-peaked episode. The brightest part of the episode is covered by TASC data. The three Band parameters change from hard to soft. The low energy spectral index gets a value that violated the line of death.

GRB990506 had 4 TASC spectra with significant detection, see figure 3.33. It had 6 episodes. The first episode had two peaks. The TASC data covers the brightest episodes of the burst. There is not an evident monotonic temporal evolution of the parameters through the whole burst. The high energy spectral index and the peak energy change from hard to soft in the first episode while the low energy spectral index evolves from soft to hard.

In overall, only sixteen of the eighteen burst had spectra well-described by the

Band function. The two remaining bursts, GRB941017 and GRB980923, had only the first spectrum described by the Band function. The rest of these burst presented excess of emission at energies above ~5MeV. Two bursts, GRB970202 and GRB981021, are excluded from further analysis because most of their emission did not present a significant detection in TASC.

Figure 3.16: Counts rates and energy fluxes for GRB910503 are shown. The BATSE and TASC lightcurves are shown in the top-left and bottom-left windows, respectively. When TASC lightcurve is plotted, the solid line corresponds to the 4th order polynomial that best fits the background. Energy fluxes for GRB910503 for the time intervals shown in Table 3.3. Crosses and circles correspond to BATSE-LAD and EGRET-TASC data respectively. For the purpose of the plot, but not for the spectral fit, the TASC data are binned in energy to give at least 2σ significance over the background. The upper limits correspond to 2σ deviation from the background. The solid lines represent the best fit to the joint LAD-TASC data using a Band function described by fit parameters given in Table 3.3. The normalization factor between the data sets was fixed through the whole burst and given in 3.2.

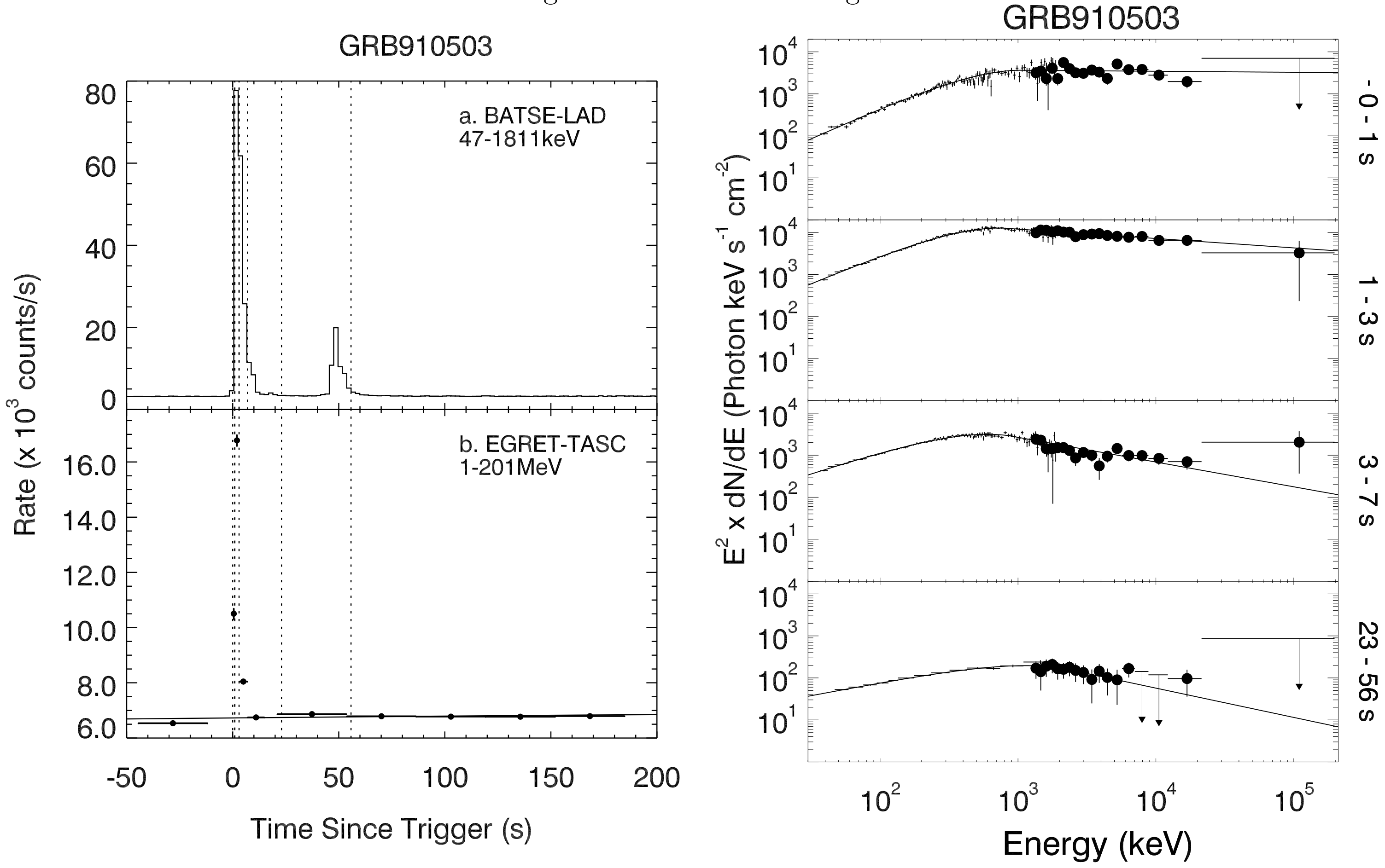

Figure 3.17: Counts rates and energy fluxes for GRB920311 are shown. Same as figure 3.16 but for GRB920311.

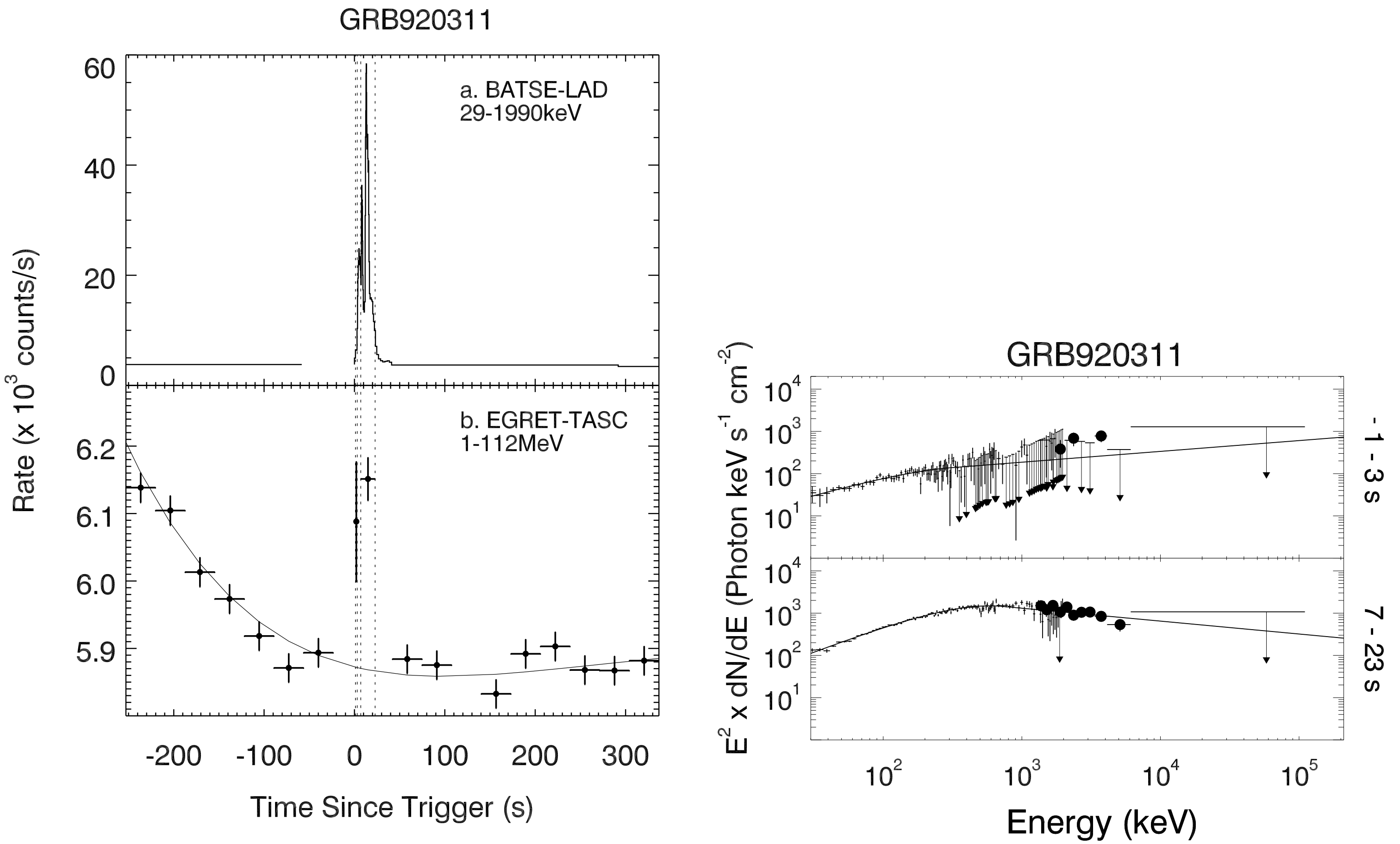

Figure 3.18: Counts rates and energy fluxes for GRB920622 are shown. Same as figure 3.16 but for GRB920622.

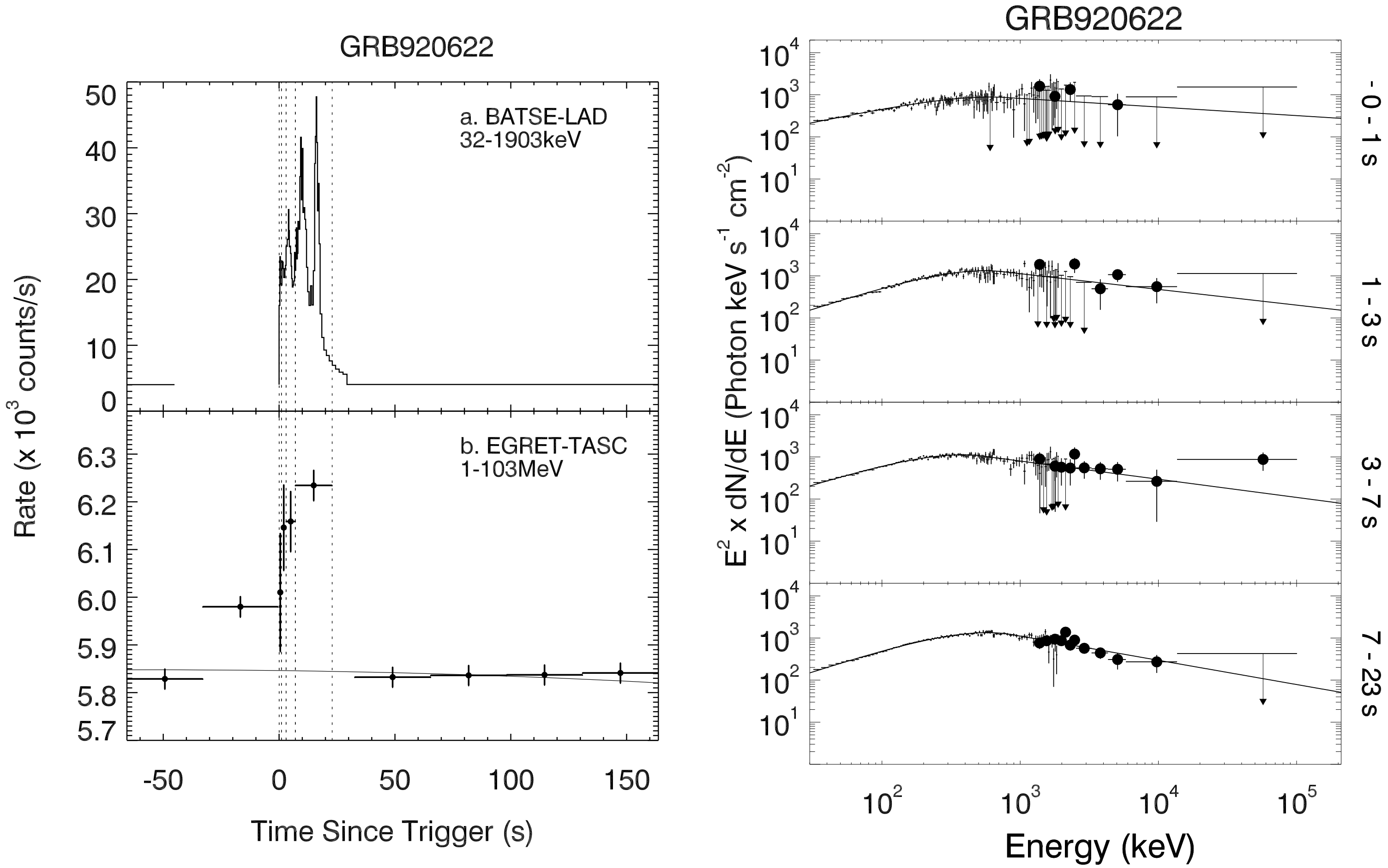

Figure 3.19: Counts rates and energy fluxes for GRB930506 are shown. Same as figure 3.16 but for GRB930506.

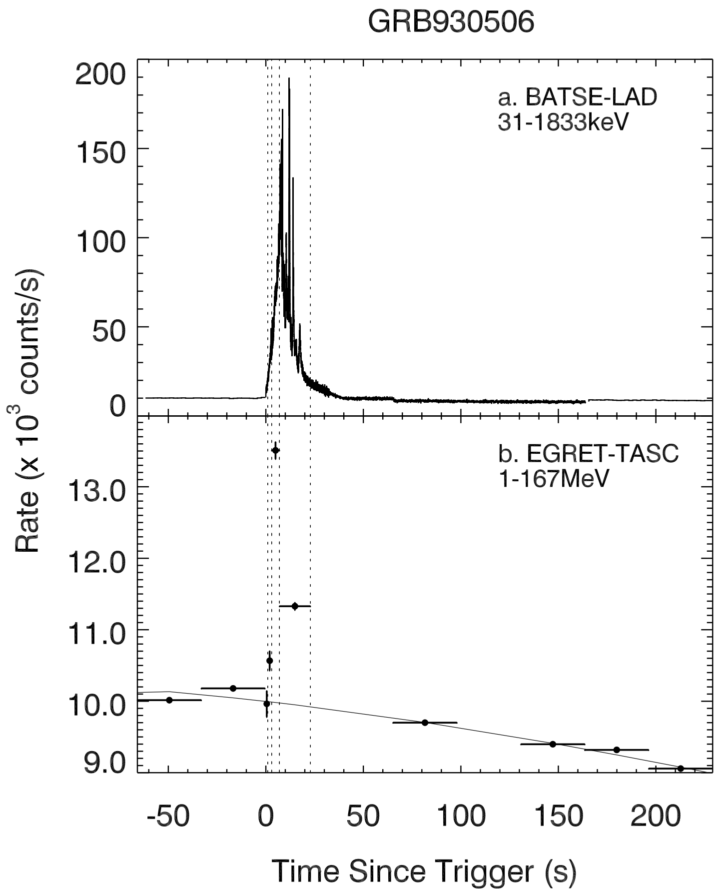

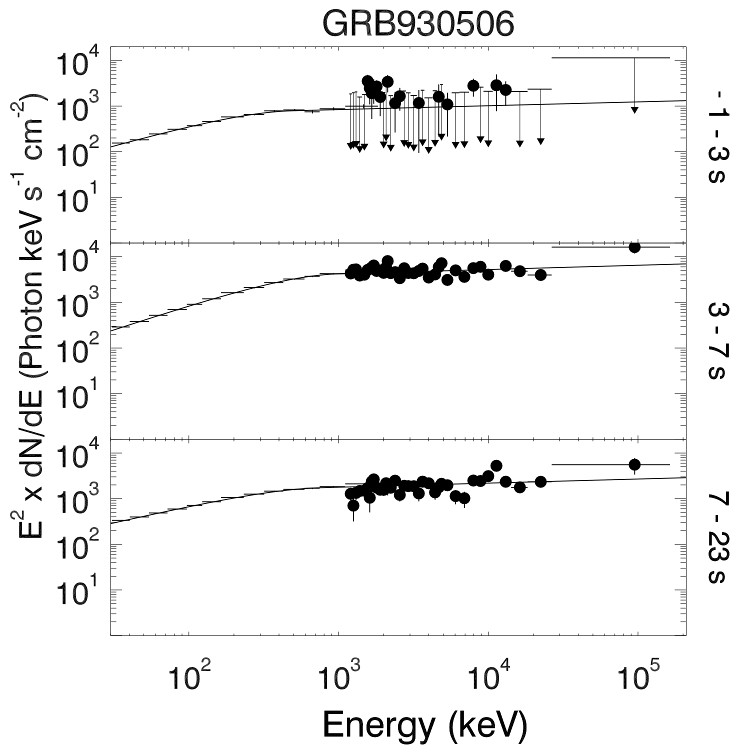

Figure 3.20: Counts rates and energy fluxes for GRB940217 are shown. Same as figure 3.16 but for GRB940217.

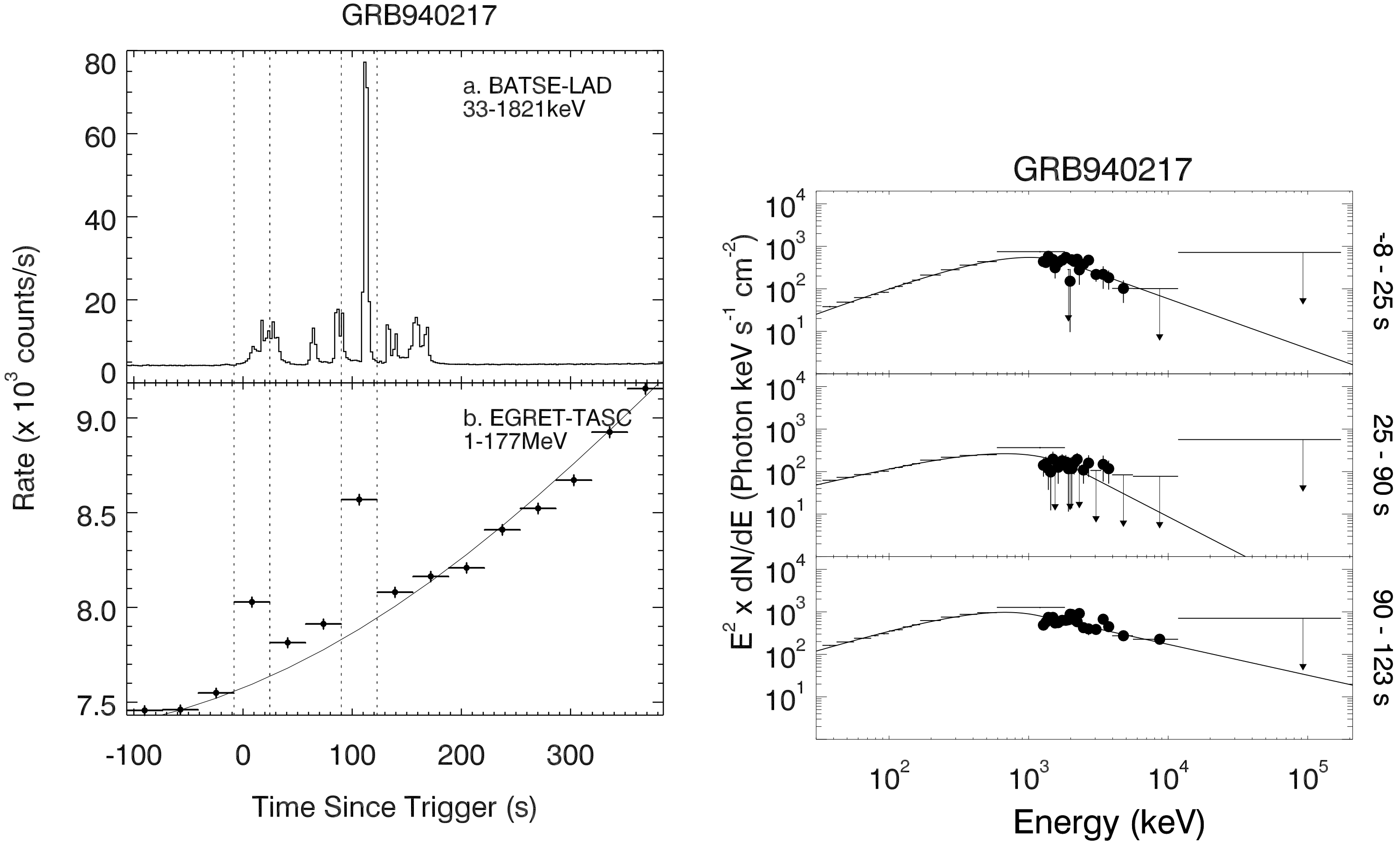

Figure 3.21: Counts rates and energy fluxes for GRB940703 are shown. Same as figure 3.16 but for GRB940703.

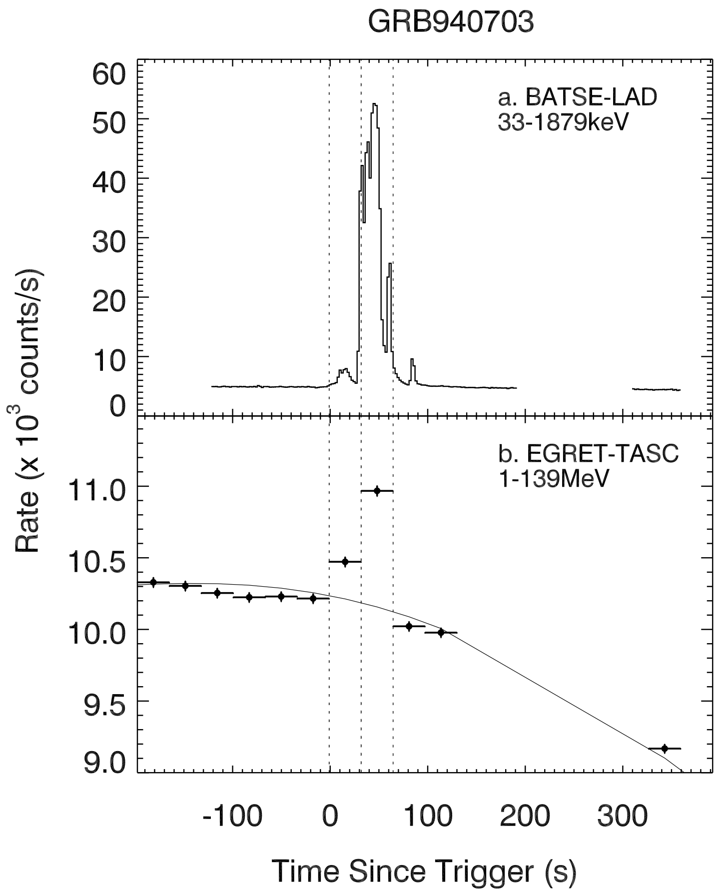

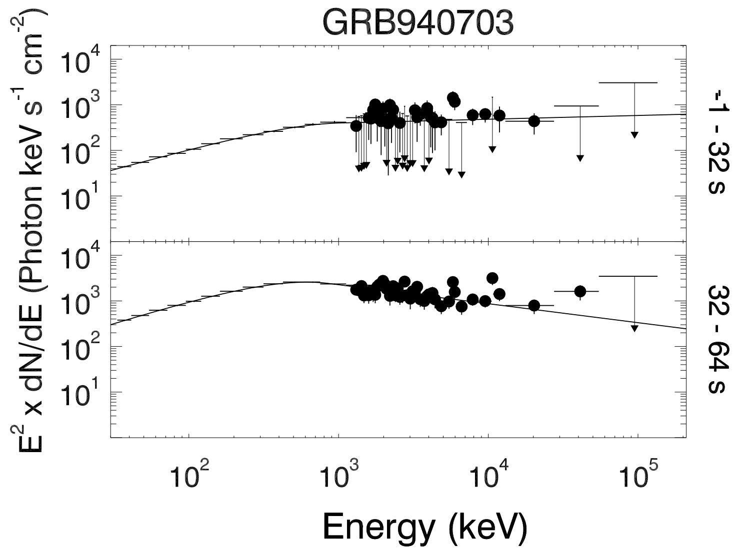

Figure 3.22: Counts rates and energy fluxes for GRB940921 are shown. Same as figure 3.16 but for GRB940921.

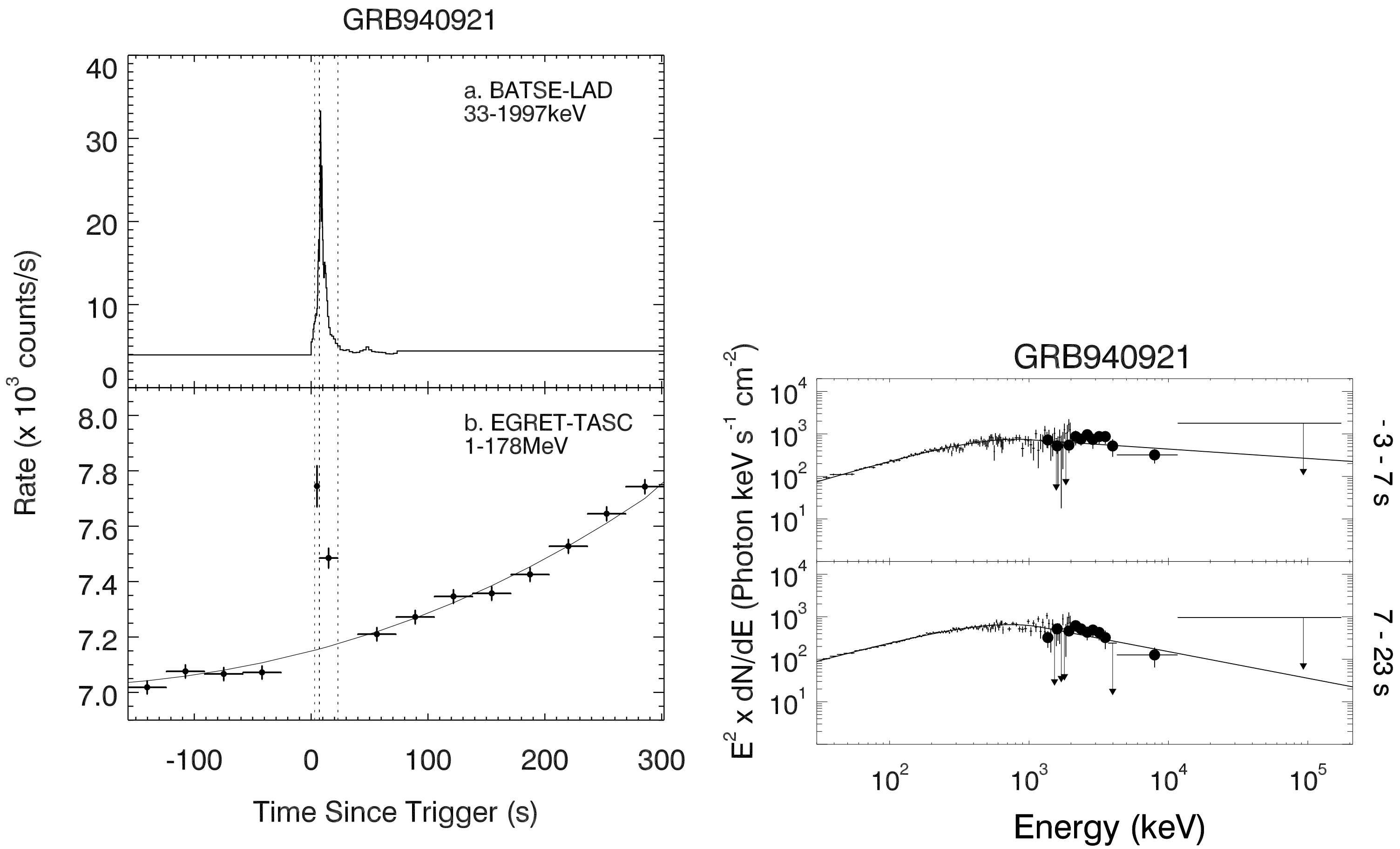

Figure 3.23: Counts rates and energy fluxes for GRB941017 are shown. Same as figure 3.16 but for GRB941017.

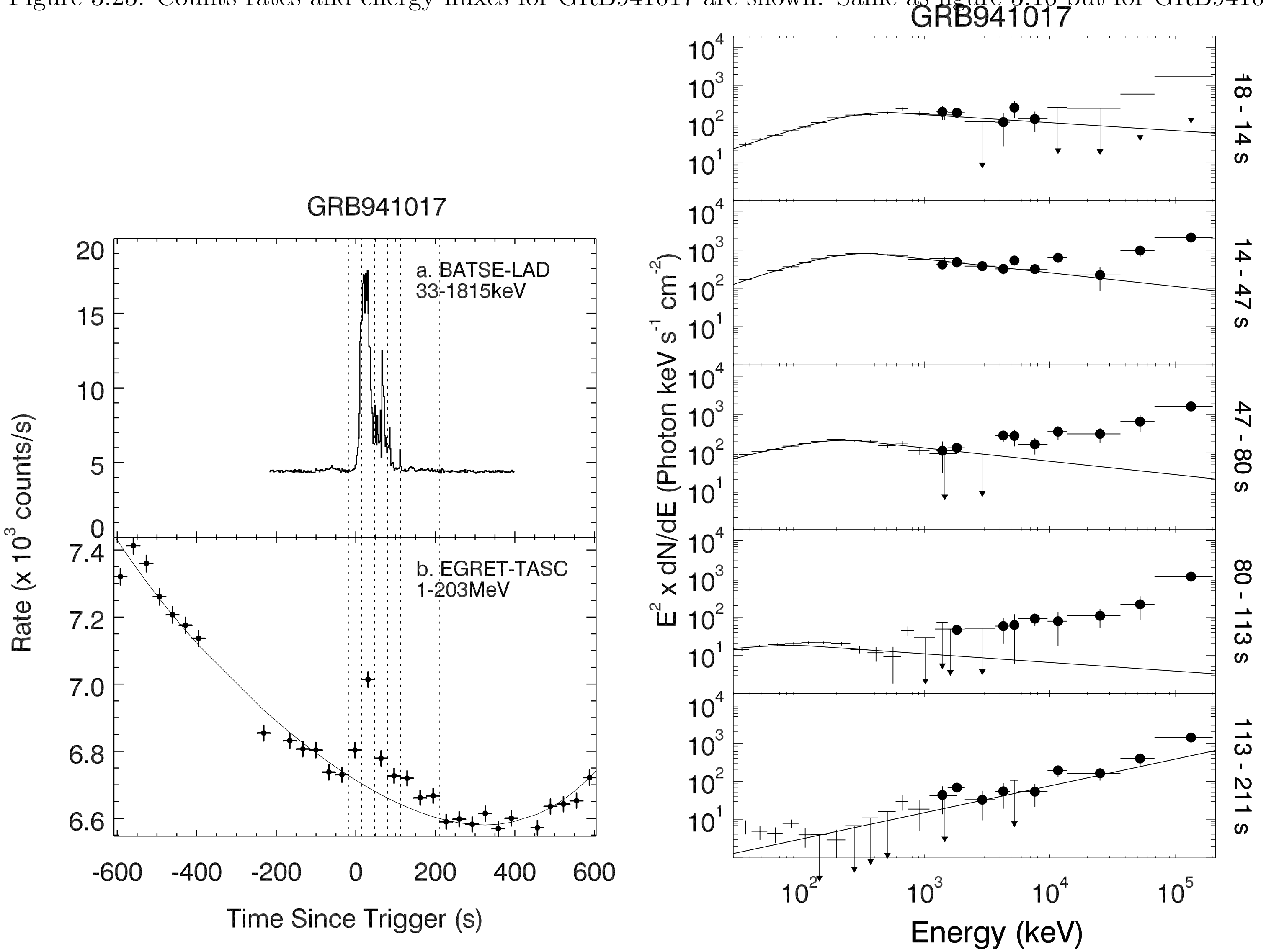

Figure 3.24: Counts rates and energy fluxes for GRB950425 are shown. Same as figure 3.16 but for GRB950425.

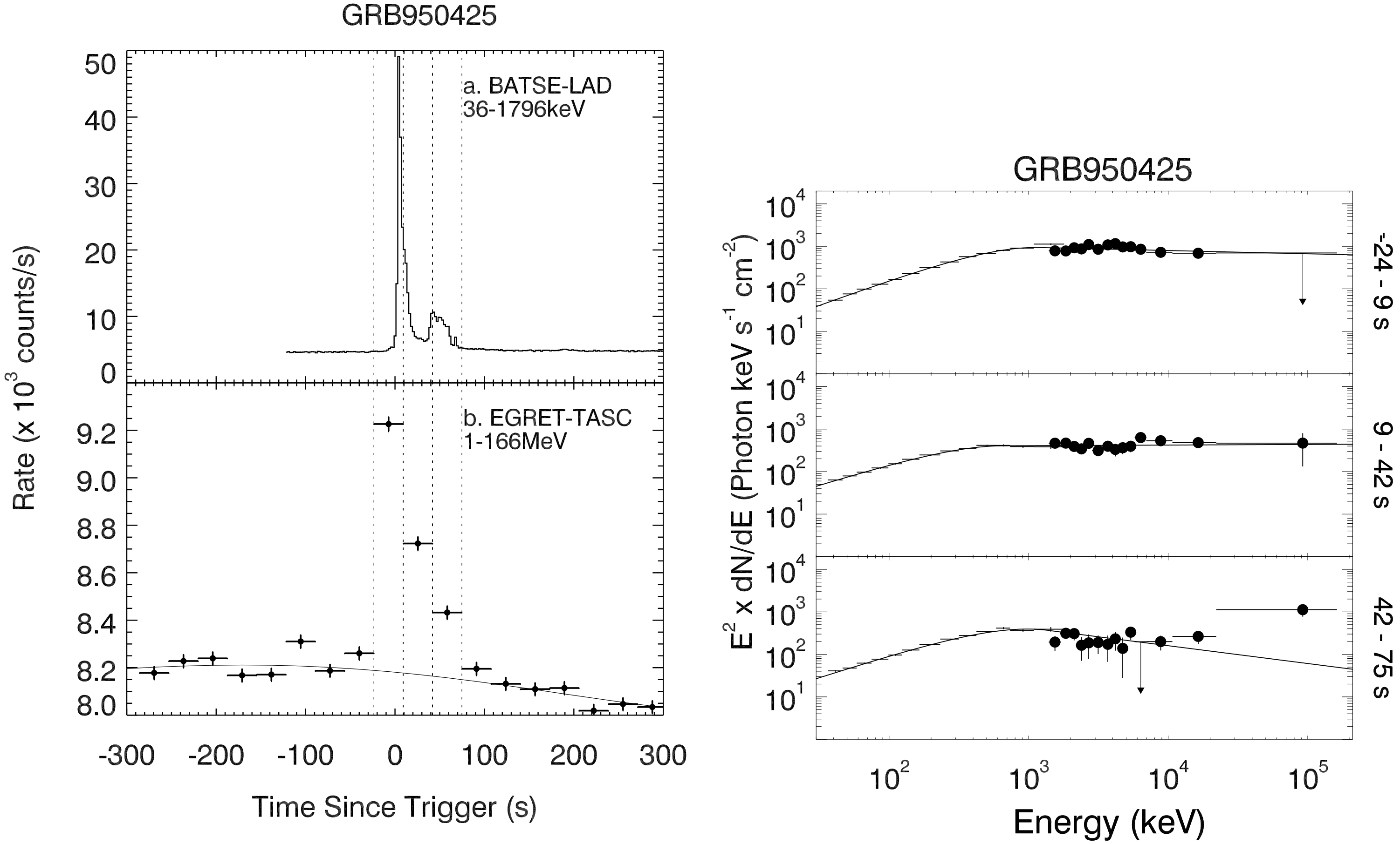

Figure 3.25: Counts rates and energy fluxes for GRB970202 are shown. Same as figure 3.16 but for GRB970202.

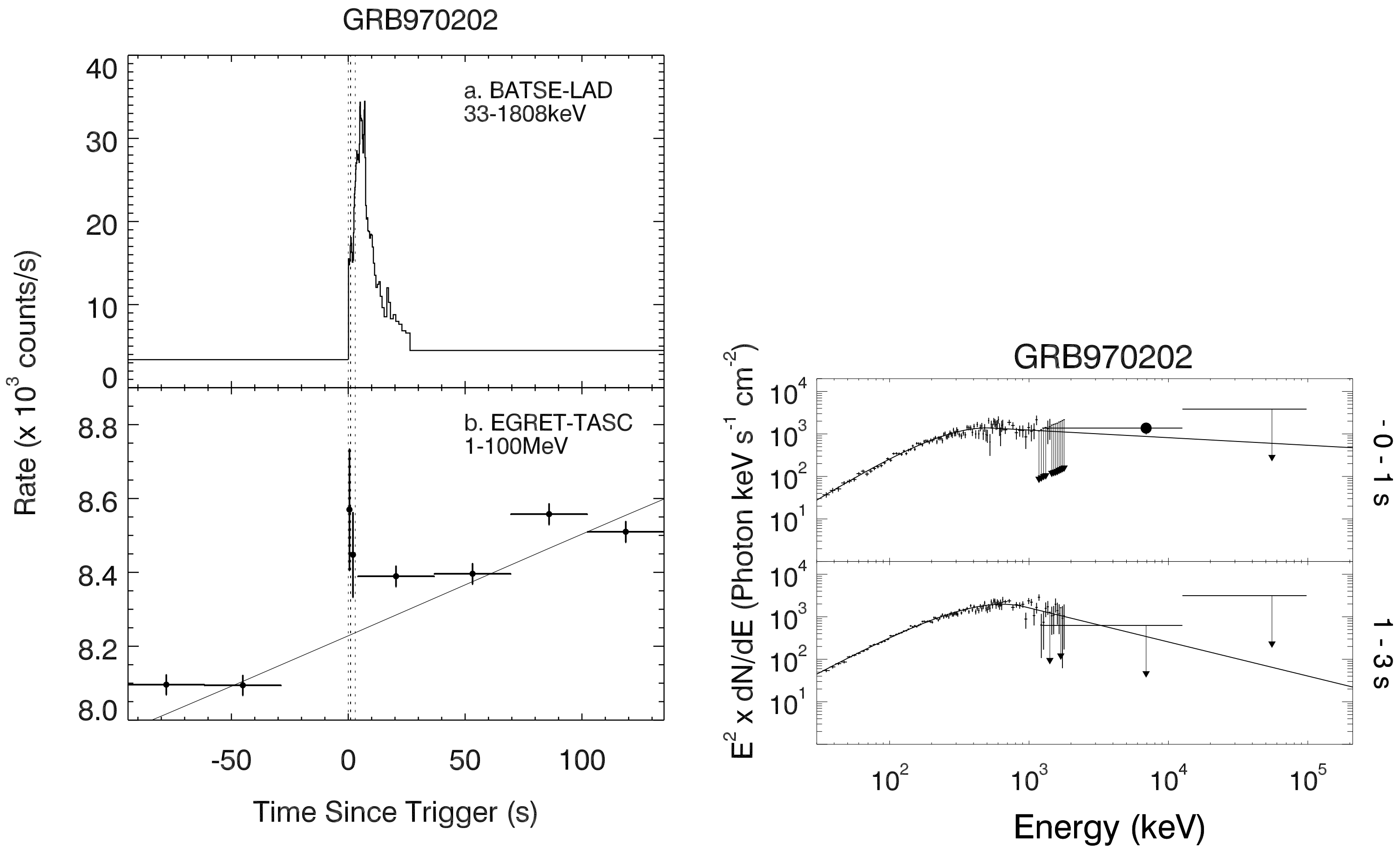

Figure 3.26: Counts rates and energy fluxes for GRB970223 are shown. Same as figure 3.16 but for GRB970223.

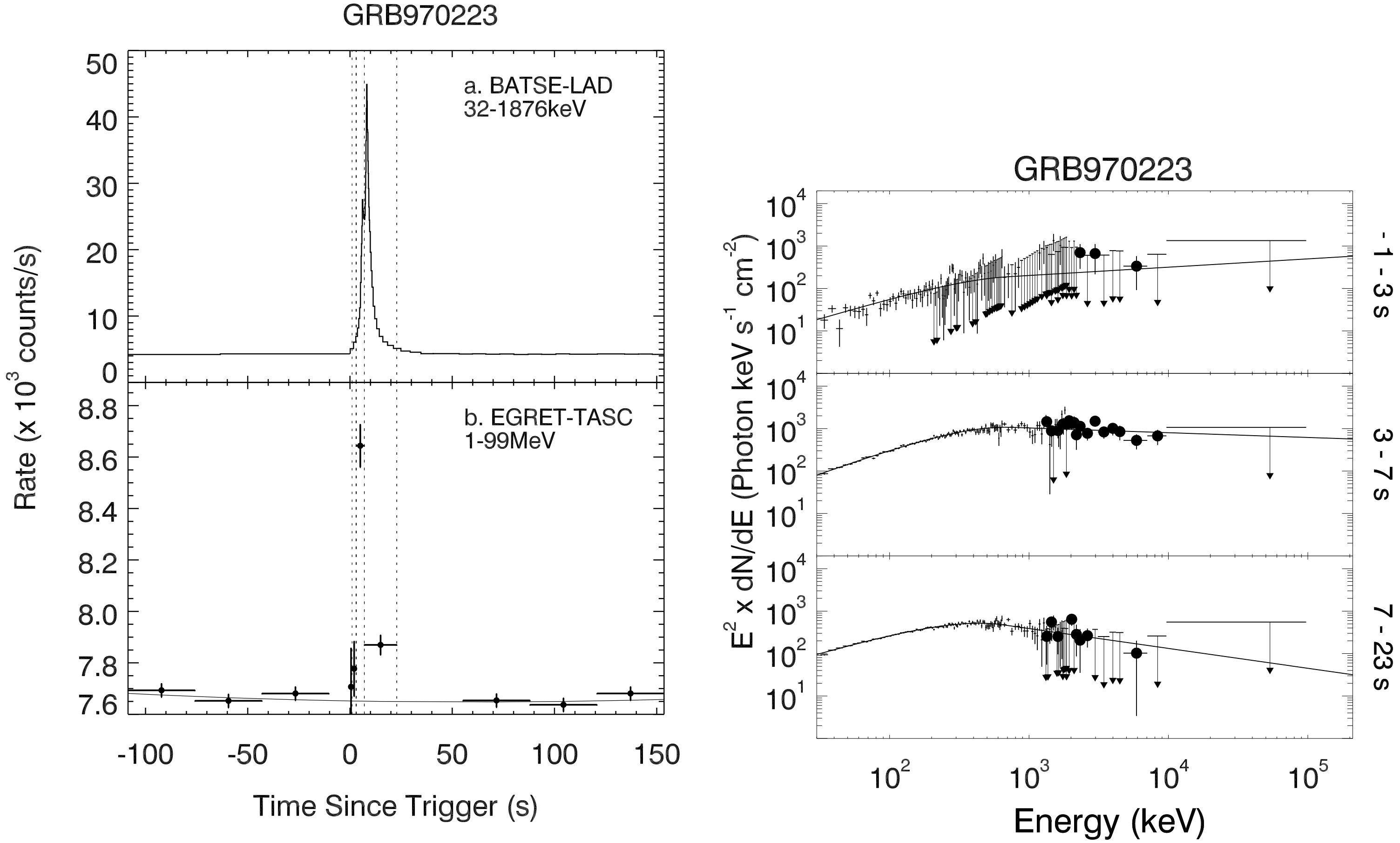

Figure 3.27: Counts rates and energy fluxes for GRB970315 are shown. Same as figure 3.16 but for GRB970315.

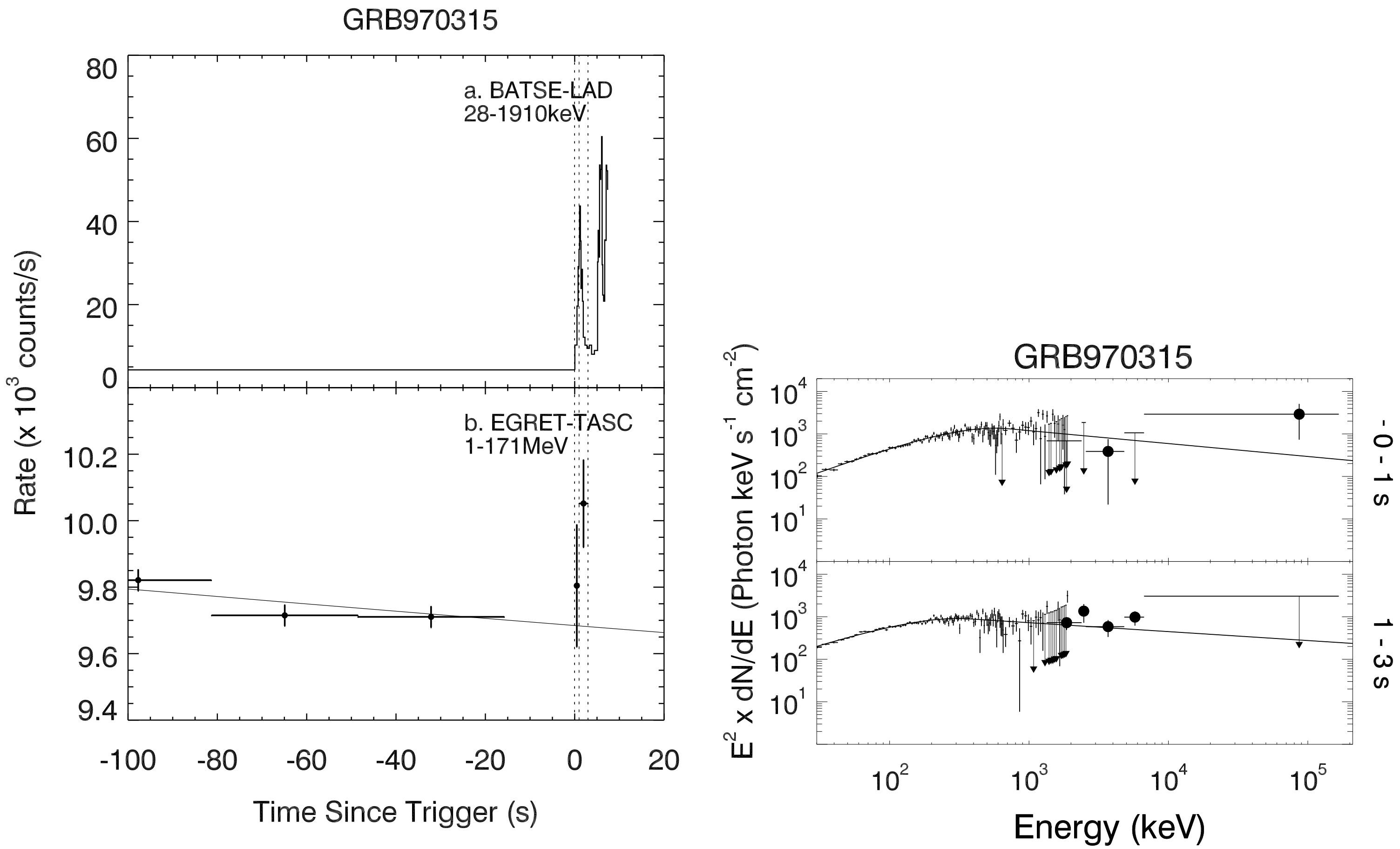

Figure 3.28: Counts rates and energy fluxes for GRB970411 are shown. Same as figure 3.16 but for GRB970411.

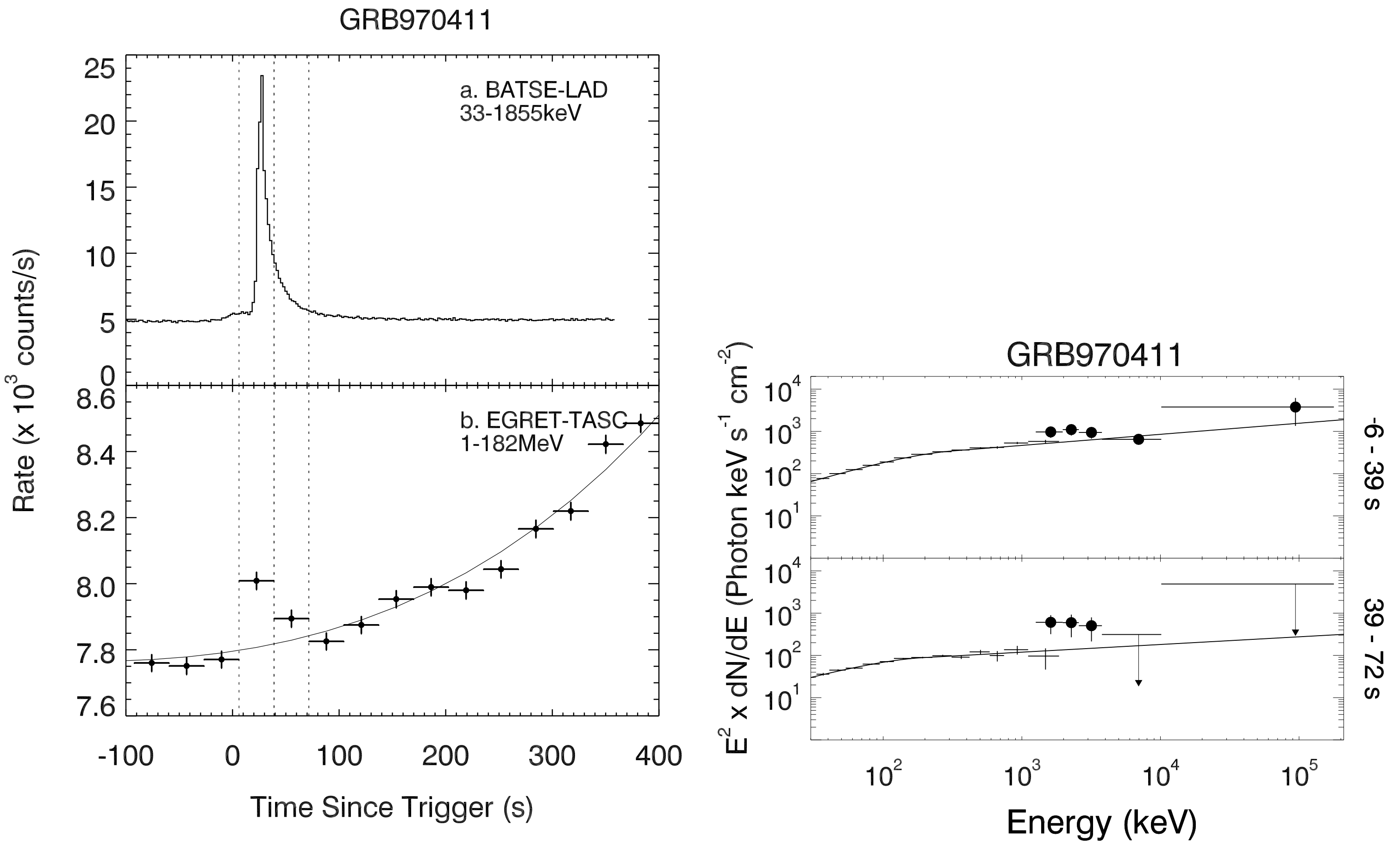

Figure 3.29: Counts rates and energy fluxes for GRB980923 are shown. Same as figure 3.16 but for GRB980923.

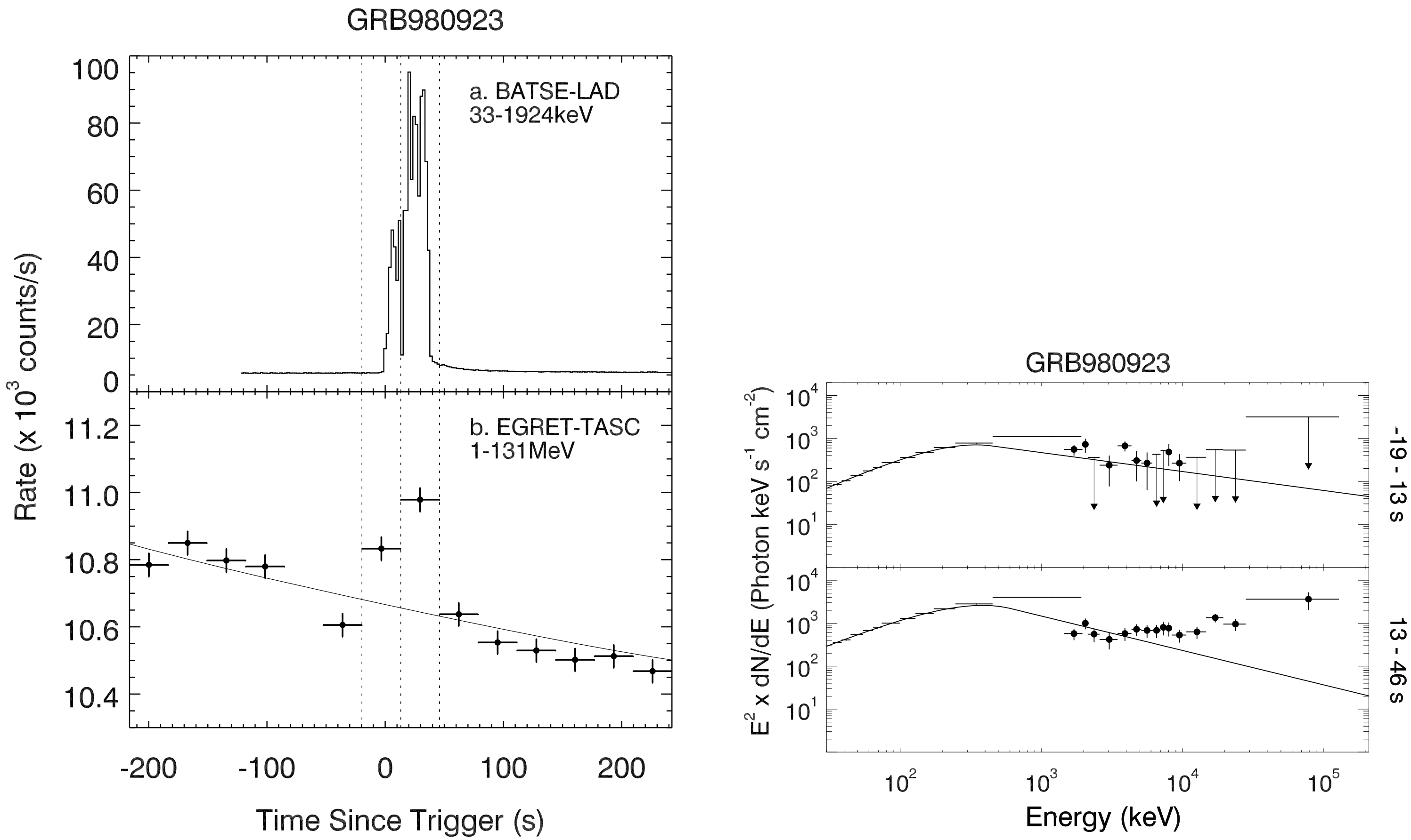

Figure 3.30: Counts rates and energy fluxes for GRB981021 are shown. Same as figure 3.16 but for GRB981021.

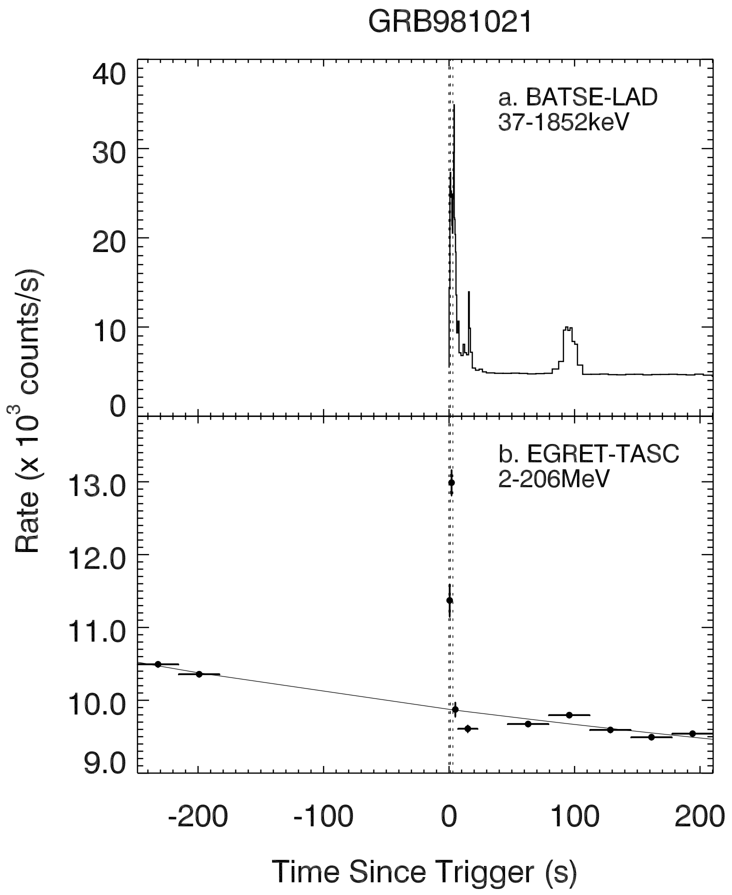

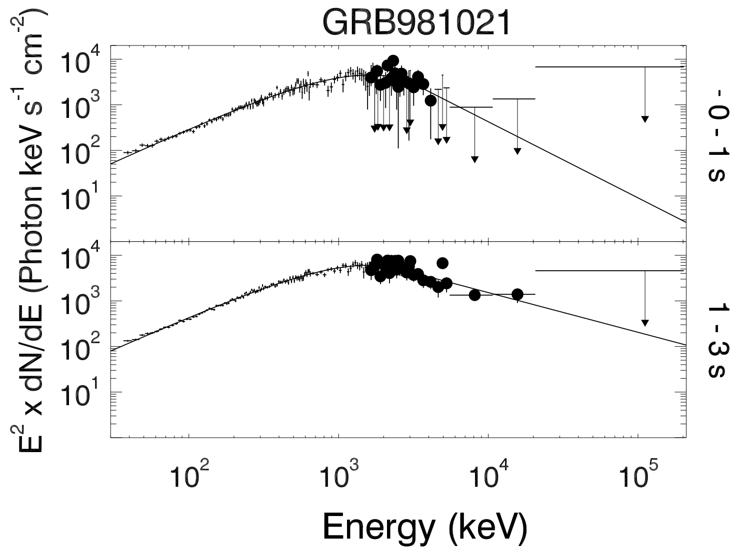

Figure 3.31: Counts rates and energy fluxes for GRB990104 are shown. Same as figure 3.16 but for GRB990104.

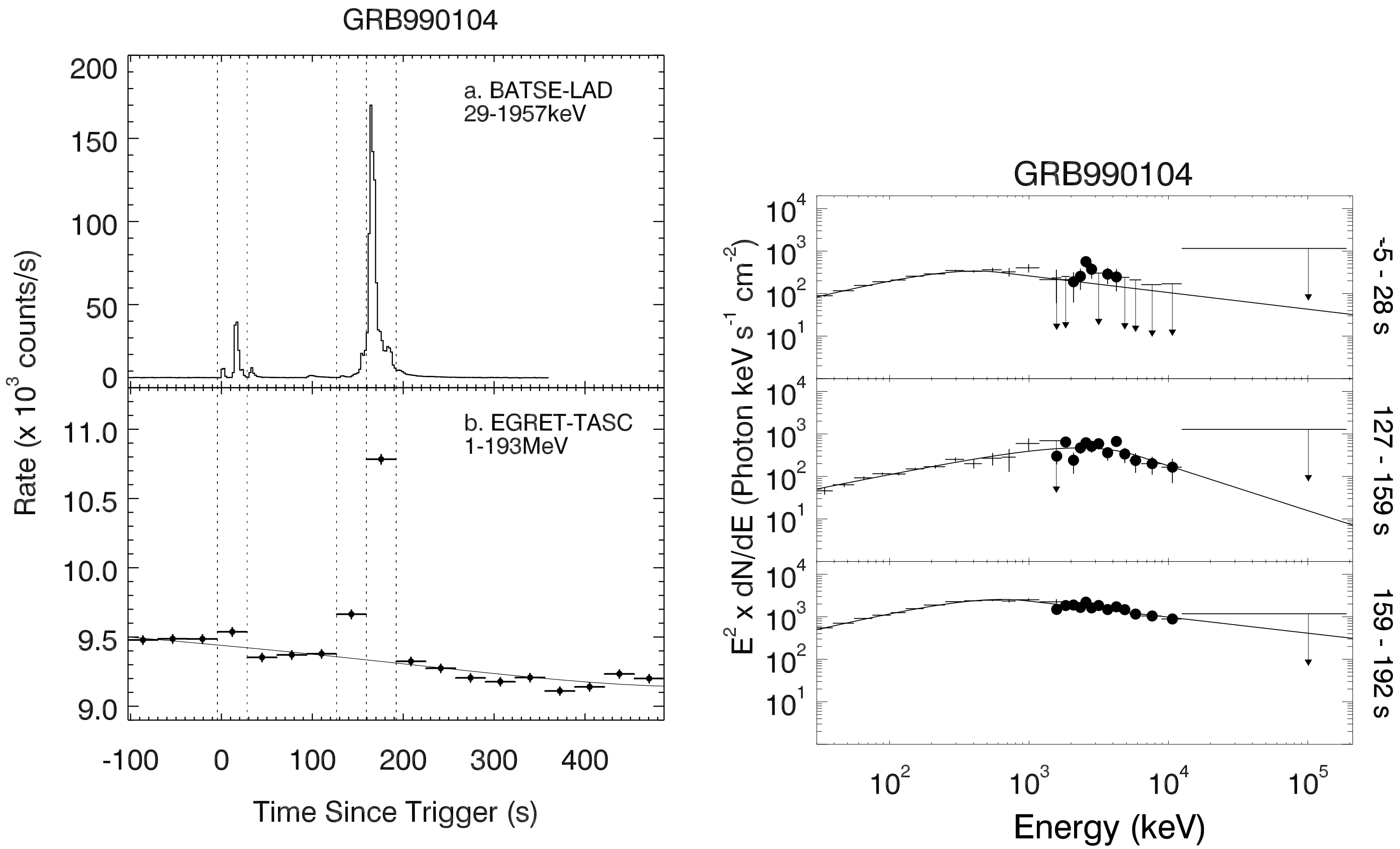

Figure 3.32: Counts rates and energy fluxes for GRB990123 are shown. Same as figure 3.16 but for GRB990123.

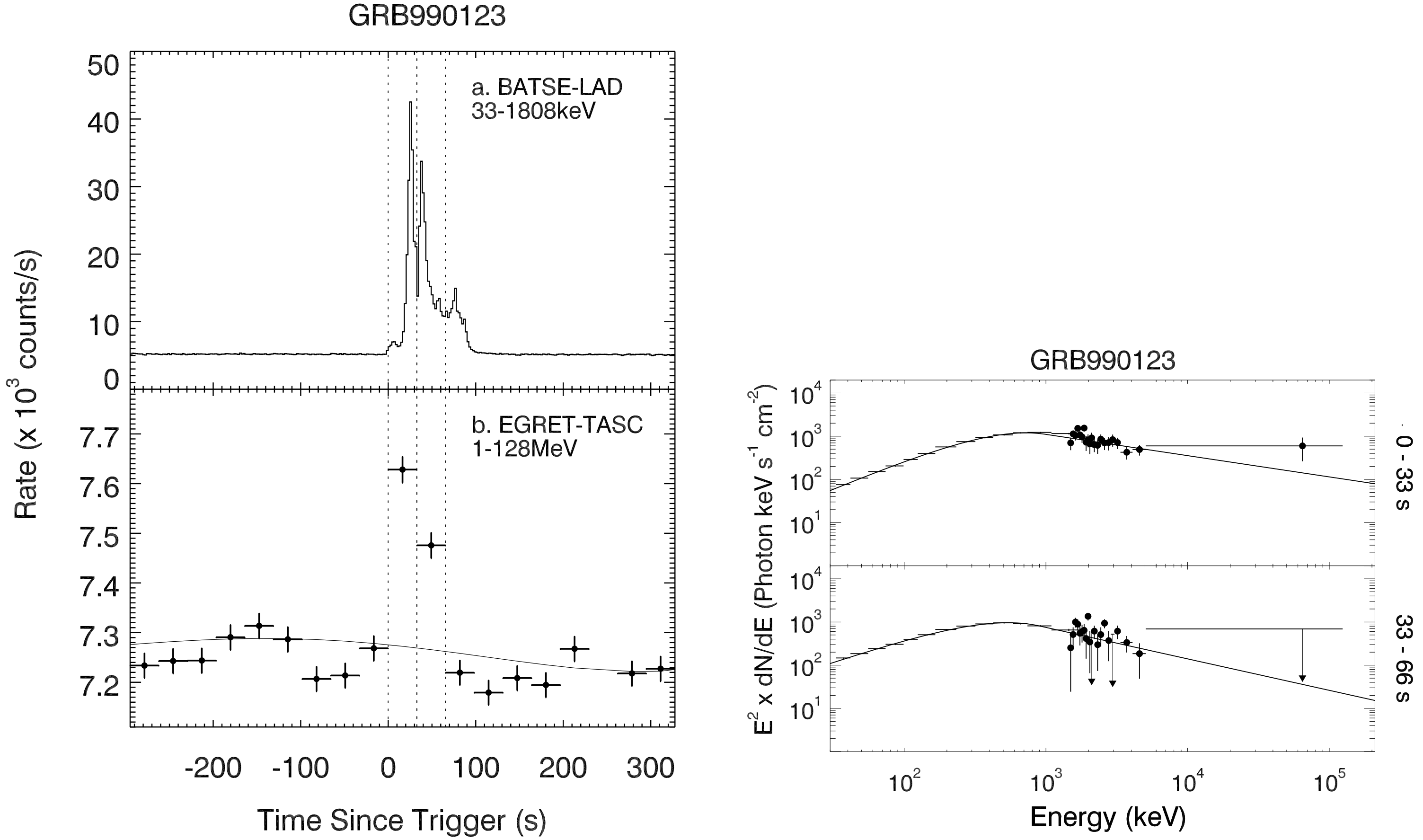

Figure 3.33: Counts rates and energy fluxes for GRB990506 are shown. Same as figure 3.16 but for GRB990506.

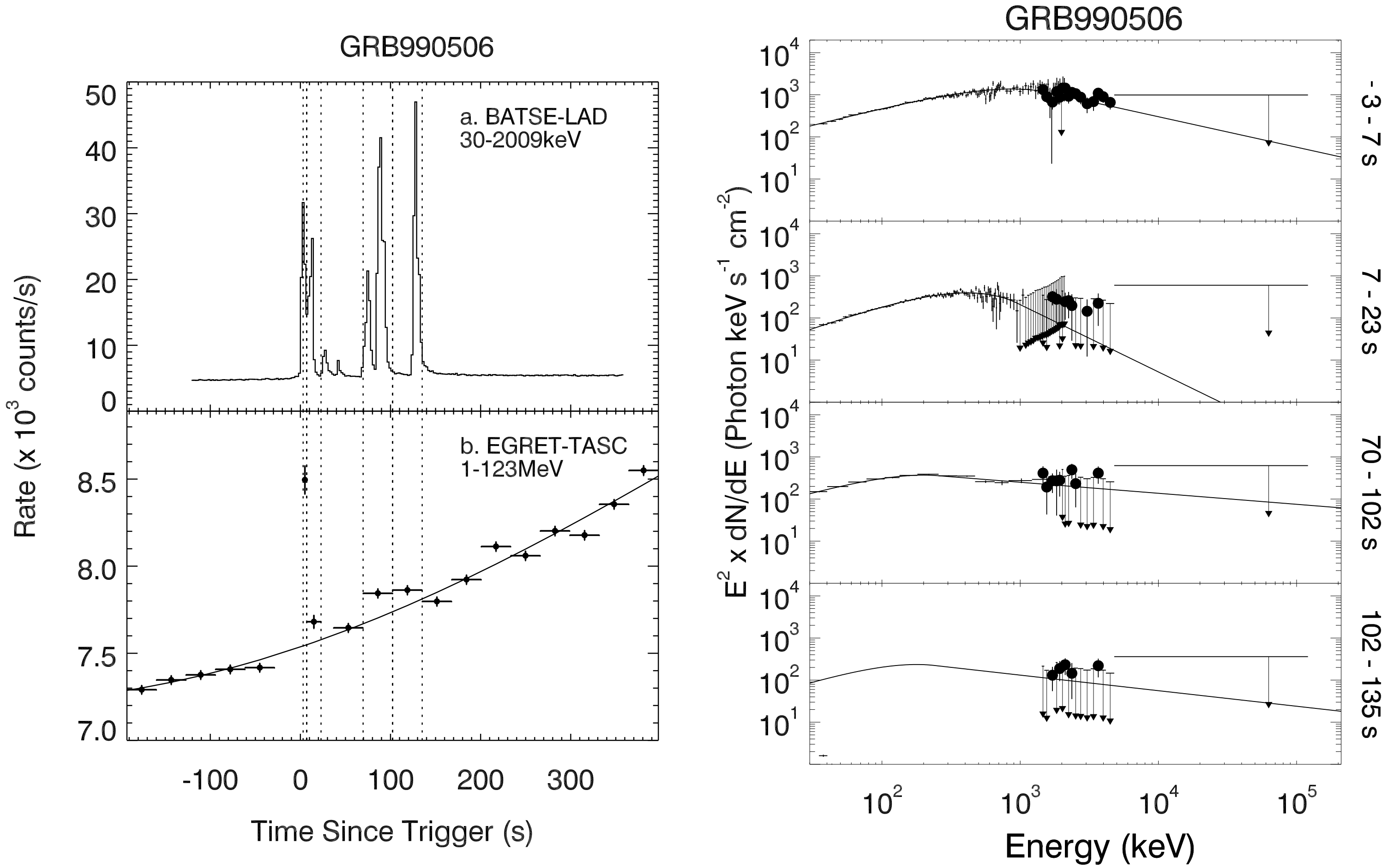

3.7 Global features

The global features mentioned below are based in the analysis of 14 bursts (GRB970202 and GRB981021 were excluded; GRB980923 and GRB941017 are discussed in later chapter). Bursts were required to be well described by the Band function. Also, the available TASC spectra for each burst had to cover most of the burst emission or at least most of one episode.

Results for the high energy spectral index and the peak energy obtained by analyzing combined BATSE-TASC data have been compared with that obtained by analyzing only BATSE data. Time resolved analysis of BATSE data for these bursts on TASC time intervals had not previously done. Therefore, they were obtained using the same software and methodology described in earlier sections. Results from BATSE and BATSE-TASC data are compared in figure 3.34. As expected, the high energy spectral index and the peak energy are better constrained by the combined BATSE-TASC analysis. The main impact is on those spectra with higher energy peaks. In general, the peak energy obtained with the combined analysis moves to higher energies than the obtained with only BATSE data. Also, the high energy spectral index gets softer than the obtained by only BATSE data.

A blind analysis of spectral temporal evolution without considering burst's morphologies could yield inconsistent conclusions. Therefore, in this analysis spectral temporal evolution within single episodes and spectral temporal evolution between different episodes is performed. For the 14 bursts considered in this analysis, the high energy emission came in a total of 32 episodes as observed by BATSE with 24 of them clearly mono-peaked and 8 multi-peaked (in GRB920311, GRB920622, GRB940217, GRB940703, GRB941017, GRB970315, GRB990123 and GRB990506). However, only 26/32 episodes yielded to a significant detection in TASC data, 12 of them covered by two or more TASC spectra. Also, there were only 5 bursts with more than one episode with significant detection.

As observed in table 3.3, the low energy spectral index gets a value that violates the line of death three times without considering GRB970202 and GRB981021, and seven times considering them. In all the seven times, TASC spectra mainly cover the raising period of a burst peak. Even though, this may suggest a correlation, its important to consider that there are spectra covering raising burst periods that do not violate the line of death, for example the spectrum in GRB940921. The violation of the line of death may rather be related to the increasing rate of the burst emission, but more statistics is needed for a conclusive result.

Twelve burst presented a single peak covered by more than one TASC spectra. Four peaks, the ones from GRB910503, GRB940921, GRB970411 and GRB990123, presented hard to soft temporal evolution in the peak energy and in the low and high energy spectral indices. The four peak of GRB920311, GRB920622, GRB970223 and GRB990506, presented hard to soft temporal evolution only in the high energy spectral index and the peak energy. One burst, GRB930506, had a peak with no evident temporal evolution in the high energy spectral index. Three peaks, GRB950425, GRB970315 and

GRB990104, had different temporal evolutions for the high energy spectral index and the peak energy. For instance, the high energy spectral index in GRB950425 changed from soft to hard while the peak energy changed from hard to soft. Therefore, approximately 2/3 of single peaks presented a hard to soft evolution in both the high energy spectral index and the peak energy.

GRB940217, GRB940703, GRB910503, GRB990104 and GRB990506 presented more than one peak in the light curves that were covered by TASC spectra with significant detection. There was not an evident temporal evolution from the parameters of one peak to a later one. Sometimes the value of the peak energy increases over the value of a preceding peak like in GRB910503. Sometimes the parameter increasing over peaks is the high energy spectral index, for example GRB990506. And sometimes, neither the high energy spectral index nor the peak energy increases over peak, as in GRB940703. Therefore, no evident unique or predominant temporal evolution over burst peaks was observed.

No correlation was observed between burst duration and any of the spectral indices or the peak energy. Even though, in single peaks the hard to soft temporal evolution of both, the high energy spectral index and the peak energy is observed, no correlation between these parameters was found. Many other correlations were searched without success, for example between the averaged values and the absolute changes of any parameter.

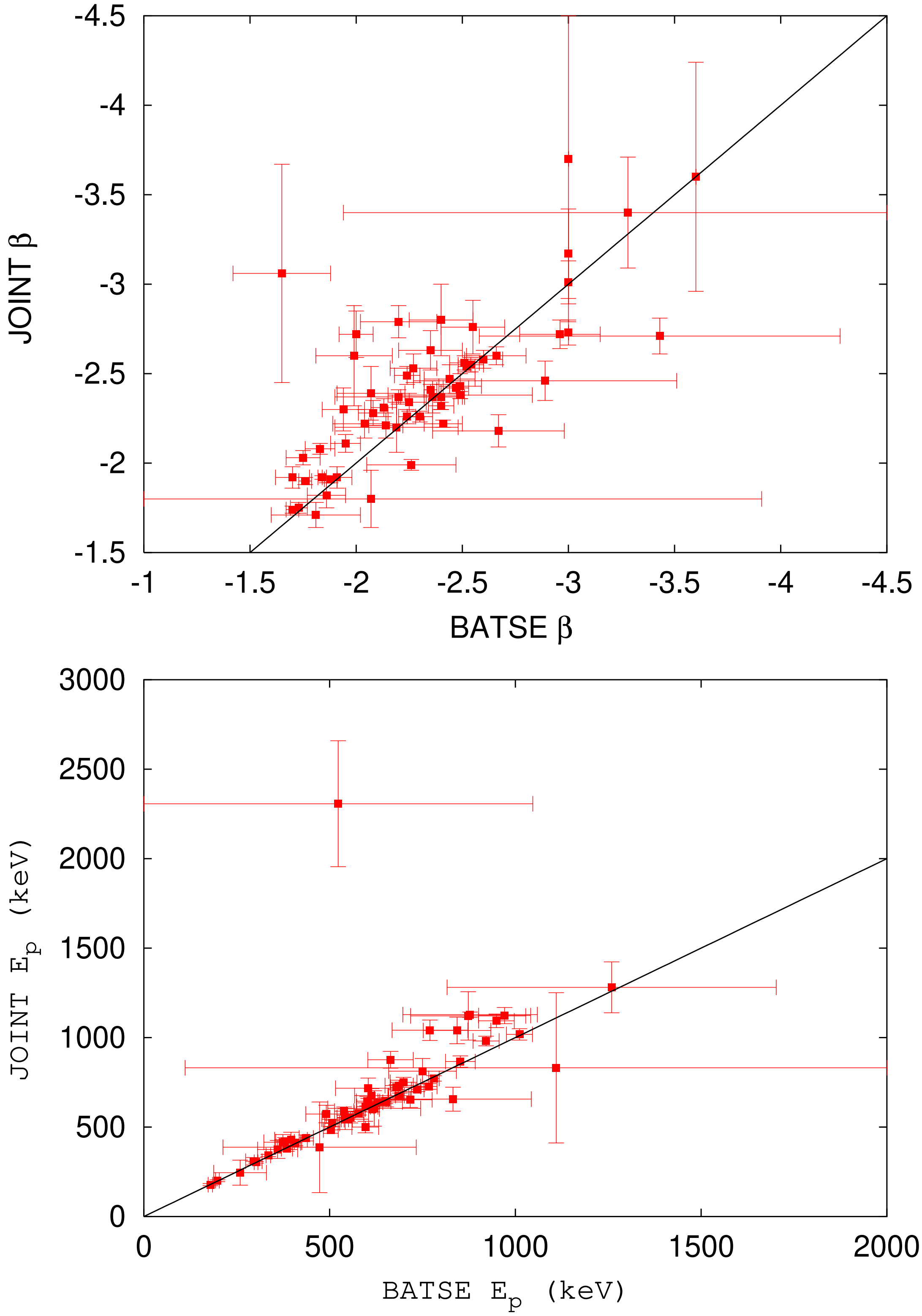

Figure 3.34: High energy spectral index (β) and peak energy (E_{peak}) as determined by BATSE and joint BATSE-TASC data.

3.8 Conclusions

TASC spectra for 18 bursts have been calibrated, corrected by deadtime and written in FITS format. Description and study of the temporal evolution of 50 GRB spectra has been performed using combined BATSE-TASC data. The peak energy and the high energy spectral index are better constrained by this analysis than using BATSE data alone.

Approximately 2/3 of the bursts showed hard to soft spectral temporal evolution in single episodes. No generalized temporal evolution through the whole burst or between episodes in a same burst was observed.

As discussed in section 1.4, the analysis of BATSE data show the Band function as the best photon flux model to describe the burst emission explained as synchrotron radiation. However, 10% of the BATSE bursts required another photon flux model such as the "Smooth Broken Power Law" or "Broken Power Law" because of peak energies close to the BATSE sensitivity. In this analysis, it was shown that the burst spectra associated with peaks at or below a few MeV can be totally described by a Band function. GRB941017 and GRB980923 are not exceptions as discussed in chapter 4.

It is shown that there is no cut off in the GRB spectra up to $\sim$ 10MeV and in some bursts up to $\sim$ 100MeV like in GRB930506, GRB941017 and GRB980923. Except for GRB941017 and GRB980923, the burst emission observed up to $\sim$ 10 MeV is consistent with being a smooth continuation of the emission at keV-energies which is likely due to synchrotron radiation. Additionally, some other bursts such as GRB920622 seem to have *more* emission above 10MeV than predicted by the model, but it is not as statistically significant mainly because of TASC sensitivity.

Most of the spectra of GRB941017 and GRB980923 are not described by a Band function because the emission above 10MeV is greater than predicted by the model. This excess can be explained as a second component in the spectra. The peak of this component does not seem to be below 100MeV. Further analysis is needed on these bursts and it will be done in chapter 4.

Chapter 4

Unexpected Higher-Energy Spectral Component

In chapter 3, data from BATSE and TASC were combined to characterize the prompt emission and its evolution in time for sixteen bursts in the energy range of 0.03-200MeV. Most of the analyzed spectra were well-described by the "Band function" up to 200MeV. This result is consistent with other high-energy observations such as [HU94, DI01]and [SH92]. This prompt emission at keV energies that is well-described by the "Band function" is "generally" explained as synchrotron radiation even though some details are not fully understood such as the violation of the "line of death" or the resulting electron energy distribution from the Fermi acceleration (details in section 1.2). The analysis of the temporal evolution GRB spectra helps to improve and constrain this or others models. By the other hand, observations inconsistent with the model's predictions may clarify our understanding or require new physics. In this sense, the spectra of GRB941017 and GRB980923 are of great interest because of the extra emission above 10MeV that needs to be understood.

Prompt GRB emission, other than the one associated with synchrotron radiation, is expected at much higher energies. For instance, synchrotron radiation may be Inverse Compton Scattered to energies higher than a few GeV, as explained in section 1.2.

There are a few observations at energies higher than 1MeV, all of them being consistent with a continuation of the emission observed at keV energies, except for the Milagrito observation [AT00]. The emission observed by Milagrito at ∼1TeV energies was more hot than the predicted. However, because of the lack of energy resolution, this observation exceeded an extrapolation of the Band fuction is not sufficient to undoubtedly identify the responsible radiation process. Fortunately, TASC data for GRB941017 and GRB980923 can give not only the energy distribution of the emission, but also the emission evolution along the burst for the observed excess above 10MeV.

In this chapter, the spectra of the strongest case, GRB941017, are considered. Then, GRB980923 is also analyzed for comparison with GRB941017. Data from TASC and EGRET's spark chambers are used to constrain the existence of the emission observed in GRB941017 and GRB980923 in other bursts. The results in this chapter have been partially published in [GO03b, GO04b].

4.1 GRB941017

BATSE observed GRB941017 at 10:19:33.938 UT for 77s (as determined by T90) from the galactic coordinates $l = 50.5°$ and $b = -11.7°$. The burst direction was 66° with respect to the pointing-axis direction of CGRO, reducing COMPTEL's effective area and placing the burst outside the ∼1sr field of view of the EGRET spark chamber.

BATSE spectra were analyzed by [PR98, PR00] an element of a set of bright bursts. A total energy fluence of 1.6×10^{-4} erg/cm^2 was estimated, placing this burst as the eleventh highest fluence one detected by BATSE. When a Band function was used to described the BATSE spectra [PR98], a hard-to-soft temporal evolution of the high energy spectral index, β, was observed. There were no observed spectral features different to the ones observed in most bursts in the energy interval of 0.03-2MeV in any of the time-resolved analyses. In particular, no excess of emission at higher energies at later times was reported.

The COMPTEL telescope-mode lightcurve is reported in [webComptel] for the energy range of 0.7-30MeV. Because of the observation's low significance, there is not published analysis of these data. However, the two COMPTEL's burst modules also observed this burst in the energy range of 0.3-10MeV. The analysis [KA05] of COMPTEL's burst module data have shown consistency with the results presented in this section and published in [GO03b, GO04b].

The TASC data have been previously analyzed [CA98] using a Power Law function to describe the time integrated spectrum of GRB941017. The spectral index reported in [CA98] is consistent with the one obtained with the analysis described in chapter 3. In the same reference, the maximum energy observed, either by TASC or the spark chambers, was given. GRB930506 was pointed out as an interesting case because the significance of TASC detection up to 135MeV. However, for GRB941017 the maximum energy observed was 10.9MeV indicating "no significant" emission above that energy in T90.

The "apparent" disagreement of previous analyses of BATE and TASC data with the spectra reported in chapter 3 for GRB941017 is consequence of the limitations of the analyses performed in [PR98, PR00, CA98]. GRB941017 is the best example of the advantages of time resolved spectral analysis of joint data.

BATSE-LAD and EGRET-TASC data are analyzed jointly for GRB941017. The analysis is fully described in chapter 3. Therefore, only relevant details to the analysis of GRB941017 data are mentioned in this section.

The lightcurves of the emission observed by LAD and TASC are shown in figure 4.1, left panel. The LAD data show a weak precursor ∼90s before the trigger. TASC detected seven 32.768s spectra starting 18s before the trigger. Each of the TASC spectra has more than 3σ excess over the background in the energy range of 1-200MeV. Both lightcurves are correlated, for instance, the highest time interval in TASC data corresponds to the BATSE lightcurve's peak. The BATSE flux in the time interval from 113-211s is still significantly detected with a 17σ excess over the background, while TASC flux is only 6σ excess above the background in both of the energy ranges shown in figure 4.1.

The TASC background was checked against the background 15 orbits earlier or later when the spacecraft was located at the same geomagnetic rigidity. In figure 4.1 the TASC count rates around GRB941017 trigger and 15 orbits earlier are shown. The background is fairly smooth in time and well described by a polynomial, therefore, the count excess in all seven TASC spectra are related to GRB941017.

The last 3 time intervals for the TASC and LAD were combined in a single bin.

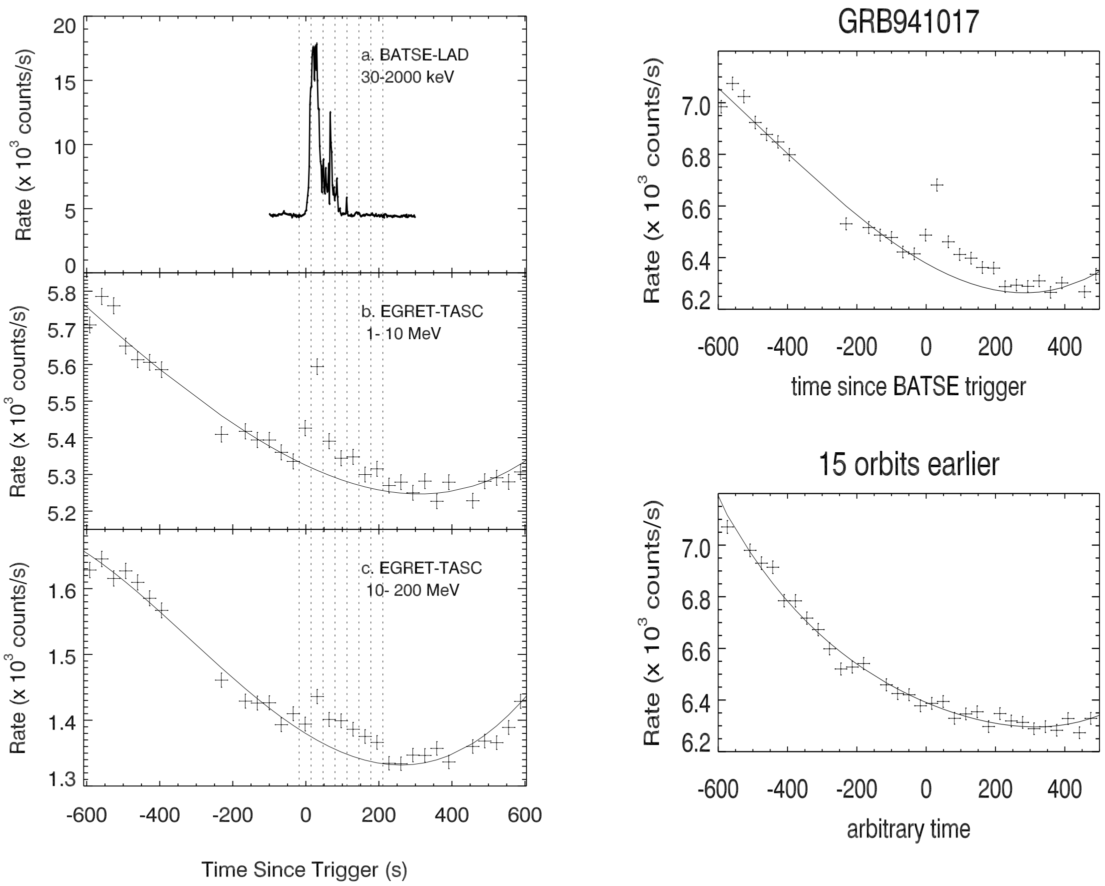

Figure 4.1: Counts rates for GRB941017. The BATSE lightcurve is shown in the top-left window labeled as a. The TASC lighcurves are shown in the middle-left and bottom-left windows labeled as b and c for the energy ranges of 0.03-2, 2-10 and 10-200MeV respectively; and for the whole TASC energy range (1-200MeV) in the top-right window. For comparison, the TASC count rates for 15 orbits earlier to GRB941017 are shown in bottom-right window. When TASC data is plotted, the solid line corresponds to the 4th order polynomial that best fits the background.

The data was analyzed using the Band function plus a power law function described by $A_{PL}[E(keV)/30MeV]^{\gamma}$ that was required to fit the higher energy γ-ray excess at later times. A normalization factor of 0.45 was applied to TASC data to account for the errors in the calculated effective area that was shown to be needed even in the pre-flight calibration [TH93]. The data and spectral fits for the five time intervals are shown in figure 4.2 with the best fit parameters given in Table 4.1.

In the first time interval, LAD-TASC data could be mainly described by the Band function, while in the last time interval the higher-energy power law describes most of the data. Thus, both spectral components, the Band function at lower energies and the higher-energy power law, are observed by both detectors. In the second time interval, TASC data below 10MeV smoothly continues the lower-energy component described by the Band function, showing the correct energy dependence and normalization factor.

As observed in figure 4.2, the lower-energy component evolves with time while the higher-energy component remains fairly constant. Figure 4.3 shows the hard-to-soft evolution of the Band parameters α and β. E_{peak} moves to lower energies while the amplitude of the lower-energy component decreases. This is the generalized evolution observed in other bursts [PR00, GO04]. The higher-energy component stays bright and the spectral index does not change within the statistical uncertainties. The energy fluxes for three different energy ranges are also shown in figure 4.4 for each time interval. The temporal fit of the energy fluxes (F) in the last four time intervals when described by $F = At^{\phi}$, yields ϕ=2.8,1.45 and 0.2 for the energy ranges of 0.03-2,2-10 and 10-200MeV, respectively, showing that the higher-energy component decays much slower than the lower-energy component. The additional higher-energy component results in a total >30keV fluence greater than 6.5×10^{-4}erg/cm^2, since it peaks above 200MeV. This total >30keV fluence is more than three times the estimated from the BATSE energy alone and it places GRB941017 within the first 3 brightest bursts observed by BATSE. A 1σ upper limit for the energy flux of the higher-energy component was calculated for the time interval of 210-309s. A value of 0.26×10^{-6} was obtained, see Figure 4.4.

The higher-energy component started within the first 14s of the burst since its detection beyond 14s reached a significance of 3σ. On the other hand, the background subtracted count rates above 10MeV were approximately 41, 36 and 31 $\times10^3$counts/sec for the three spectra in the time period of 113-211s, varying only 25%, see Figure 4.1 bottom panel. In contrast, the background subtracted count rate for the following spectrum (211-243s) was only 2 $\times10^3$counts/sec, implying a sharp decay of the higher-energy component around 211s, see Figure 4.1 bottom panel. The total sub-MeV duration of the emission from GRB941017 given in [webBATSEid3245] is $\sim$280s, starting $\sim$100s before BATSE trigger. Thus, the burst's tail ended around $\sim$180s. Since TASC temporal resolution was 32.77s, the difference in ending times of the burst tail and the higher-energy component could imply they are coincident.

It is clear from this analysis that the maximum energy detected by TASC is not 10.9MeV as reported in [CA98], not even in T90. In this case, the time-average spectrum increases the background and not the signal at the highest energies since the second component starts to be significant after 14s, see figure 4.1. Therefore, the significance of the detection at the highest energies decreases. The problem is solved with a time-resolved analysis.

The duration of GRB941017, as defined by T90, is dominated by the brightest part of the burst in the BATSE's energy range. Therefore, the long dim but energetic tail of GRB941017 was ignored by [CA98] by implying that the emission above 1MeV lasted T90. Also, a description of the TASC data by a single power law would yield incorrect conclusions. Compare 3.23 right panel with 4.2, for the time interval from 14s to 47s where previous knowledge of the spectra behavior at keV energies could avoid this mistake. Analysis of joint data solved the problem.

A higher-energy component separated from the lower-energy component usually described as a Band function was clearly detected. This higher-energy component is described by a power law with differential photon index ~ -1 up to 200MeV. This higher-energy component decays more slowly than the lower-energy component and its fluence is at least twice the fluence of the lower-energy component.

Time from BATSE trigger (s)	**-18 to 14**	**14 to 47**	**47 to 80**	**80 to 113**	**113 to 211**
Band GRB function parameters					
A($\frac{\times 10^{-2}\text{ph}}{\text{s cm}^{-2}\text{keV}}$)	1 ± 0.05	6 ± 0.1	2 ± 0.1	0.7 ± 0.3	5^{+4}_{-2}
E_{peak}(keV)	505 ± 69	350 ± 8	240 ± 14	91 ± 15	10 fixed
α	-0.84 ± 0.09	-0.79 ± 0.02	-1.08 ± 0.06	-1.45 ± 0.27	-1 fixed
β	-2.22 ± 0.13	-2.46 ± 0.05	$-2.65^{+0.22}_{-0.85}$	$-3.13^{+0.63}_{-\infty}$	-2.73 ± 0.55
High-energy power law parameters					
A$_{PL}$($\frac{\times 10^{-7}\text{ph}}{\text{s cm}^{-2}\text{keV}}$)	NA	2.4 ± 0.6	2.4 ± 1.0	3.2 ± 0.7	1.8 ± 0.5
γ	NA	-1 fixed	$-1.06^{+0.70}_{-0.44}$	$-1.10^{+0.32}_{-0.17}$	$-0.96^{+0.36}_{-0.17}$
Probability	NA	1.4×10^{-4}	3.7×10^{-4}	6.5×10^{-8}	1.4×10^{-7}
Energy Flux ($\times 10^{-6} \frac{\text{erg}}{\text{s cm}^{-2}}$)					
0.03-2 MeV	0.85 ± 0.02	3.52 ± 0.46	0.96 ± 0.19	0.20 ± 0.02	0.03 ± 0.004
2-10 MeV	0.33 ± 0.008	0.82 ± 0.11	0.20 ± 0.04	0.15 ± 0.01	0.07 ± 0.007
10-200 MeV	0.38 ± 0.009	2.63 ± 0.35	2.03 ± 0.40	2.54 ± 0.25	1.67 ± 0.18

Table 4.1: Spectral fitting parameters of the differential photon flux. The first six rows contain the best spectral fit parameters for the five time intervals shown in Figure 4.2. The seventh row shows the probability that the improvement in χ^2 from the addition of the high-energy power law in the fit is due to chance, as determined by the χ^2 test. The last three rows contain the energy fluxes for three different energy ranges.

4.2 GRB980923

BATSE observed GRB980923 at 20:10:52 for 33.02s (as determined by T90) from the galactic coordinates $l = 293.08°$ and $b = -30.89°$. The burst direction was 124.4° with respect to the pointing-axis direction of CGRO, placing the burst outside the ∼1sr field of view of COMPTEL and the EGRET spark chamber.

BATSE spectra were analyzed by [PR00]. A total energy fluence of 4.5×10^{-4} erg/cm^2 was estimated, placing this burst as the third highest fluence one. Similarly to GRB941017, GRB980923 had a long and smooth tail observed [webBATSEid7114] by BATSE that lasted up to 120s. In the reference [GI99] the duration of the tail is reported to be ∼400s. This tail has been specifically studied by [GI99] using BATSE data. An abrupt change in the spectral shape was observed when the tail became noticeable arguing the existence of a separate emission component correlated with the tail.

TASC data for GRB980923 consist of only two spectra covering almost twice the burst duration (as defined by T90). Only the second spectrum covering from 13s to 46s was inconsistent with a continuation of the emission at keV energies, see figure 3.29. Thus, the temporal behavior of the emission above 10MeV can not be determined as for GRB941017. However, the constant differential photon index observed in the higher-energy component of GRB941017 can be tested by GRB980923. BATSE-LAD and EGRET-TASC data are analyzed jointly for the second spectrum of GRB980923. The first spectrum was analyzed in the previous chapter and the results are included

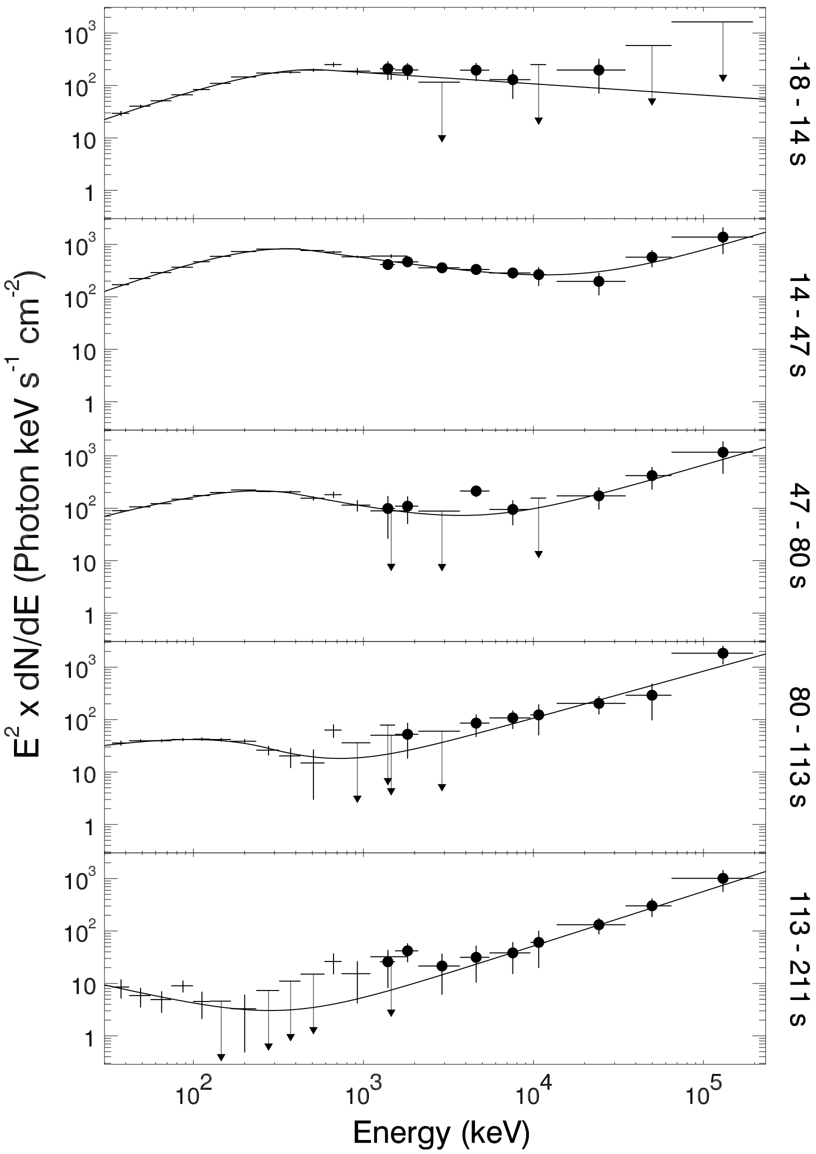

Figure 4.2: Energy fluxes for GRB941017, during the time intervals shown in Table 4.1. Crosses and circles correspond to BATSE-LAD and EGRET-TASC data respectively. For the purpose of the plot, but not for the spectral fit, the TASC data are binned in energy to give at least 2σ significance over the background. The upper limits correspond to 2σ deviation from the background. The solid lines represents the best fit to the joint LAD-TASC data using a Band function. The best fit parameters are shown in Table 4.1. The normalization factor between the data sets was fixed to 0.45 through the whole burst.

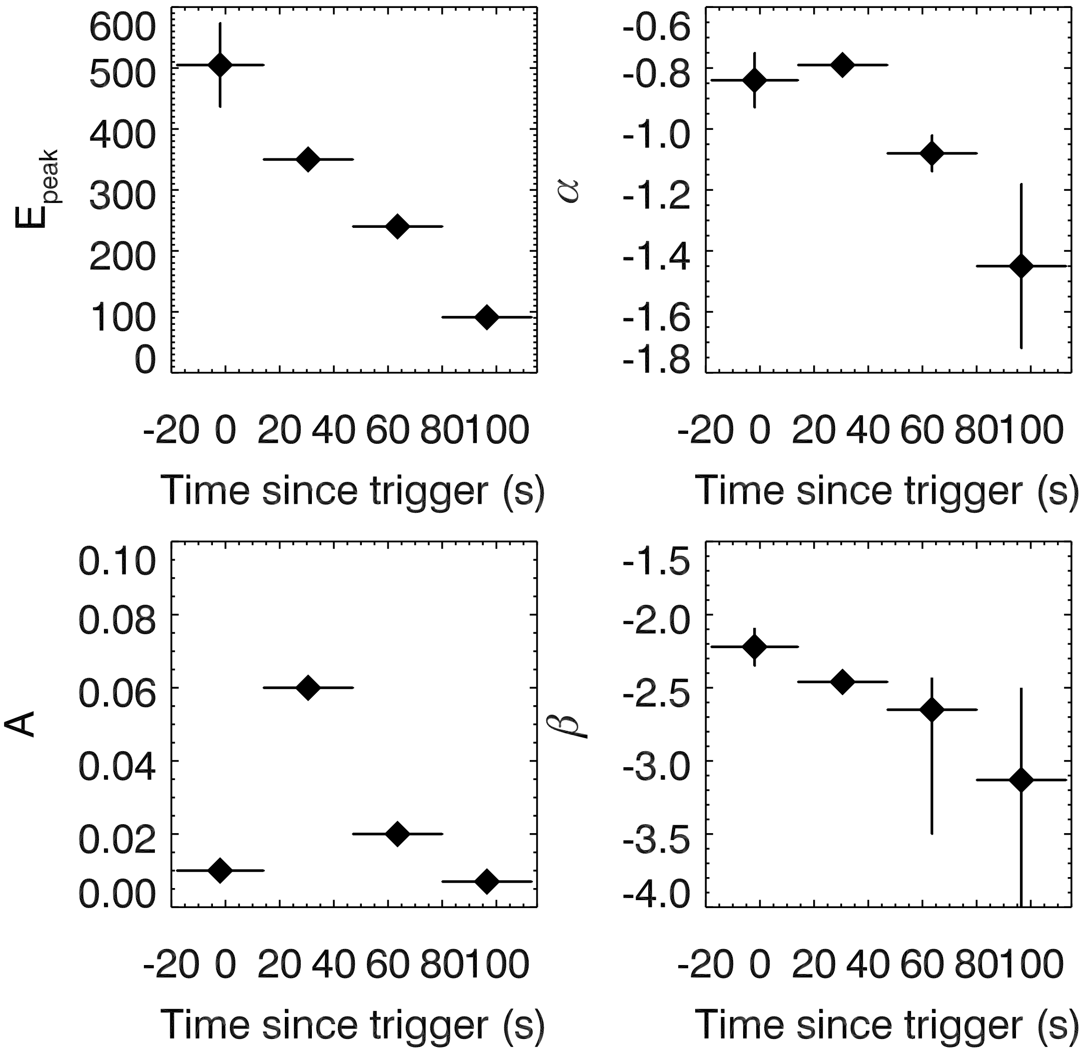

Figure 4.3: The Band's parameters that best fit the spectra below 1MeV as function of time. A typical hard to soft evolution is observed.

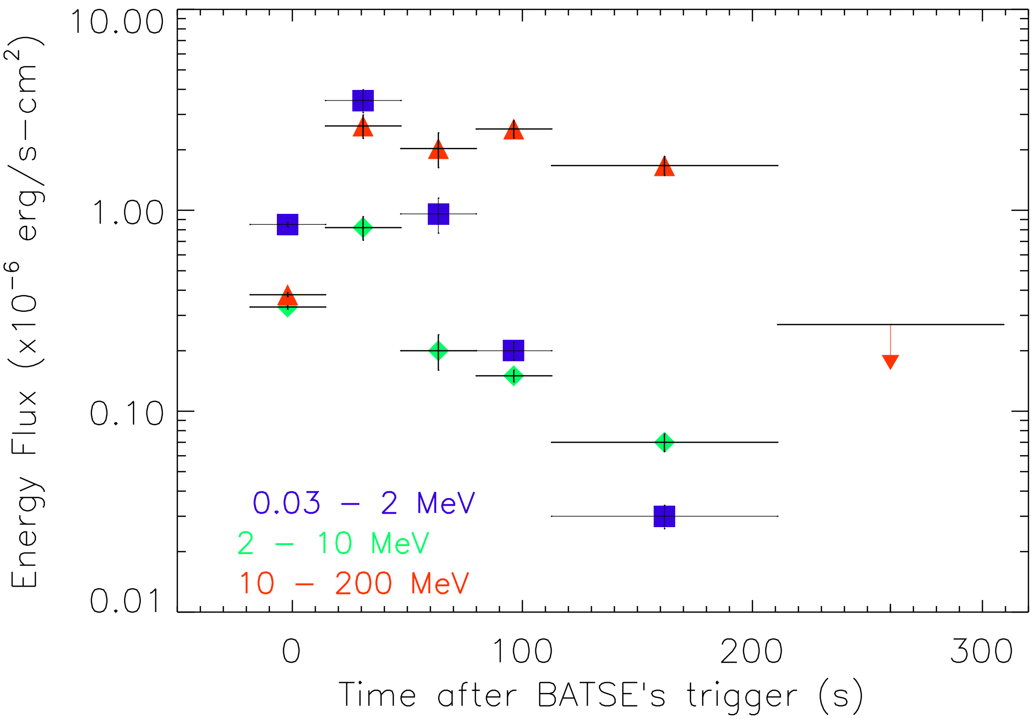

Figure 4.4: Time evolution of the energy fluxes observed in GRB941017 is shown for the energy ranges of 0.03-2MeV(square), 2-10MeV(diamond) and 10-200MeV(triangle). The energy flux at higher energies decays much slower than the energy flux of the sub-MeV emission.

in this section only for comparison. The analysis is fully described in chapter 3. Only relevant details to the analysis of GRB980923 data are mentioned in this section.

The lightcurves of the emission observed by LAD and TASC are shown in figure 4.5. TASC detected two 32.768s spectra starting -19s before the trigger. The TASC spectra have 5.9σ and 10.5σ excess over the background in the energy range of 1-200MeV respectively. As in GRB941017, TASC data are shown for below and above 10MeV, see figure 4.5. The second TASC spectrum has an excess over the background of 8.6σ and 6.9σ in the energy ranges shown in 4.5 respectively. BATSE and TASC lightcurves have the same behavior up to 46s. The tail observed by BATSE beyond 46s was not detected in the TASC energies. Figure 4.5 also shows the background model used and checked against the background of 15 orbits later.

The second TASC spectrum was analyzed using the Band function plus the power law function described by $A_{PL}[E(keV)/30MeV]^{\gamma}$, as was used for GRB941017. A normalization factor of 0.32 was applied to TASC data. The data and spectral fits for the two time intervals are shown in figure 4.6 with the best fit parameters given in Table 4.2.

In the first time interval, LAD-TASC data is sufficiently described by the Band function, while in the second time interval both functions, the higher-energy power law and the Band function are required to describe the data. Only the Band function is observed by both detectors in both time intervals. In the second time interval, TASC data below 10MeV smoothly continues the lower-energy component described by the

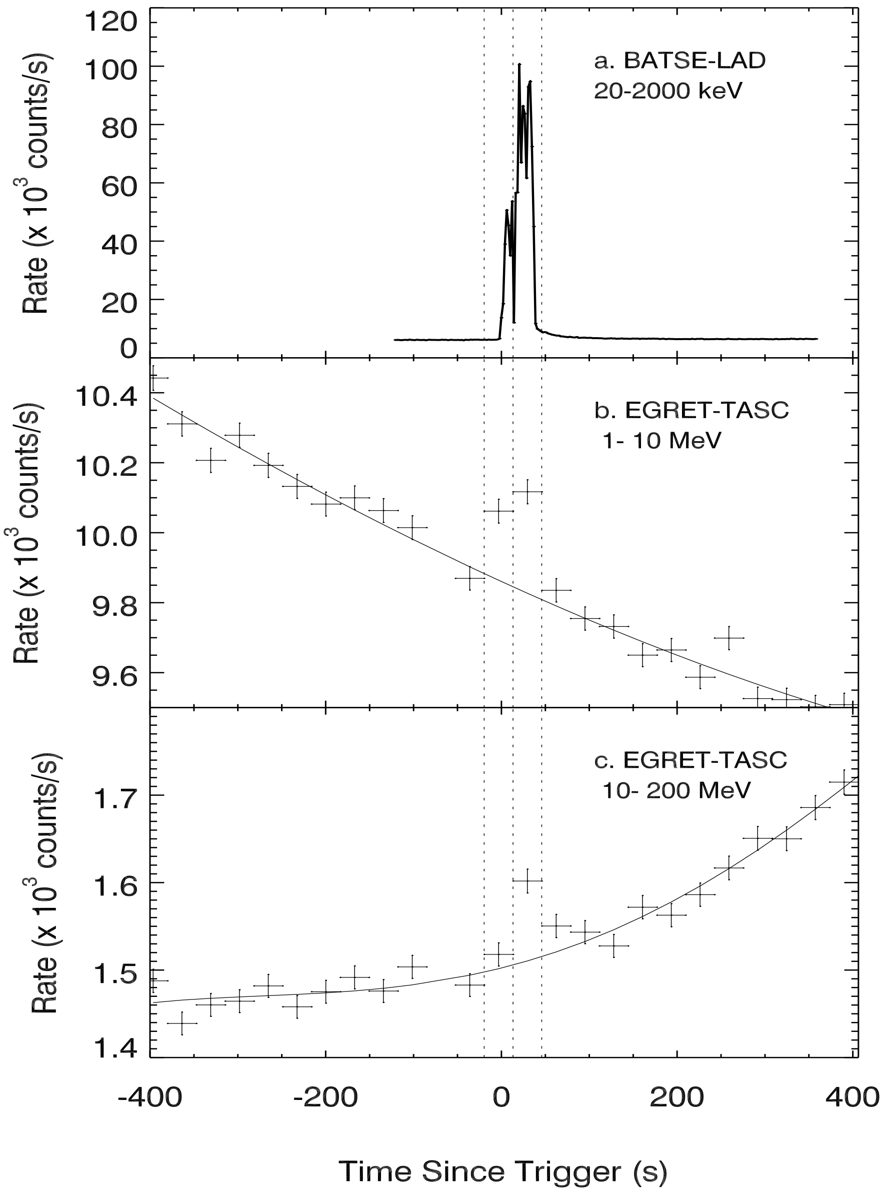

Figure 4.5: Counts rates for GRB980923. The BATSE lightcurve are shown in the top window labeled as a. The TASC lighcurves are shown in the middle and bottom windows labeled as b and c for the energy ranges of 0.03-2, 2-10 and 10-200MeV respectively; and for the whole TASC energy range (1-200MeV) in figure 3.29, left bottom window. When TASC data is plotted, the solid line corresponds to the 4th order polynomial that best fits the background.

Time from BATSE trigger (s)	**13 to 46**	**13 to 46**	**13 to 46**
Band GRB function parameters			
A($\frac{\times 10^{-2}\text{ph}}{\text{s cm}^{-2}\text{keV}}$)	16.2 ± 0.1	15.9 ± 0.2	16.0 ± 0.1
E_{peak}(keV)	388 ± 4	397 ± 4	397 ± 4
α	-0.66 ± 0.01	-0.67 ± 0.01	-0.67 ± 0.01
β	-2.93 ± 0.06	-3.51 ± 0.25	-3.31 ± 0.12
High-energy power law parameters			
A$_{PL}$($\frac{\times 10^{-7}\text{ph}}{\text{s cm}^{-2}\text{keV}}$)	—	5.6 ± 0.7	4.9 ± 0.7
γ	—	-1.32 ± 0.25	$-1 fixed$
Probability	—	1.1×10^{-6}	3.4×10^{-7}
Energy Flux ($\times 10^{-6} \frac{\text{erg}}{\text{s cm}^{-2}}$)			
0.03-2 MeV	11.1 ± 0.03	10.9 ± 0.7	10.9 ± 0.7
2-10 MeV	1.0 ± 0.003	0.8 ± 0.05	0.8 ± 0.05
10-200 MeV	0.26 ± 0.0008	2.7 ± 0.2	2.9 ± 0.2

Table 4.2: Spectral fitting parameters of the differential photon flux. The first six rows contain the best spectral fit parameters for the two time intervals shown in Figure 4.6. The seventh row shows the probability that the improvement in χ^2 from the addition of the high-energy power law in the fit is due to chance, as determined by the χ^2 test. The last three rows contain the energy fluxes for three different energy ranges. In last column, a higher-energy component similar to the one observed in GRB941017 with spectral index -1 is assumed.

Band function, showing the correct energy dependence and normalization factor.

The best high-energy power law that fits the data above 10MeV has a spectral index consistent with the constant value of -1 found in GRB941017. Its amplitude approximately twice the amplitude of the one in GRB941017. The probability that the improvement in χ^2 from addition of the high-energy power law in the fit is due to chance, as determined by the F-test, is 1.2×10^{-6}. Although, this probability is two orders of magnitude above the lowest probability of GRB941017, it is better than expected when compared with GRB941017 because the Band part is much brighter and peaks at higher energy than in GRB941017. Fortunately, the Band's high-energy spectral index was soft enough to uncover the higher-energy component. The energy fluence from the higher-energy component is only about 10% of the total energy fluence, even though the higher-energy component is brighter than the one observed in GRB941017.

GRB941017 and GRB980923 had a single episode lasting less than 80s, a long tail and are within the brightest bursts. In other hand, GRB941017 had a multi-peak single episode and "Band component" evolving slowly with time from hard-to-soft and; GRB980923 had a smooth single episode and a fast decaying "Band component" without a clear temporal evolution. Besides that, both had a higher-energy component described by a power law function of index -1 releasing an energy flux of $\sim 2.3\times10^{-6} erg - s^{-1} - cm^{-2}$ in the energy range of 10-200MeV. For completeness, a second fit to the joint data was performed assuming a spectral index of -1 for the higher-energy component. The results are given in Table 4.2 and shown in figure 4.6.

Now that the existence of the higher-energy component in GRB980923 is known, it is possible to understand the results reported by [GI99]. First, a spectral fit to the tail of GRB980923 was done with the same assumptions made by [GI99] (only BATSE data). Same results were obtained. Secondly, BATSE spectra were combined to match TASC time intervals. Three TASC spectra (79-177s) were combined to increase statistics. Then, TASC spectra for the time intervals 46-79s and 79-177s were fitted with the same assumptions made by [GI99]. The best fits are shown in 4.7 together with the fits for previous spectra.

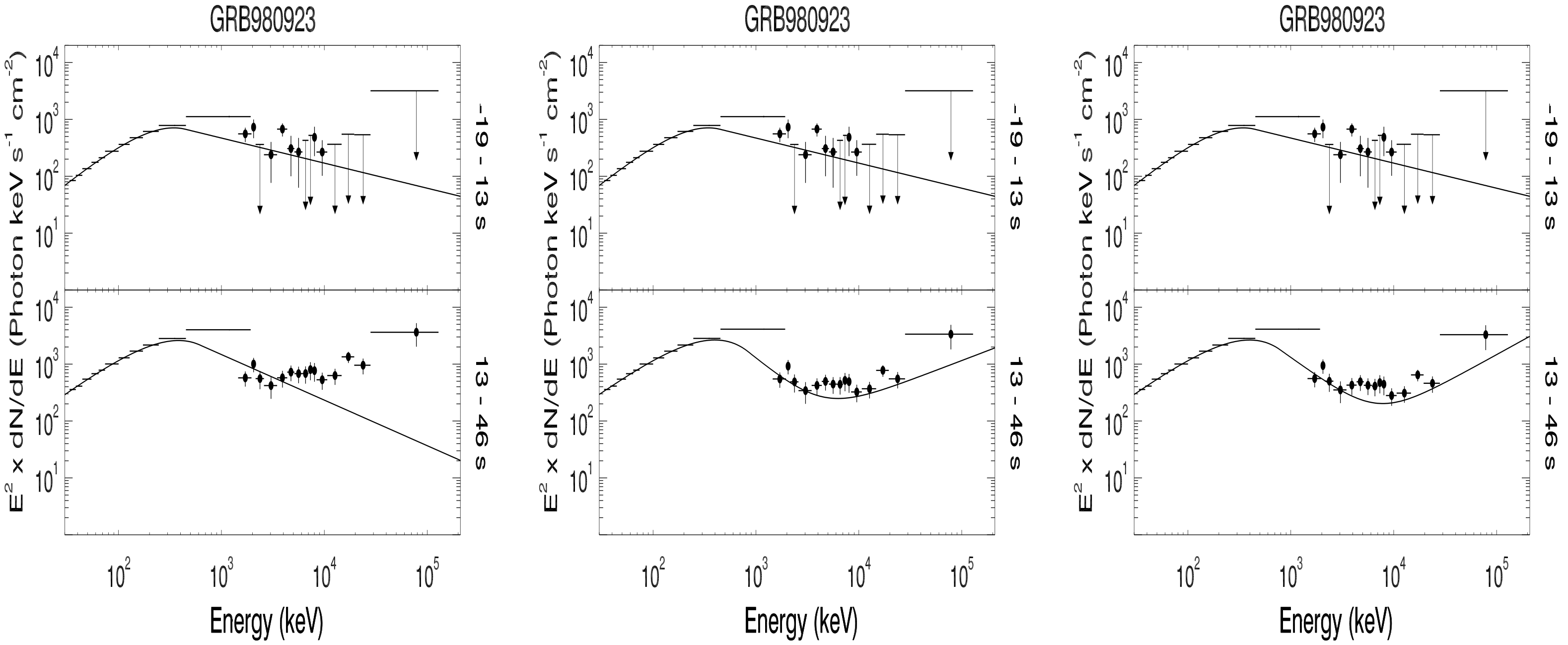

Figure 4.6: Energy fluxes for GRB980923, during the time intervals shown in Table 4.2. Crosses and circles correspond to BATSE-LAD and EGRET-TASC data respectively. For the purpose of the plot, but not for the spectral fit, the TASC data are binned in energy to give at least 2σ significance over the background. The upper limits correspond to 2σ deviation from the background. The solid lines represents the best fit to the joint LAD-TASC data using a Band function. The best fit parameters are shown in Table 4.2. The normalization factor between the data sets was fixed to 0.32 through the whole burst. A higher-energy component similar to the one observed in GRB941017 with spectral index -1 is assumed in two right windows.

The lower-energy component in the first 46s is described by a Band function. The low-energy spectral index and the peak energy remain fairly constant while the high-energy spectral index softens. Around 46s, the lower-energy component decays rapidly. For instance, the energy flux at 400keV decreases almost 3 orders of magnitude from the second to the third time interval shown in Fig 4.7. There is not a clear temporal evolution of the lower-energy component. The higher energy component dimmed below TASC sensitivity after 46s and it did not yield a significant detection in TASC energies. However,this high energy component did not decay abruptly because when the lower-energy component decreases below 100 $\mathrm{ph-keV/s-cm^2}$, it became apparent in BATSE data (last spectra). It was also likely present in BATSE data in the time interval between the two large peaks in the light curve at $t \sim$ 15s as indicated by the similar spectrum with $\alpha \sim -1.5$ reported by [GI99]. This is not an unexpected result for a higher-component like that observed in GRB941017, as seen in the last spectrum in 4.2. Therefore, the change in the spectral component observed by [GI99] when the tail became noticeable ($\sim 40s$) is because the contributions to the spectrum of the lower and higher energy components, are comparable. It resulted in a harder Band's high-energy spectral index. Therefore, there was not a separate emission component described by a Band function in the keV energies, but a unique lower-energy component evolving with time through the burst.

The limitation of the analysis in [GI99] was the short energy range of BATSE. In the tail, the spectra around 100keV have significant contribution from both components

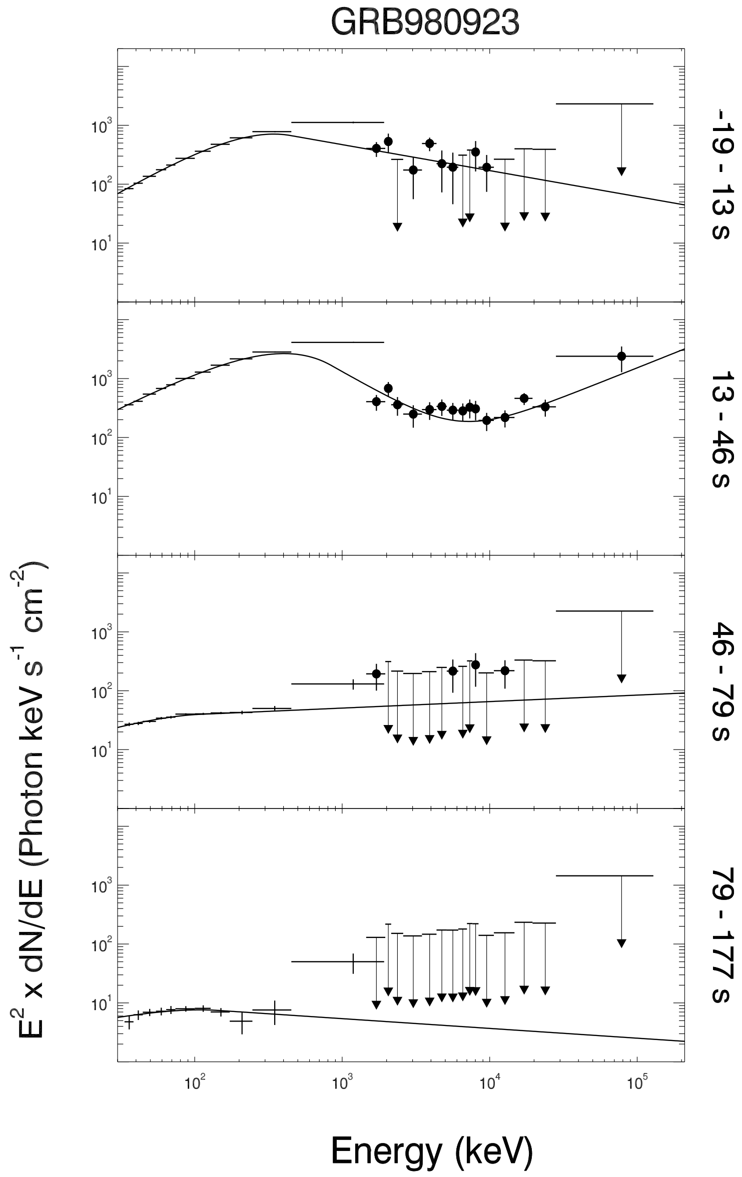

Figure 4.7: Same as 4.6 but energy fluxes for later time intervals are included. The two upper windows correspond to the parameters given in 4.2. Three TASC spectra (79-177s) were combined to increase statistics. TASC spectra for the time intervals 46-79s and 79-177s were fitted with the same assumptions made by [GI99]. The best fits are shown in the two lower windows.

and around 1MeV BATSE sensitivity is too low to undoubtedly resolve the higher-energy component. The limitation of the tail's analysis in this section is, clearly, TASC sensitivity that for GRB980923 was lower than for GRB941017 because of the burst direction.

A higher-energy component has been observed in GRB980923, as in GRB941017. The spectral index describing the higher-energy component is consistent with ~-1. The higher-energy component started within the brightest part of the burst. The duration of the higher-energy component is longer than T90 as suggested by BATSE data in the burst tail. The released energy flux in the energy range of 10-200MeV for a 32s time period was comparable with the ones in GRB941017. BATSE data in the burst tail also suggested that the higher-energy component evolves in time differently than the lower-energy component. Therefore, despite the differences between both bursts, the higher-energy components showed similar features.

4.3 Constrains on the Higher-Energy Spectral Component for E=1-200MeV

Some of the bursts studied in chapter 3 showed more emission at higher energies than the predicted by the Band function. Because of the low significance of the detection above 10MeV, it was not possible to characterize this extra emission in these bursts, except for two of them. The spectra of GRB941017 and GRB980923 required an extra higher-energy component with well-defined spectral index. The goal of this section is to search for the higher-energy component in the other 16 bursts studied in chapter 3.

The analysis is similar to the one described in chapter 3. In this case, the photon model used is a Band function plus a Power Law function of index -1 and pivot energy of 30MeV, like the one observed in GRB941017 and GRB980923. The initial values for the Band parameters are reported in chapter 3. The amplitude of the power law function is a free parameter. One sigma upper and lower limits for the amplitude were determined by fixing all the other parameters and calculating χ^2 as function of the amplitude. The results are shown in Figure 4.8.

If the lower limit of the power law amplitude was below zero, only the one sigma upper limit was plotted as an arrow. When the lower limit was above zero, a solid line was draw with the limits as its edges. Because TASC efficiency depends on the accumulation time, a color code was used for a correct interpretation. Blue and green colors are for spectra with accumulation times of 1,2 and 4s. Black and red colors are for spectra with accumulation times of 16 and 32s. TASC sensitivity is less for shorter accumulation times, and the amplitude is less constrained than for longer accumulation times. A simplistic interpretation of Figure 4.8 may lead to the conclusion that the higher-energy component is "required or observed" in 7 more bursts besides GRB941017 and GRB980923. However, as in previous sections, it is important to calculate the probabilities of improving the fit by chance when adding the power law function. These probabilities are shown in Table 4.3.

Three bursts have probability below $1{\times}10^{-4}$, but only one of them below $1{\times}10^{-5}$. Considering that 2 of the GRB941017 had probability of the order of $1{\times}10^{-4}$. The higher energy will be further considered when the probability of improving the fit by chance by adding a power law function is less than $1{\times}10^{-5}$. This probability, after corrected by the number of analyzed spectra, is better than 3σ detection. Therefore, the higher-energy component is also observed in GRB910503.

BATSE observed GRB910503 at 07:04:13.676 for 50.82s (as determined by T90) from the galactic coordinates $l = 172.03°$ and $b = -5.79°$. The burst direction was 23.6° with respect to the pointing-axis direction of CGRO, placing the burst inside the field of view of COMPTEL and the EGRET spark chamber. The spark chamber data will be analyzed to search for the higher-energy component. GRB910503 had one 10 GeV photon 84s after the BATSE tigger and two well-defined and separated mono peaked episodes. The higher energy component was observed only in the first and brightest episode. The episode had a duration of ∼10s and no a reported tail. The observed higher-energy component is as bright as or brighter than the one in GRB980923.

Therefore, the higher-energy component has been observed in 3/18 bursts. This represents the 16.7% of the bursts. Fifty spectra were analyzed and only 4 of them required the higher-energy component (with a probability of having an improvement in the fit by chance lower than $1{\times}10^{-5}$). This represents the 8%. No cut-off of the higher-energy component has been seeing in any of the three bursts.

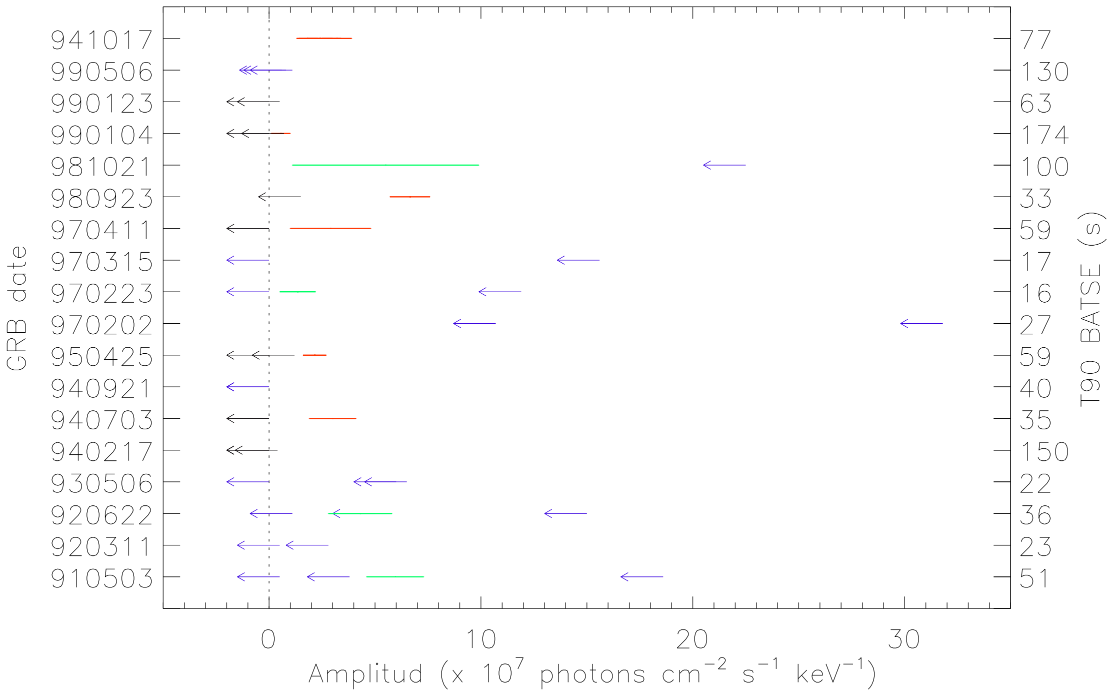

Figure 4.8: Upper limits of the higher-energy component. The calculated limits correspond to 66% confidence level. When the lower limit was zero or below zero, an arrow was plotted with the upper limit as its tail. Otherwise, a line was plotted with the lower and upper limits as its edges. Also, the probabilities of improving the fit by chance when adding the power law function are shown in Table 4.3. The vertical dotted line indicates amplitud equal to zero. Blue and green colors are for spectra with accumulation times of 1,2 and 4s. Black and red colors are for spectra with accumulation times of 16 and 32s.

Burst	**Time period (s)**	$\mathbf{A_{PL}}(\frac{\times 10^{-7}\mathrm{ph}}{\mathrm{s\,cm^{-2}keV}})$	**Probability**
GRB910503	3 - 7	4.6 - 7.3	$\mathbf{3.5 \times 10^{-5}}$
GRB920622	3 - 7	2.8 - 5.8	4.5×10^{-3}
GRB940703	32 - 64	1.9 - 4.1	2.7×10^{-2}
GRB950425	42 - 75	1.6 - 2.7	$\mathbf{1.1 \times 10^{-4}}$
GRB970223	7 - 23	0.5 - 2.2	1.5×10^{-1}
GRB970411	39 - 72	1.0 - 4.8	1.1×10^{-1}
GRB981021	1 - 3	1.1 - 9.9	$\mathbf{2.6 \times 10^{-4}}$

Table 4.3: The 66% confidence level upper and lower limits for the amplitud of a higher-energy component are given in the third column. The corresponding burst and time interval are given in first two columns. The probabilities of improving the fit by chance when adding the power law function are given in last column.

4.4 Constrains on the Higher-Energy Spectral Component for E=1MeV-30GeV

As mentioned in chapter 3, EGRET spark chambers observed only four bursts with a total of 45 photons. However, the analysis in chapter 2, showed that it is possible to obtain limits to the emission at energies of 1MeV-30GeV for bursts in the EGRET field of view. In chapter 2, spectral indexes only below -2.0 were considered because only emission from continuation of the keV-emission to GeV energies was expected. The discussion in the previous sections was to prove the existence of a spectral component at MeV energies. The cut-off of this component was not observed. Therefore, in this section EGRET spark chambers data are used to set limits to the spectral component observed at MeV energies.

The analysis is exactly the same as described in chapter 2. The only difference is the spectral index considered to calculate the limits and that they are 3σupper limits.

The calculation is performed for 33s sequential time intervals as in solar TASC spectra. The results are shown in Figure 4.9.

The results are not much different to the ones presented in chapter 2. But it is important to note the following. Most of the upper limits are above $2{\times}10^{-5}$erg/cm^2 . The best chances for detection were for the brightest bursts in BATSE energy range. And, GRB910503 is included in the set of studied bursts. The BATSE total energy fluence reported was $2.92{\times}10^{-4}$ erg/cm^2 thus the arrow in the left side in the panel for the first 33s corresponds to GRB910503. The energy fluence in the energy interval of 30MeV-10GeV was calculating assuming that the higher-energy component has a cut-off beyond 10GeV and that last 4s. The calculated value is a energy flux of $5.1 \pm 0.56 \times 10^{-6} erg - s^{-1} - cm^{-2}$ or energy fluence $2.04 \pm 0.22 \times 10^{-5}\mathrm{erg} - \mathrm{s}^{-1} - \mathrm{cm}^{-2}$. Since the higher-spectral component may last more than 4s, this numbers are really conservative and the released energy may be higher than $2.04 \pm 0.22 \times 10^{-5}\mathrm{erg} - \mathrm{s}^{-1} - \mathrm{cm}^{-2}$. As observed, it is coincident with the calculated lower limit. Therefore, a higher-energy spectral component extending up to 10GeV energies is perfectly consistent with EGRET spark chambers. Even more, EGRET spark chamber data for GRB910503 may be the first observation of the higher-energy component at GeV energies.

The theoretical implications of the higher-energy component are discussed in the following section.

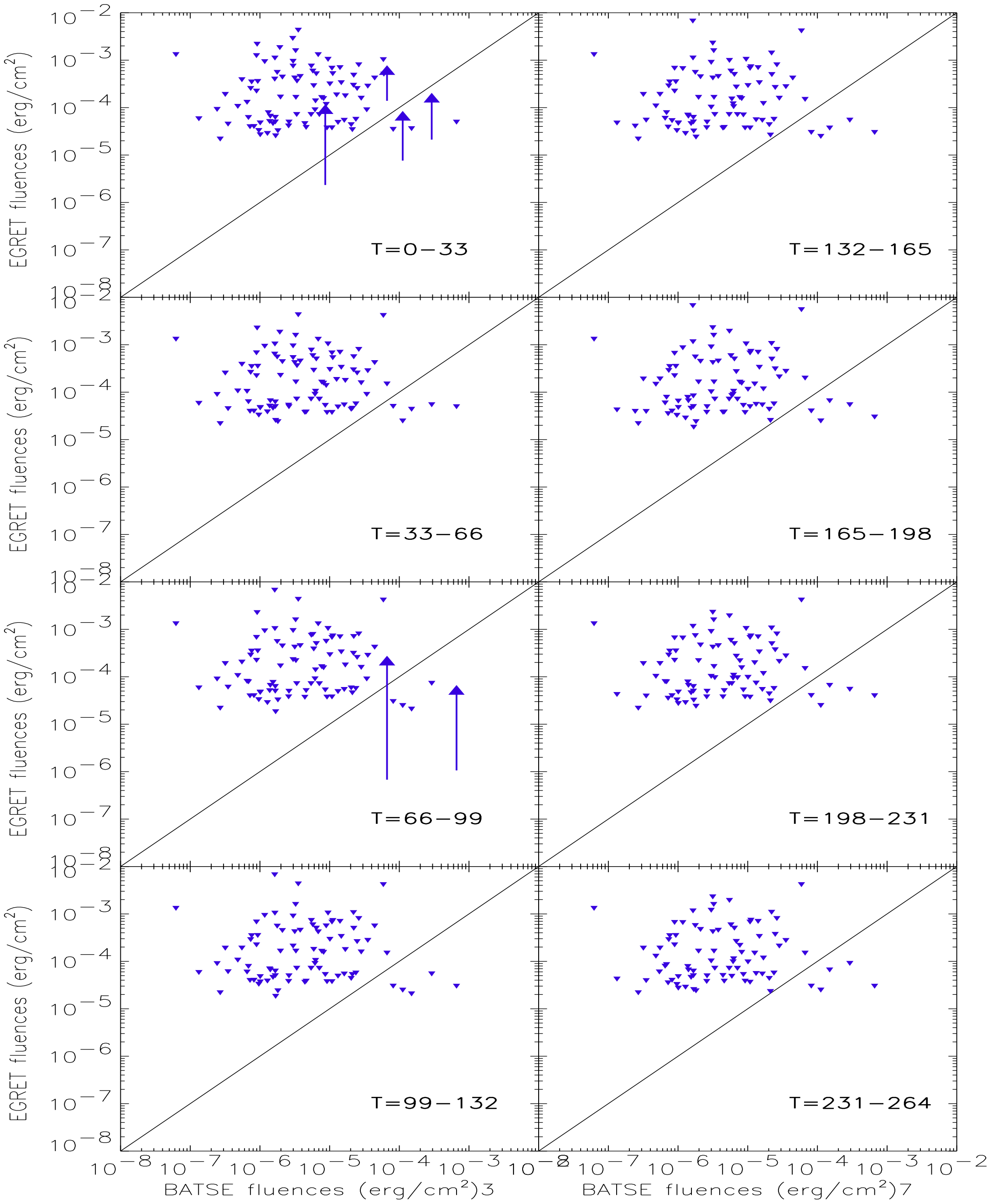

Figure 4.9: Limits to EGRET energy fluences for bursts given in Table 2.1. They are calculated in the energy range of 30MeV-30GeV, for 90% confidence level, spectral index equal to -1.0 and sequential time intervals of 33s starting at the BATSE trigger. They are plotted as function of the BATSE fluence for each burst. When the lower limit was equal to zero, only a triangle has plotted for the upper limit. The arrow heads and tails correspond to the upper and lower limits of EGRET fluences, respectively. The dashed line corresponds to equal fluences in BATSE and EGRET energy sensitivity.

4.5 Theoretical Interpretation

GRB 941017 is the best observation of high energy emission from a burst up to today since its energy distribution and temporal evolution were determined and compared with the well-known sub-MeV emission. Three main conclusions arise from the results given in this chapter, independent of their theoretical interpretation. First, the observed emission exceeds the expected emission from a smooth continuation of the sub-MeV component and has been observed by two independent detectors in at least 3 burst. Second, a new radiation process should be involved to explain the excess since the spectra became harder than the sub-MeV spectra. And third, the higher-energy component is likely to be emitted a different physical region than the sub-MeV component to explain the different temporal evolutions. Therefore, new constrains in the Fireball Model can be derived and/or new radiation processes will be added to the Fireball Model.

Building a theoretical model to explain the emission of the higher-energy component is beyond the scope of this thesis. However, some obvious arguments to reject existing models of high-energy emission are given below.

GRBs are expected to exhibit a synchrotron self-Compton (SSC) component during the prompt phase that extends to photon energies $> \gamma_{\rm pk}^2 {\rm E}_{\rm peak}$, where $\gamma_{\rm pk}$ is the electron Lorentz factor producing synchrotron emission at ${\rm E}_{\rm peak}$. Because $\gamma_{\rm pk} \gg 10^3$ in the external shock of the relativistic blast wave [ME02], this places the peak of the self-Compton component at GeV-TeV energies, even taking into account Klein-Nishina effects on Compton scattering [DE00, ZH01]. To produce self-Compton fluxes with comparable brightness as the synchrotron flux near E_{peak} would require orders-of-magnitude greater luminosities in the self-Compton component, making such an interpretation for the higher-energy emission untenable. This is because of the large amplitude of the additional power law that was observed. A related possibility is that the higher-energy component is due to Compton radiation from synchrotron-emitting electrons that scatter photons from the internal shocks (rather than external shocks) thought to produce the prompt radiation [ZH02], or from an intense radiation field that originates from outside the relativistic blast wave shell [IN03]. The evolution of the Compton fluxes should, however, follow the behaviour of the synchrotron emission, contrary to observations that the higher-energy component evolves with time independently to the synchrotron component. This behaviour could also pose difficulties for other electron models involving Comptonization of photospheric and reverse shock radiation (see [ZH02] for a summary).

Another explanation for the observations is that ultra-relativistic hadrons produce the multi-MeV γ rays by inducing electromagnetic cascades through photomeson and photo-pair production. Acceleration of high-energy protons by GRBs is proposed in models that link GRBs with the sources of the highest energy cosmic rays [VI95, WA95], and would be confirmed through detection of high-energy neutrinos [AL00]. Hadronic cascade radiation spectra are hard and will decay more slowly than the lepton radiations [ZH01, BO98], with potentially brighter fluxes in the hadronic component if more energy is found in the hadrons than the electrons and the hadronic radiation efficiency is high.

After the publication of the observation of the higher-energy component in GRB941017, several authors have theoretically modeled this observation. Table 4.4 summarizes the model basis and predictions. Table 4.5 summarizes the results in reproducing the higher-energy component features. Few of these models require changes in the Standard Fireball Model, see [GR03, ST04]. Most of them give interesting predictions that challenge future experimental work. But more interesting is the difficulty reproducing all the features of the higher-energy component and the high values for the energy where the higher-energy component is expected to peak implying a much more energy in this component than observed in the sub-MeV component. It is important to point out that most of the authors assumed two characteristics in the higher-energy component that have not been concluded from this analysis. One, the higher-energy component is delayed with respect to the sub-MeV component. Clearly, the higher-energy component was not observed from the beginning in any of the three bursts, but one possible explanation is the limited TASC sensitivity and the brightness of the sub-MeV component masking the higher energy flux. In section 4.3, the upper limits for the amplitude of the higher-energy component are very close to the amplitudes of the observed higher-energy component, indicating that those bursts might contain the higher-energy component because it was slightly above TASC sensitivity. The second assumption most of the models make is that, GRB941017 is a rare burst. This conclusion came from the fact that GRB941017 was the strongest noticeable case and the only one published. However after the deeper analysis described in this chapter, two more bursts have been shown to require the higher-energy component for a complete spectral description. Even more, if the energy flux of the higher-energy component follows a distribution similar to that observed for the BATSE energy fluences, only the tail of the energy flux distribution is being observed as consequence of the low TASC sensitivity and much more bursts may present the higher-energy component. Therefore, the small differences observed in the amplitudes of the higher-energy components in all three bursts is a consequence of the limited TASC sensitivity.

Detailed theoretical modeling of this observation is required to quantify and constrain the production mechanisms. This observation did not extend to high enough gamma-ray energies to know the total luminosity in the higher-energy component or the gamma-ray energy at which the flux peaks. Also, because of low TASC sensitivity, questions on the starting time and rareness of the higher-energy component remain open. However, future observations by GLAST [webGLAST], a gamma-ray observatory scheduled to be launched in 2006, with its Gamma Ray Burst Monitor (10 keV - 25 MeV) and its Large Area Telescope (20 MeV - 300 GeV) will be more sensitive and extend to higher energies to better characterize this higher-energy component.

The impact of this higher-energy component is not restricted to electromagnetic radiation mechanisms in GRBs. This higher-energy component may be the counterpart to a future neutrino observation from GRBs [AL04]. It may be a strong contribution to the total energy released in GRBs [FR04]. It may be the connection of GRBs with the sources of Ultra High Energy Cosmic Rays [WI04, WA04]. It may favor GRBs as the producers of chondrules [MC05]. It may constrain the quantum gravity effect [MI03].

Table 4.4: Basis and Predictions of Possible Interpretations to the higher-energy component. First column gives the reference where the interpretation to the higher-energy component is described. The radiative process and the particles involved are given in the second and third columns. In the model implies changes in the Standard Fireball Model or observational predictions or consequences, they are mentioned in the last two columns.

reference	Radiative Process	particles involved	Changes in Std. Fireball Model	Predictions
[GR03]	SSC SSC SSC	$\gamma_{\mathrm{reverse}} + e_{\mathrm{forward}}$ $\gamma_{\mathrm{forward}} + e_{\mathrm{reverse}}$ $\gamma_{\mathrm{reverse}} + e_{\mathrm{reverse}}$	- - To get $\gamma = -1$ prompt must be SSC	- - optical flash
[PE04]	SSC + self abs.	$\gamma_{\mathrm{reverse}} + e_{\mathrm{forward}}$	N	Lower limits for Total burst energy and Lorentz factor of expansion, Upper limits for surrounding density and energy in magnetic field.
[ST04]	2nd order SSC	e plasma inestabilities behind the shock front or refreshed internal shocks.	Y, prompt due to 1st order SSC and continuosly heated e.	prompt and delay GeV emission
[BE05]	SSC	$\gamma_{\mathrm{internal,prompt}} + e_{\mathrm{forward}}$	N	No in short bursts Upper limits in surroundings density long bursts with low Γ
[DE04] & [DE04b]	Synch. Synch.	$e^{\pm}$ from $\pi^{\pm}$ produced in $p + \gamma_{internal,synchrotron}$ or $p + \gamma_{externalfield}$ $e^{\pm}$ from $n + \gamma_{externalfield}$ produced in $p + \gamma$	N N	responsable of emission between 1-10 MeV

Table 4.5: Results of Possible Interpretations compared with the observed features of the higher-energy component. First column gives the reference where the interpretation to the higher-energy component is described. 'Y' and 'N' indicate that the model result is or is not consistent with the observation, respectively.

reference	spec index of high E comp	constant γ?	Temporal evolution	delayed & long?	peaking energy	rare?
[GR03]	-	-	-	-	10-100 GeV	-
	-	-	-	-	10-100 GeV	-
	-1/2	N	-	Y	few hund. of MeV	rare
[PE04]	Y	Y	Y	Y	1 GeV	rare
[ST04]	Y	Y	slow	Y	0.01-10GeV	typical
[BE05]	$\gamma = \alpha$	N	diff. to prompt	Y	GeV-TeV	rare, low Γ
[DE04] & [DE04b]	-1.5 to -2	N	same as prompt	N, start	-	rare
	Y	Y	Y	Y		rare

Conclusions

The goal of this thesis is to extend our knowledge of the GRB emission for energies in the range of MeV-GeV. Data from three detectors of CGRO were used in the analysis because they covered the broadest energy range existing up to now. The goal was achieved and very important results were obtained. These results are summarized below.

- A systematic search for delayed emission was proposed and done for energies in the range of 30MeV-30GeV.

- Prompt or delayed emission at energies of 30MeV-30GeV was not observed from a burst different to that previously reported in the bibliography.

- Upper limits to the energy fluences of prompt and delayed emission at energies of 30MeV-30GeV were calculated for all possible bursts in the EGRET's spark chambers field of view.

- Time-resolved spectra for 18 bursts were obtained for energies in the range of 20keV-200MeV.

- The time-resolved spectra for 16 bursts have been carefully characterized.

- Time-resolved spectra for 14/16 bursts were described by a Band function and the temporal evolution of their spectra was determined.

- 2/3 of these bursts showed spectra with a hard-to-soft temporal evolution in single peaks.

- No high energy cutoff was observed in any burst's spectra.

- An extra spectral component was found in three bursts, GRB941017, GRB980923 and GRB910503.

- This extra spectral component is described by a power law of differential photon number index of -1. It evolves slower in time than the sub-MeV emission. The energy flux, at least for two bursts, was fairly constant in time and between bursts within the uncertainties. The peak energy of this component was not observed, at least up to the energies of 200MeV.

- Theoretical interpretations to this extra spectral component within the favored Fireball model is not possible without extreme conditions either in the radiative process or the fireball surroundings.

- A link between this extra spectral component and the sources of the highest-energy cosmic rays is the result of a possible theoretical interpretation of the extra spectral component.

The time-resolved analysis that was done on a broader energy range was focused on bursts with bright energy fluences and bright photon fluxes. A search for the extra spectral component in other BATSE bursts could be done. However, a preliminary analysis [CA05] has been done for bursts with high energy fluences and low photon fluxes and, the results are not promising. Only one burst of twenty five had significant detection in TASC spectra with no evidence of a extra spectral component. This is a consequence of the TASC sensitivity. Thus, better quality data is required. In this sense GLAST with a lower sensitivity and broader energy range than EGRET spark chambers and TASC should see more of these bursts with this extra spectral component. GLAST will be capable of observed the peak energy, the energy fluence distribution and the frequency of this extra spectral component, which are crucial information to constrain the source modeling.

Bibliography

[AL00] Alvarez-Muiz J., Halzen F. & Hooper D. W., *Phys.Rev.D.*, **62**, 093015 (2000).

[AL04] Alvarez-Muiz J., Halzen F. & Hooper D. W., *ApJ*, **604**, L85 (2004).

[AT00] Atkins R., Benbow W., Berley D., Chen M.L., Coyne D.G., Dingus B.L., Dorfan D.E., Ellsworth R.W., Evans D., Falcone A., Fleysher L., Fleysher R., Gisler G., Goodman J.A., Haines T.J., Hoffman C.M., Hugenberger S., Kelley L.A., Leonor I., McConnell M., McCullough J.F., McEnery J.E., Miller R.S., Mincer A.I., Morales M.F., Nemethy P., Ryan J.M., Shen B., Shoup A., Sinnis C., Smith A.J., Sullivan G.W., Tumer T., Wang K., Wascko M.O., Westerhoff S., Williams D.A., Yang T. & Yodh G.B., *ApJ*, **533**, L119 (2000).

[AT04] Atkins R., Benbow W., Berley D., Blaufuss E., Bussons J., Coyne D.G., DeYoung T., Dingus B.L., Dorfan D.E., Ellsworth R.W., Fleysher L., Fleysher R., Gisler G., Gonzalez M.M., Goodman J.A., Haines T.J., Hays E., Hoffman C.M., Kelley L.A., McEnery J.E., Miller R.S., Mincer A.I., Morales M.F., Nemethy P., Noyes D., Ryan J.M., Samuelson F.W., Shoup A., Sinnis G., Smith A.J., Sullivan G.W., Williams D.A., Westerhoff S., Wilson M.E., Xu X. & Yodh G.B., *ApJ*, **604**, L25 (2004).

[AT85] Atteia J.L., Barat C., Hurley K., Niel M., Vedrenne G., Evans W.D., Fenimore

E.E., Klebesadel R.W., Laros J.G. & Cline T. L., *In 19th Intern. Cosmic. Ray Conf.*, **1**, 33 (1985).

[AT91] Atteia J.L., Barat C., Jourdain E., Niel M., Vedrenne G., Blinov N., Chernenko A., Dolidze V., Kozlenkov A., Kuznetsov A., Mitrofanov I., Pozanenko A., Sunyaev R. & Terekhov O., *Nature*, **351**, 296 (1991).

[BA93] Band D., Matteson J., Ford L., Schaefer B., Palmer D., Teegarden B., Cline T., Briggs M., Paciesas W., Pendleton G., Fishman G., Kouveliotou C., Meegan C., Wilson R. & Lestrade P., *ApJ*, **413**, 281 (1993).

[BA99] Barthelmy S.D., Butterwoth P., Cline T.L. & Gehrels N., *AAS bulletin*, **31**, 718 (1999).

[BE05] Beloborodov A.M., *ApJ*, **618**, L13 (2005).

[BL03] Bloom J.S., Berger E., Kulkarni S.R., Djorgovsky S.G. & Frail D.A., *AJ*, **125**, 999 (2003).

[BL99] Blandford R.D. & Helfand D.J., *MNRAS*, **305**, L45 (1999).

[BL99a] Bloom J.S., Odewanh S.C., Kulkarni S.R., Djorgovsky S.G., Harrison F.A., Koresko C., Neugebauer G., Armus L., Frail D.A., Gal R.R., Sari R., Squires G., Illingworth G., Kelson D., Chaffee F.H., Goodrich R., Feroci M., Costa E., Piro L., Frontera F., Mao S., Akerlof C. & McKay T.A., *ApJ*, **518**, L1 (1999).

[BJ01] Bjornsson G., Holland S., Hjorth J. & Thomsen B., *grba.conference*, 175 (2001).

[BJ01a] Bjornsson C.I., *ApJ*, **554**, 593 (2001).

[BO98] Boettcher M. & Dermer C., *ApJ*, **499**, L131 (1998).

[BR98] Briggs M.S., Band D.L., Preece R.D., Pendleton G.N., Paciesas W.S. & Matteson J.L., *Gamma-Ray Bursts. AIP conference proceedings*, ed. Meegan C.A., Preece R.D. & Koshut T.M., **428**, 299 (1998).

[BR99] Briggs M.S., Preece R.D., Band D.L. & Kouveliotou C., *AAA*, **31**, 711 (1999).

[BR99a] Briggs M.S., Band D.L., Kippen R.M., Preece R.D., Kouleveliotou C., van Paradus J., Share G.H, Murphy R.J, Matz S.M., Connors A., Winkler C., McConnell M.L., Ryan J.M., Williams O.R., Young C.A., Dingus B., Catelli J.R. & Wijers R.A.M., *ApJ*, **524**, 82 (1999).

[BU03] Burbidge G.R., *ApJ*, **585**, 112 (2003).

[CA05] Carrillo M., *B.Sc. thesis,* under preparation. Universidad Autonoma de México.

[CA03] Coburn W. & Boggs S.E., *Nature*, **423**, 415 (2003).

[CA98] Catelli J.R., Dingus B.L. & Schneid E.J., *AIPC*, **428**, 309 (1998).

[CA99] Castro-Tirado, A.J., Zapatero-Osorio M.R., Caon N., Cairos L.M., Hjorth J., Pedersen H., Andersen M.I., Gorosabel J., Bartolini C., Guarnieri A., Piccioni A., Frontera F., Masetti N., Palazzi E., Pian E., Greiner J., Hudec R., Sagar R., Pandey A.K., Mohan V., Yadav R., Nilakshi, Bjornsson G., Jakobsson P., Burud

I., Courbin F., Valentini G., Piersimoni A., Aceituno J., Montoya L.M., Pedraz S., Walter F., Ott J., Hippelein H., Sanchez-Bejar V., Gutierrez C., Oscoz A., Zhu J., Chen J., Zhang H., Wei J., Zhou A., Guziy S., Shlyapnikov A., Heise J., Costa E., Feroci M. & Piro L., *Sci*, **5410**, 2069 (1999).

[CH99] Chiang J. & Dermer C., *ApJ*, **512**, 699 (1999).

[DA99] Dai Z.G. & Lu T., *ApJ*, **519**, L155 (1999).

[DE00] Dermer C.D., Chiang J. & Mitman K.E., *ApJ*, **537**, 785 (2000).

[DE04] Dermer C.D. & Atoyan A., *Gamma-Ray Bursts. AIP Conference Proceedings*, ed. Fenimore E.E. & Galassi M., **727**, 557 (2004).

[DE04b] Dermer C.D. & Atoyan A., *A&A*, **418**, L5 (2004).

[DI01] Dingus B.L., *In High-Energy Gamma Ray Astronomy. AIP Conference Proceedings*, ed. Aharonian F.A. & Heinz J.V, **558**, 383 (2001).

[DI01b] Dingus B.L., *Gamma-Ray Bursts and afterglow astronomy 2001. AIP Conference Proceedings*, ed. Ricker G.R. & Vanderspek R.K., **662**, 294 (2001).

[DI95] Dingus B., *Ast.Sp.Sc.*, **231**, 187 (1995).

[DI98] Dingus B., Catelli J.R. & Schneid E.J., *AIPC*, **428**, 349 (1998).

[FA02] Fan Y.Z., Dai Z.G., Huang Y.F. & Lu T., *Chin.J.Astron.Astrophys.* **2** 449 (2002).

[FE98] Feldman G.J. & Cousins R.D. , *Ph.Rv.D*, **57, Iss. 7** 3873 (1998).

[FE99] Fenimore E.E., Ramirez-Ruiz E. & Wu Bobing, *ApJ*, **518**, L73 (1999).

[FI89] Fishman G.J., Meegan C.A., Wilson R.B., Paciesas W.S., Parnell T.A., Matteson J.L., Teegarden B.J., Cline T.L., Pendleton G.N. & Schaefer B.E., *In: GRO Science Workshop*, 3 (1989).

[FI95] Fishman G.J. & Meegan C.A., *ARA&A*, **33**, 415 (1995).

[FO95] Ford L.A., Band D.L., Matteson J.L., Briggs M.S., Pendleton G.N., Preece R.D., Paciesas W.S., Teegarden B.J., Palmer D.M., Schaefer B.E., Cline T.L., Fishman G.J., Kouveliotou C., Meegan C.A., Wilson R.B. & Lestrade J.P., *ApJ*, **439-1**, 307 (1995).

[FR04] Frail D.A., *Nuc.Phys.B, Proc.Suppl.*, **132**, 255 (2004).

[FR99] Fruchter A.S., Thorsett S.E., Metzger M.R., Sahu K.C., Petro L., Livio M., Ferguson H., Pian E., Hogg D.W., Galama T., Gull T., Kouveliotou C., Macchetto D., van Paradijis J., Pedersen H. & Smette A., *ApJ*, **519**, L13 (1999).

[GA99] Gallant Y.A., Achterberg A., Kirk J.G., *A& A*, **138**, 549 (1999).

[GI00] Giblin T.W., *PhD. Thesis*, University of Alabama in Huntsville (2000).

[GI99] Giblin T.W., van Paradijs J., Kouveliotou C., Connaughton V., Wijers R.A.M., Briggs M.S., Preece R.D. & Fishman G.J., *ApJ*, **524**, L47 (1999).

[GO03] González M.M., Kaneko Y., Preece R. & Dingus B.L., *GAMMA-RAY BURST AND AFTERGLOW ASTRONOMY 2001. AIP Conference Proceedings*, **662**, 267 (2003).

[GO03b] González M.M., Dingus B.L., Kaneko Y., Preece R.D., Dermer C.D. & Briggs M.S., *Nature*, **424**, 749 (2003).

[GO04] González M.M., Dingus B.L., Kaneko Y., Preece R.D. & Briggs M.S., *Gamma-Ray Bursts. AIP Conference Proceedings*, ed. Fenimore E.E. & Galassi M., **727**, 236 (2004).

[GO04b] González M.M., Dingus B.L., Kaneko Y., Preece R.D. Dermer C.D. & Briggs M.S., *Gamma-Ray Bursts. AIP Conference Proceedings*, ed. Fenimore E.E. & Galassi M., **727**, 203 (2004).

[GR03] Granot J. & Guetta D., *ApJ*, **598**, L11 (2003).

[GR95] Greiner J., Sommer M., Bade N., Fishman G.J., Hanlon L.O., Hurley K., Kippen R.M., Kouveliotou C., Preece R., Ryan J., Shconfelder V., William O.R., Winkler C., Boer M. & Niel M., *A&A*, **302**, 121 (1995).

[HA92] Hartman R.C., Bertsch D.L., Fichtel C.E., Hunter S.D., Kanbach G., Kniffen D.A., Kwok P.W., Lin Y.C., Mattox J.R.& Mayer-Hasselwander H.A., *In its The Compton Observatory Science Workshop*, 116 (1992).

[HA94] Hanlon L.O., Bennett K., Collmar W., Connors A., Diehl R., van Dijk R., Greiner J., den Herder J.W., Hermsen W., Kippen R.M., Kuiper L., McConnell M., Ryan J., Schonfelder V., Steinle H., Strong A., Verendorff M., William O.R. & Winkler C., *A&A*, **285**, 161 (1994).

[HA98] Harris M.J. & Share G.H., *ApJ*,**494**, 724 (1998).

[HI90] Higdon J.C. & Schmidt M., *ApJ*, **355**, 13 (1990).

[HJ03] Hjorth J., Sollerman J., Mller P., Fynbo J.P.U., Woosley S.E., Kouveliotou C., Tanvir N.R., Greiner J., Andersen M.I., Castro-Tirado A.J., Castro C.J.M., Fruchter A.S., Gorosabel J., Jakobsson P., Kaper L., Klose S., Masetti N., Pedersen H., Pedersen K., Pian E., Palazzi E., Rhoads J.E., Rol E., van den Heuvel E.P.J., Vreeswijk P.M., Watson D. & Wijers R.A.M.J., *Nature*, **423**, 847 (2003).

[HO00] Holland S., Bjornsson G., Hjorth J. & Thomsen B., *A&A*, **364**, 467 (2000).

[HO99] Holland S. & Hjorth J., *A&A*, **344** L67, (1999).

[HU94] Hurley K, Dingus B.L., Mukherjee R., Sreekumar P., Kouveliotuo C., Meegan C., Fishman G.J., Band D., Ford L., Bertsch D., Cline T., Fichtel C., Hartaman R., Hunter S., Thompson D.J., Kanbach G., Mayer-Hasselwander H., von Montigny C., Sommer M., Lin Y., Nolan P., Michelson P., Kniffen D., Mattox J., Schneid E., Boer M. & Niel M., *Nat*, **372**, 652 (1994).

[IN03] Inoue S., Guetta D. & Pacini F., *ApJ*, **583**, 379 (2003).

[KA04] Kaneko Y., Hanlon L., Preece R.D., Gonzalez M.M., Dingus B.L., Briggs M.S., Williams O.R., Bennett K. & Winkler C., *Gamma-Ray Bursts. AIP Conference Proceedings*, ed. Fenimore E.E. & Galassi M., **727**, 244 (2004).

[KA05] Kaneko Y. *Ph.D. thesis*, in preparation.

[KA77] Kane S.R. & Share G.H., *ApJ*, **217**, 549 (1977).

[KA88] Kanbach G., Bertsch D.L., Fichtel C.E., Hartman R.C., Hunter S.D., Kniffen D.A., Hughlock B.W., Favale A., Hofstadter R. & Hughes E.B., *Space Science Reviews*, **49**, 69 (1988).

[KI96] Kippen R.M., Ryan J., Connors A., McConnell M., Winkler C., Hanlon L.O., Schnfelder V., Greiner J., Varendorff M., Collmar W., Hermsen W. & Kuiper L., *In: Gamma-ray bursts* , **384**, 197 (1996).

[KL73] Klebesadel R.W., Strong I.B. & Olson R.A., *ApJ*, **182**, L85 (1993).

[KO93] Kouveliotou C., Meegan C.A., Fishman G.J., Bhat N.P., Briggs M.S., Koshut T.M., Paciesas W.S. & Pendleton G.N., *ApJ*, **413**, L101 (1993).

[KU88] Kudryavtsev M.I. & Svertilov S.I., *Soviet Astr.Lett.*, **14**, 90 (1988).

[KU99] Kulkarni S.R., Frail D.A., Sari R., Moriarty-Schieven G.H., Shepherd D.S., Udomprasert P., Readhead A.C.S. & Bloom J.S., *ApJ*, **522**, L97 (1999).

[KW93] Kwok P.W., Bertsch D.L., Dingus B.L., Fichtel C.E., Hartman R.C., Hunter S.D., Mattox J.R., Sreekumar P., Thompson D.J., Schneid E.J., Kanbach G., Mayer-Hasselwander H.A., von Montigny C., Pinkau K., Rothermel H., Sommer M., Lin Y.C., Michelson P.F., Nolan P.L. & Kniffen D.A., *AIP*, **280**, 855 (1993).

[KW94] Kwok P.W., et. al., *AIP*, **280**, 855 (1994).

[LL00] Lloyd N.M. and Petrosian V., *ApJ*, **543**, 722(2000).

[LI99] Liang E.P., Crider A., Bottcher M. & Smith I.A., *ApJ*, **519**, L21 (1999).

[MA82] Mazets E.P., Golenetskii S.V., Ilinskii V.N., Gurian Iu.A., Aptekar R.L., Panov V.N., Sokolov I.A., Sokolova Z.Ia. & Kharitonova, T.V, *ApSS*, **82**, 261 (1982).

[MC05] McBreen B., Winston E., McBreen S. & Hanlon L., *A&A*, **429**, L41 (2005).

[ME02] Mészáros P., *Ann.Rev.Astron.Astrophys*, *40*, 137 (2002).

[ME03] Mészáros P., *astroph/0311321* , (2003).

[ME03a] Mészáros P., *Nature*, **423**, 809 (2003).

[ME92] Meegan C.A., Fishman G.J., Wilson R.B., Horack J.M., Brock M.N., Paciesas W.S., Pendleton G.N. & Kouveliotou C., *Nature*, **355**, 143 (1992).

[ME99] Mzros P. & Rees M.J., *MNRAS*, **306**, L39 (1999).

[MI00] Mitra A., *A&A*, **359**, 413 (2000).

[MI03] Mitrofanov I.G., *Nature*, **426**, 139 (2003).

[NE85] Nelson W.R., Hirayama H. & Rogers D.W.O., *SLAC Rep.*, 265 (1985).

[NO92] Nolan P.L., Bertsch D.L., Fichtel C.E., Hartman R.C., Hofstadter R., Hughes E.B., Hunter S.D., Kanbach G., Kniffen D.A., Lin Y.C., Mattox J.R., Mayer-Hasselwander H.A., Michelson P.F., von Montigny C., Pinkau K., Rothermel H., Schneid E., Sommer M., Sreekumar P. & Thompson, D.J., *IEEE Transactions Nucl. Sci.*, **39**, 993 (1992).

[PA97] Park H.S., Williams G.G., Ables E., Band D.L., Barthelmy S.D., Bionta R., Butterworth P.S., Cline T.L., Ferguson D.H., Fishman G.J., Gehrels N., Hartman D., Hurley K., Kouveliotou C., Meegan C.A., Ott L., Parker E. & Wurtz R., *ApJ*, **490**, L21 (1997).

[PE04] Pe'er A. & Waxman E., *ApJ*, **603**, L1 (2004).

[PE95] Pendleton G.N., Paciesas William S., Mallozzi R.S., Koshut T.M., Fishman G.J., Meegan C.A., Wilson R.B., Horack J.M., Lestrade J.P., *NIMSA*, **364**, 567 (1995).

[PR00] Preece R.D., Briggs M.S., Mallozzi R.S., Pendleton G.N., Paciesas W.S. & Band D.L., *ApJ*,**126**, 19 (2000).

[PR02] Press W.H., Teukolsky S.A., Vetterling W.T. & Flannery B.P., *Numerical Recipes in C: The art of scientific computing* , Cambridge University (1992).

[PR94] Preece R.D., Brock M.N. & Briggs M.S., *WINGSPAN, Windows Gamma Spectral Analysis*, Internal BATSE Documentation, (1994).

[PR96] Preece R.D., Briggs M.S., Pendleton G.N., Paciesas W.S., Matteson J.L., Band D.L., Skelton R.T. & Meegan C.A., *ApJ*,**473**, 310 (1996).

[PR98] Preece R.D., Pendleton G.N., Briggs M.S., Mallozzi R.S., Paciesas W.S., Band D.L., Matteson J.L. & Meegan C.A., *ApJ*,**496**, 849 (1998).

[PR98a] Preece R.D., Briggs M.S., Mallozzi R.S., Pendleton G.N., Paciesas W.S., Band D.L., *ApJ*,**506**,L23 (1998).

[RU75] Ruderman M., *Ann.N.Y.Acad.Sci.*, **262**, 164 (1975).

[SA99] Sari R. & Piran T., *ApJ*, **517**, L109 (1999).

[SC78] Schmidt W.K.H., *Nature*, **271**, 525 (1978).

[SC92] Schneid E.J., Bertsch D.L., Fichtel C.E., Hartman R.C., Hunter S.D., Kanbach G., Kniffen D.A., Kwok P.W., Lin Y.C., Mattox J.R., Mayer-Hasselwander H.A., Michelson P.F., von Montigny C., Nolan P.L., Pinkau K., Rothermel H., Sommer M., Sreekumar P. & Thompson D.J., *A&A*, **255**, L13 (1992).

[SC93] Schneid E.J., Bertsch D.L., Dingus B.L., Fichtel C.E., Hartman R.C., Hunter S.D., Kanbach G., Kniffen D.A., Kwok P.W., Lin Y.C., Mattox J.R., Mayer-

Hasselwander H.A., Michelson P.F., von Montigny C., Nolan P.L., Pinkau K., Rothermel H., Sommer M., Sreekumar P. & Thompson D.J., *AIP*, **280**, 850 (1993).

[SC94] Schaefer B.E., Teegarden B., Cline T., Dingus B.L., Fishman G.J., Meegan C.A., Wilson R.B., Paciesas W.S., Pendleton G.N., Band D.L., Schneid E.J., Kwok P.W., Schnfelder V., Winkler C., Hermsen W. & Kippen R.M., *AIP*, **307**, 280 (1994).

[SC95] Schneid E.J., Bertsch D.L., Dingus B.L., Fichtel C.E., Hartman R.C., Hunter S.D., Kanbach G., Kniffen D.A., Lin Y.C., Mattox J.R., Mayer-Hasselwander H.A., Michelson P.F., von Montigny C., Nolan P.L., Sreekumar P. & Thompson D.J., *ApJ*, **453**, 95 (1995).

[SC96] Schaefer B.E., Palmer D., Fichtel C.E., Dingus B.L., Schneid E.J., Kippen R.M., Winkler C., Hanlon L. & and Schonfelder V., *In: Gamma-Ray Bursts*, **384**, 248 (1996).

[SC98] Schaefer B.E., Hobbeheydar J., Bromm V. & Fenimore E.E., *??*, **428**, 379 (1998).

[SH92] Share G.H., Messina D.C., Iadicicco A., Matz S.M., Rieger E. & Forrest D.J., *In: Gamma-ray bursts - Observations, analyses and theories*, 249 (1992).

[SH92b] Share G.H., Johnson W.N., Kinzer R.L., Kroeger R.A., Kurfess J.D., Murphy R.J., Strickman M.S., Matz S.M., Grabelsky D.A. & Purcell W.R., *In: Gamma-ray bursts*, **265**, 32 (1992).

[SH94] Share G.H., Johnson W.N., Kurfess J.D., Murphy R.J., Connors A., Dingus B.L., Schaefer B.E., Band D., Matteson J., Collmar W., Schnfelder V., Fichtel C.E., Kwok P.W., Teegarden B.J., Fishman G., Kuiper L., Jung G.V., Matz S.M., Nolan P.L., Schneid E.J. & Winkler C., *AIP*, **307**, 283 (1994).

[SO00] Sokolov V.V., Fatkhullin T.A. & Komarova V.N., *BSAO*, **49**, 14 (2000).

[SO02] Soderberg A.M. & Ramirez-Ruiz E., *MNRAS*, **330**, L24 (2002).

[SO03] Soderberg A.M. & Ramirez-Ruiz E., *AIPC*, **662**, 172 (2003).

[SO94] Sommer M., Bertsch D.L., Dingus B.L., Fichtel C.E., Fishman G.J., Harding A.K., Hartman R.C., Hunter S.D., Hurley K., Kanbach G., Kniffen D.A., Kouveliotou C., Lin Y.C., Mattox J.R., Mayer-Hasselwander H.A., Michelson P.F., von Montigny C., Nolan P.L., Schneid E., Sreekumar P. & Thompson D.J., *ApJ*, **422**, L63 (1994).

[ST04] Stern B.E. & Poutanen J., *MNRAS*, **352**, L35 (2004).

[ST98] Strohmayer T.E., Fenimore E.E., Murakami T. & Yoshida A., *ApJ*, **500**, 873 (1998).

[TA00] Taylor G.B., Bloom J.S., Frail D.A., Kulkarni S.R., Djorgovsky S.G. & Jacoby B.A., *ApJ*, **537**, L17 (2000).

[TH93] Thompson D.J., Bertsch D.L., Fichtel C.E., Hartman R.C., Hofstadter R., Hughes E.B., Hunter S.D., Hughlock B.W., Kanbach G., Kniffen D.A., Lin Y.C., Mattox J.R., Mayer-Hasselwander H.A., von Montigny C., Nolan P.L., Nel H.I., Pinkau K., Rothermel H., Schneid E.J., Sommer M., Sreekumar P., Tieger D. & Walker A.H., *ApJS*, **86**, 629 (1993).

[TO97] Tokanai F., Yoshida A., Otani C., Kawai N., Shibata R., Murakami T., Ueda Y. & Hurley K., *PASJ*, **49**, 207 (1997).

[VI95] Vietri M., *ApJ*, **453**, 883 (1995).

[WA00] Wang X.Y., Dai Z.G. & Lu T., *MNRAS*, **319**, 1159 (2000).

[WA04] Waxman E., *ApJ*, **606**, 988 (2004).

[WA95] Waxman E., *Phys.Rev.Lett.*, **75**, 386 (1995).

[WI00] Williams G.G., Hartmann D.H., Park H.S., Porrata R.A., Ables E., Bionta R., Band D.L., Barthelmy S.D., Cline T., Gehrels N., Ferguson D.H., Fishman G., Kippen R.M., Kouveliotou C., Hurley K., Nemiroff R. & Sasseen T., *AIPC*, **526**, 250 (2000).

[WI04] Wick S.D., Dermer C.D. & Atoyan A., *Astro.Part.Phys.*, **21**, 125 (2004).

[WI92] Winkler C., Bennett K., Bloemen H., Collmar W., Connors A., Diehl R., Vandordrecht A., den Herder J.W., Hermsen W., Kippen M., Kuiper L., Lichti G., Lockwood J., McConnell M., Morris D., Ryan J., Schonfelder V., Stacy C., Steinle H., Strong A., Swanenburg B., Taylor B.G., Varendorff M. & de Vries C., *A&A*, **255**, L9 (1992).

[WI95] Winkler C., Kippen R.M., Bennett K., Collmar W., Hanlon L.O., Hermsen W., Flaherty K.S.O., Ryan J.M., Schoenfelder V., Sreible H. & Williams O.R., *A& A*, **302**, 765 (1995).

[WR02] Wren D.N., Bertsch D.L. & Ritz S., *ApJ*, **574**, L47 (2002).

[YO99] Young C.A., Connors A., McConnell M., Ryan J.M., Williams O.R., Winkler C., Bennett K., Hermsen W., Kuiper L., Collmar W., Schoenfelder V., Kippen R.M. & CGRO-COMPTEL Team, *AAA*, **31**, 711 (1999).

[YO00] Young C.A., Connors A., Bennett K, Collmar W., Hermsen W., Kippen R.M., Kolaczky E., Kuiper L., McConnell M., Miller R., Ryan J.M., Schonfelder V., Williams O.R. & Winkler C., *AICP*, **526**, 170 (2000).

[ZH01] Zhang B. & Mészáros P., *ApJ*, **559**, 110 (2001).

[ZH02] Zhang B. & Mészáros P., *ApJ*, **581**, 1236 (2002).

[ZH03] Zhang B., Mészáros P., astro-ph/0311321.

[EGRETdoc] http://cossc.gsfc.nasa.gov/egret/egret_doc.html

[webBATSEid3245] http://cossc.gsfc.nasa.gov/batse/BATSE_Ctlg/html/3245.html

[webBATSEid7114]
ftp://legacy.gsfc.nasa.gov/compton/data/batse/trigger/07001_07200/07113_burst/

[webComptel] http://wwwgro.unh.edu/bursts/cgrbdata.html, 08/13/1997.

[webGLAST] http://glast.gsfc.nasa.gov/